

# FINAL REPORT

## Mechanism-Based Modeling of Hydrogen Environment Assisted Cracking (HEAC) in High Strength Alloys for Marine Applications:

### *Prediction of Monel K-500 HEAC for Select Environmental and Mechanical Conditions*

Contract Number N00014-10-1-0552

Office of Naval Research  
Ballston Center Tower One  
800 North Quincy Street  
Arlington, VA 22217-5660

Attention:  
Dr. Airan Perez  
Program Officer  
Office of Naval Research  
airan.perez@navy.mil

John R. Scully\* and Richard P. Gangloff\*, and Dr. Francisco Presuel Moreno#  
\*Charles Henderson Chaired Professor of Materials Science and Engineering/Co-director Center for Electrochemical Science and Engineering

\*Ferman W. Perry Professor  
Department of Materials Science and Engineering  
School of Engineering and Applied Science  
University of Virginia  
Charlottesville, VA 22904

# Florida Atlantic University,  
Dept of Ocean and Mechanical Engineering,  
101 North Beach Road, Dania Beach, FL 33004.

[Jrs8d@virginia.edu](mailto:Jrs8d@virginia.edu)  
434.982.5786  
434.982.5799

A final report  
October 15, 2012

Period of Performance: 2/15/10 to 8/15/2012

20121113170

## STATEMENT OF WORK

### OBJECTIVE

The objective of this interdisciplinary research program was to implement quantitative-predictive models of hydrogen environment assisted cracking (HEAC) of Monel K-500 in a pseudo-application specific situation. Here the crack growth behavior and component lifetime will be predicted as a function of applied stress, surface condition component geometry (summed into stress intensity variation), as well as metallurgical and environmental conditions (applied cathodic potential in seawater with local pH and potential at a crack tip). These conditions were relevant to naval components in the marine environment. Research emphasized hydrogen environment assisted cracking. The scientific goal was to improve understanding of crack tip electrochemical, H-trap interaction, and fracture processes at the microscopic scale to enable threshold and crack growth rate predictions in Ni-based alloys which differ substantially from high strength steels studied previously at UVa. The engineering goal is to transform this understanding into quantitative predictions of H uptake, H crack initiation and growth towards component lifetimes. An example of component lifetime for a generic bolt is detailed in Task 2 findings. Such models must be sufficiently flexible and implemented to accept metallurgical, mechanical and electrochemical inputs for Monel K-500 to predict cracking behavior and replace extensive empirical experimentation. The overarching goal was to provide outputs relevant to engineering that are based on proper physics of crack tip hydrogen uptake and chemo-mechanical damage. With active interactions involving US Navy laboratories, this research can impact cathodic protection system optimization (for instance, low voltage anodes) for a single material condition as well as component failure analysis/design.

A follow-up program has been initiated to examine the effect of metallurgical variation (heat-to-heat variations ) specific to Navy program interests. The goal of this follow-on program is to determine how robust the model is towards heat-to-heat variations.

### SCOPE

This work will consider a single condition of Monel K-500 only. Results show that such high strength alloys in the selected classes are susceptible to Internal Hydrogen Assisted Cracking (IHAC) and HEAC, and may be more severely prone to the complicating effect of crack tip strain rate. Two material properties will be modeled; the threshold stress intensity for the onset or arrest of subcritical H crack propagation ( $K_{IH}$  or  $K_{TH}$ , respectively) and the stress intensity insensitive average rate of crack growth ( $da/dt_{II}$ ). The time to failure will be predicted in a specific application. The resulting values of these material properties are dictated by the specific alloy crystal and interface structures as well as crack tip hydrogen concentration and state of stress. While models of these properties exist, each is supported by only a small segment of experimental data and none are adequately aligned with the broad-modern database developed at UVa and elsewhere. UVa has the unique capability to model both the crack tip hydrogen concentration and resultant damage mechanisms which was demonstrated in N00014-06-1-0366. Coupled with collaborators mentioned, the model outputs from UVa can be extended to predict component crack length and component lifetime. Specific challenge tasks in the present program will be to extend the  $[da/dt]_{II}$  findings towards intermediate levels of cathodic protection where crack growth is slow or non-existent. The threshold and crack growth

models will deal with intergranular, transgranular-brittle subcritical as well as slip-band cracking, while the fracture toughness model is specific to unstable microvoid fracture involving H and interactions with plastic deformation. The model outputs will be  $K_{TH}$  and  $da/dt_{II}$ , each as a function of material and electrochemical conditions.

Such models were extended with the help of VEXTEC, Inc to predict the effect of intermediate cathodic protection levels in mitigating or exacerbating hydrogen assisted cracking of a fastener or alternate-relevant component and/or guide the understanding of the key attributes needed to design a cathodic protection system.

## **TECHNICAL BACKGROUND**

A range of hydrogen assisted cracking problems currently limits use of high strength alloys in the marine environment. In this project, we focused on HEAC due to the concurrent action of applied stress and environmental reaction to introduce damaging atomic hydrogen (H) into Monel K-500. These interactive processes are highly localized at the crack tip. The alloy considered was Monel 5-500 (63Ni-27Cu-3Al-0.5Ti) with principle work to be focused on Monel K-500.<sup>1</sup>

## **SUMMARY**

The crack propagation perspective provides a framework to quantify subcritical cracking phenomena for component life assessment in a marine application. Over the past 25 years, extensive data have been generated to describe cracking in a range of high strength alloys of naval significance. A variety of mechanism-based models have been reported in the literature, derived from this experimentation, but all involve multiple-adjustable parameters associated with uncertainties in the crack tip hydrogen interactions that govern crack initiation and propagation. As such, modeling and simulation have not been used extensively here-to-fore for alloy and protection system development; rather, time consuming experimentation continues to be carried out and results are often explained with questionable-limited speculations. However, improvements to H cracking models are achievable by developing new understanding of crack tip electrochemistry and mechanics, as guided by the existing interdisciplinary experience base. The Monel K-500 alloys system provides an ideal case, of both practical and scientific relevance, to extend understanding of HEAC modeling. By coupling with external definition of the mechanics condition, the lifetime of the component can be estimated as long as the state of stress, material, geometry, electrochemical conditions, and temperature are defined.

## **TECHNICAL APPROACH**

The following approach defines the step-by-step tasks required to complete the objectives established for this extension program. The approaches used to predict crack tip hydrogen concentration and model H cracking properties used for steels also apply to for nickel based precipitation hardened alloys with the challenge that hydrogen diffusivities in the solid state are much lower than in the case of steels.

---

<sup>1</sup> 1. Special Metals product data sheet on Monel Alloy K-500 (UNS N05500), [www.specialmetals.com](http://www.specialmetals.com)

## Predictions of Crack Tip Hydrogen Concentration and Diffusivity

### Task 1-1

Define macro- and micro potential profiles in a generic flooded tank to assess the cathodic protection potentials experienced by Monel k-500 fasteners in flooded spaces subjected to cathodic protection by sacrificial anodes. Assess the local cathodic potential as a function of anode position, tank water depth, cathodic anode potential, and coating quality (0-10% defective). *Portions of this task were conducted by Dr. Francisco Presuel Moreno at Florida Atlantic University, Dept. of Ocean and Mechanical Engineering, 101 North Beach Road, Dania Beach, FL 33004.*

### Task 1-2

Utilize a combination of Newman's Trapezoidal Crack Model, Finite Element Potential Distribution Model, or Experimental Exploitation of Occluded Site Scaling Laws to define local crack tip pH, hydrogen overpotential, and hydrogen production rate as a function of bulk solution composition as well as applied potential, material and geometry. Conduct this analysis specifically for Monel K-500 in alkaline solutions or alkaline seawater. *Portions of this task were conducted by Dr. Francisco Presuel Moreno at Florida Atlantic University, Dept. of Ocean and Mechanical Engineering, 101 North Beach Road, Dania Beach, FL 33004.*

### Task 1-3

Refine analysis of diffusible hydrogen concentrations in alkaline environments applicable to cathodic polarization using a combination of permeation, TDS, barnacle cell methods calibrated by LECO analysis for Monel K-500 precipitation age hardened alloys. Provide revised values of diffusible and trapped hydrogen concentration as a function of potential and pH.

### Task 1-4

Utilize either selected permeation, thermal desorption, NRA or diffusion couple methods to define and refine apparent hydrogen diffusivity for in Monel K-500. Modify as appropriate over length scales relevant to fracture process zones. Provide as inputs to the fracture tasks.

### Task 1-5

Integrate/couple results from Tasks 1-1 to 1-5 to enable prediction of lattice, diffusible and stress/trap modified crack tip hydrogen concentrations as a function of material-geometry-environment for nickel based precipitation age hardened alloys. Predict potential dependency of local tip diffusible hydrogen concentration for a crack tip as inputs to fracture model.

## Predictions of the Effect of Crack Tip H Concentration and Diffusivity on Crack Propagation Properties and Component Performance

#### Task 2-1

Predict HEAC properties,  $K_{IH}$  and  $da/dt_{II}$ , of a given Monel K-500 metallurgical condition as a function of applied cathodic polarization, using integration of state-of-the art crack tip micromechanical modeling, independent electrochemical and H diffusivity inputs from Task 1, and limited cracking experimentation from Task 2.3.

#### Task 2-2

Develop a user-friendly software tool capable of predicting the effect of applied cathodic polarization on the distribution of SCC life of a relevant Navy component using damage tolerant fracture mechanics coupled with input materials HEAC data from Tasks 2-1 and 2-3 plus a probabilistic distribution of surface condition associated with the selected component. This work will be performed by VEXTEC (Dr. Robert Tryon) and leveraged with similar efforts in the areas of 5000-series Al alloy SCC (ONR-sponsored) and ultra-high strength steel HEAC (STTR-II sponsored).

#### Task 2-3

Produce laboratory measurements of HEAC resistance ( $K_{IH}$ ,  $da/dt_{II}$ , and  $da/dt$  vs. stress intensity factor) for a single metallurgical condition of Monel K-500, necessary to: (a) calibrate and validate micromechanical modeling of HEAC behavior vs.  $E_{APPLIED}$  in Task 2-1 and (b) enable prediction of fastener life vs applied stress and cathodic polarization in Task 2-2. This work will be performed by Fracture Technology Associates (Mr. J. Keith Donald) and leveraged with a similar effort in ultra-high strength steel HEAC (STTR sponsored). This work will contribute to development of an ASTM-standardized accelerated test that is capable of enabling quantitative material and component cracking predictions.

#### Task 2-4

Demonstrate and explain the likely deleterious effect of slow but active crack tip strain rate on HEAC kinetics.

### **DELIVERABLES**

This research program delivered the literature publications, important conference participation, and PDRA resources that have been characteristic of UVa research sponsored by ONR. Moreover, a specific deliverable of this current program was a strong coupling between the outputs of our fundamental research and one or more specific applications in US Navy systems as detailed in the next section.

### **TRANSITIONS**

The long range payoff of this research for the USN will be the ability to predict the environmental cracking threshold stress intensity and crack growth rate for any nickel based



alloy such as Monel K-500 and Alloy 718 fasteners in a marine environment, as a function of applied electrochemical potential, defect geometry, alloy metallurgy and state of stress. For instance these alloys are used in flooded spaces and experience various degrees of cathodic protection. Such predictions will be sufficiently quantitative for direct use in component-level analysis including time to failure. The output will be suitable for a range of components but including high strength fasteners, rods and studs in wetted marine environments. The models produced to achieve this capability will ultimately be sufficiently simple to be implemented on a desktop computer in the engineering environment.

The following are examples of specific transitions that have either been achieved or pursued in this project:

1. Drs. Wayne Tucker and Tom Ramotowski of the Naval Underwater Warfare Center have been in preliminary discussions with Profs. Scully and Gangloff regarding Ni-based alloy fastener applications in undersea marine components subjected to cathodic protection. The issue in this case is hydrogen environment embrittlement (HEAC) susceptibility. Our experimental and modeling research was aimed to impact the needs of this group.
2. Dr. Bob Bayles and LUNA Innovations will continue to have an interaction with UVA regarding a hydrogen sensor that seeks to detect HAC conditions in fastener materials.
3. Monel K-500 bolts have been identified and may be made available from Jennifer Gaies of NSWCCD. This was confirmed at the ONR D&I meeting in August 2010 and 2011. The purpose for obtaining these bolts is two-fold. The field data may in principle provide a data base of cracking observations under field conditions needed as a comparison to the model for verification purposes. The challenge is to identify specific field environment and loading conditions, as well as alloy pedigree, associated with a given-failed bolt. Ideally, hydrogen-interactions in actual cracked bolting material must be characterized for each material used for model validation to see if large differences exist from heat to heat or due to processing variations. This information serves as further input to the UVA model in order to provide the necessary parameters to enable most accurate model predictions of field crack growth rate. We have proposed to assist NSWCD and NAVAIR to transition the SCC experimental capability, and software predictive tool, to their laboratory to develop such connections between field observations and laboratory characterizations, underpinned by mechanistic understanding.
4. A second purpose will be to see if hydrogen interactions and crack growth rates vary significantly from heat to heat or from vendor source to source to see if a correlation can be obtained between fast crack growth rates or high HEE susceptibility and certain changes in hydrogen interactions. Tom and Jennifer have been in contact and the ONR sponsor should help, as well, to be sure that the necessary collaboration is encouraged.

## SUMMARY OF PROJECT FINDINGS

1. The rising displacement test method, with continuous-precision dcPD monitoring of a small crack provides an effective-accelerated characterization of environmental cracking in Monel K-500, particularly when augmented to account for artifacts due to crack surface electrical contact, highly localized crack tip plasticity under small-scale yielding, and small-specimen ligament plasticity.
2. For Monel K-500, the rising displacement test method is capable of resolving real crack growth rates of 0.4 nm/s and faster for a constant-applied  $dK/dt$  of 0.3 MPa m/h. This growth rate resolution is directly proportional to  $dK/dt$ , and may depend on alloy strength.
3. An analytical J-integral analysis characterizes HEAC in Monel K-500, without the need to measure displacement or unloading compliance, thus providing material property data for simulation of cracking in a larger and elastically loaded structure.
4. Solution treated and aged Monel K-500 is susceptible to severe intergranular hydrogen environment assisted cracking in NaCl solution when under cathodic polarization in the range of -800 mVSCE and higher. Such cracking is eliminated by reduced cathodic polarization in the range of -750 mVSCE and lower.
5. HEAC in Monel K-500 is exacerbated by rising K and active crack tip strain rate, compared to quasi-static loading, but only for environmental conditions where cracking is mild to moderate.
6. A rescaled crevice model, coupled with measured-local crevice potential and pH, was combined with a H uptake law measured by thermal desorption spectroscopy for Monel K-500, to establish the strong effect of applied potential on crack tip H concentration.
7. Diffusible H concentration produced at the crack tip in Monel K-500 decreased with increasing applied potential and was essentially below the experimental resolution limit for applied potentials above -764 mV SCE.
8. Good agreement between the measured and micromechanical model predicted dependencies of KTH and Stage II crack growth rate on applied-cathodic potential supports the conclusion that a critical level of cathodic polarization must be exceeded before HEAC can progress at a significant rate in Monel K-500 stressed in NaCl. The precise level of this potential could depend on subtle differences in Monel metallurgy through microstructure and composition effects on H uptake, as well as on key parameters in the micromechanical models.

9. A fracture mechanics-based program, *SCCrack*, predicts distributions of cracked component life as limited by HEAC using the input from accelerated laboratory experiments strengthened by electrochemical measurements of crack tip H and micromechanical mechanism-based modeling. The effect of a distribution of applied-cathodic polarization on component life is strikingly strong, reflecting the dominant influence of cathodic polarization on rates of IG HEAC.

#### **SUMMARY OF PRESENTATIONS, POSTER SESSIONS, OR PUBLISHED PAPERS RESULTING FROM THIS PROJECT:**

##### **Papers**

1. Francisco J. Presuel-Moreno, Hung Ha, John R. Scully, "Cathodic Protection Potentials Obtained using Finite Element Modeling for Zinc/intermediate anodes on coated steel proximate to Monel K-500 bolt," in preparation for CORROSION J. (2012).
2. Hung Ha, Francisco Presuel Moreno, John. R. Scully, "Predicting Diffusible Hydrogen Concentrations In Simulated Monel k-500 Crack Tips Using Rescaled Crevices and Finite Element Modeling of Current and Potential Distributions," in preparation for CORROSION J. (2012).
3. J. Ai, H. Ha, R.P. Gangloff and J.R. Scully, "Hydrogen Diffusion, Trapping and Thermal Desorption Energies in a Aged Ni-Cu-Al Alloy: UNS N05500 (Monel Alloy K-500)," submitted to *Acta Metallurgica*, (2012).
4. R.P. Gangloff, H.Ha, J.T. Burns, J.R. Scully, "Measurement and Modeling of Hydrogen Environment Assisted Cracking in Monel k-500," in preparation for Metall. And Materials Trans., (2012).

##### **Presentations:**

1. Francisco Presuel-Moreno, FUA presented a poster at NACE 2011 in Houston.
2. J.R. Scully delivered an invited lecture of Hydrogen Embrittlement of Monel K-500 at Univ. of Rhode Island and NUSC in Sept. 2011. The alloy end users at General Dynamics, NRL, NUWC, and Ametek were briefed.

##### **Conference Proceedings:**

1. Abdullah Al-Rumaih and R.P. Gangloff, "Measurement and Modeling of Temperature Dependent Internal Hydrogen Assisted Cracking in Cr-Mo Steel", in



Hydrogen Effects on Materials, B.P. Somerday and P. Sofronis eds., ASME, New York, NY, in review (2012). 50% supported by ONR and 50% supported by oil companies.

**Book Chapters:**

1. J.R. Scully, Effect of Stress, Environmental Assisted Cracking, Francis LaQue Seawater Corrosion Handbook, second addition, in press (2012).
2. J.R. Scully, "Hydrogen Interactions in Al Alloys," Woodhead Publishing, R.P. Gangloff and B. Somerday editors, (2012).
3. Gaseous Hydrogen Embrittlement of Materials in Energy Technologies: The Problem, Its Characterization, and Effects on Particular Alloy Classes, Volume 1, eds., R.P. Gangloff and B.P. Somerday, Woodhead Publishing Limited, Cambridge, UK, 840 pages (2012).
4. Gaseous Hydrogen Embrittlement of Materials in Energy Technologies: Mechanisms, Modelling and Future Developments, Volume 2, eds., R.P. Gangloff and B.P. Somerday, Woodhead Publishing Limited, Cambridge, UK, 500 pages (2012).

**Task 1**  
**Macropotential Profiles under Cathodic Protection in a Flooded Rectangular Space**

## **Cathodic Protection Potentials Obtained using Finite Element Modeling for Zinc/intermediate Anodes on Coated Steel Proximate to Monel K-500 Bolt**

Francisco J. Presuel-Moreno<sup>1</sup>, Hung M. Ha<sup>2</sup>, John R. Scully<sup>2</sup>

<sup>1</sup>Florida Atlantic University  
Dept. Ocean & Mechanical Engineering  
101 North Beach Road  
Dania Beach, FL 3300

<sup>2</sup>Center for Electrochemical Science and Engineering  
Department of Materials Science and Engineering  
University of Virginia, Charlottesville VA 22904

### **Abstract**

For systems consisting of coated steel that also include high strength fasteners (e.g. Monel K-500 bolts), it is important to know cathodic polarization levels from the stand point of both corrosion protection (both at the fastener and coated steel) and also to avoid coating damage as well as hydrogen embrittlement (particularly at the fastener). In this section, we describe computational effort conducted to better understand polarization levels obtained under various conditions for a system with zinc or intermediate anodes, cathodically protecting coated steel proximate to Monel K-500 bolt. A Finite Element Method commercial software was used to obtain potential distribution across coated steel surface for a generic geometry. The conductivity was assumed to be constant and assumed to be 2 S/m. The tank was assumed to be 20 meters long and 12 meters high. The height of the solution in the tank was varied between 10 m (base cases), 2 m, 1 m and 0.25 m. Three values were assumed for the  $E_{\text{anode}}$ : -1.1 V, -1. V and -0.9 V vs. SCE. It was assumed that the anodes were non-polarizable. The results demonstrate how the anode potential, coating % defect, solution height and geometric distance all control the applied cathodic potential at the Monel K-500 bolt. A 200 mV ohmic potential drop could be obtained when distances were large and the coating possessed 10% defect area. However, the potential drop was negligible when a pristine coating was present. In the case of pristine coatings with little current leakage, the potential of the sacrificial anode material is the dominant factor that controls the potential of a Monel K-500 bolt and anode separation distance has little impact. In the case of a 1-10% defective coating, ohmic voltage drop can be 100-200 mV and anode placement matters. The water height also exhibits strong effects on the potential sensed by an exposed bolt when the coating is defective.

## Introduction

For systems consisting of coated steel that also include high strength fasteners (e.g. Monel K-500 bolts), it is important to know the cathodic polarization level for both corrosion protection (both at the fastener and coated steel) [1-4] to avoid coating damage [1, 5-11] as well as hydrogen embrittlement (particularly at the fastener) [12-17]. In this section we describe computational effort conducted to better understand macro-polarization levels obtained under various conditions for a system with zinc or intermediate anodes and coated steel proximate to a Monel K-500 bolt.

Traditional Zn and Al based sacrificial anodes have a potential of  $\sim -1.1 \text{ V}_{\text{SCE}}$  [18-23]. Intermediate anodes usually have a nobler (less negative potential), in here intermediate anodes were assumed to have a rest potential values of  $-1.0 \text{ V}_{\text{SCE}}$  and  $-0.9 \text{ V}_{\text{SCE}}$ .

## Experimental Procedure

A Finite Element Method commercial software was used to obtain potential distribution across coated steel surface for generic geometry. Figure 1 shows a description of what is being model (1a) and the model abstraction (1b).

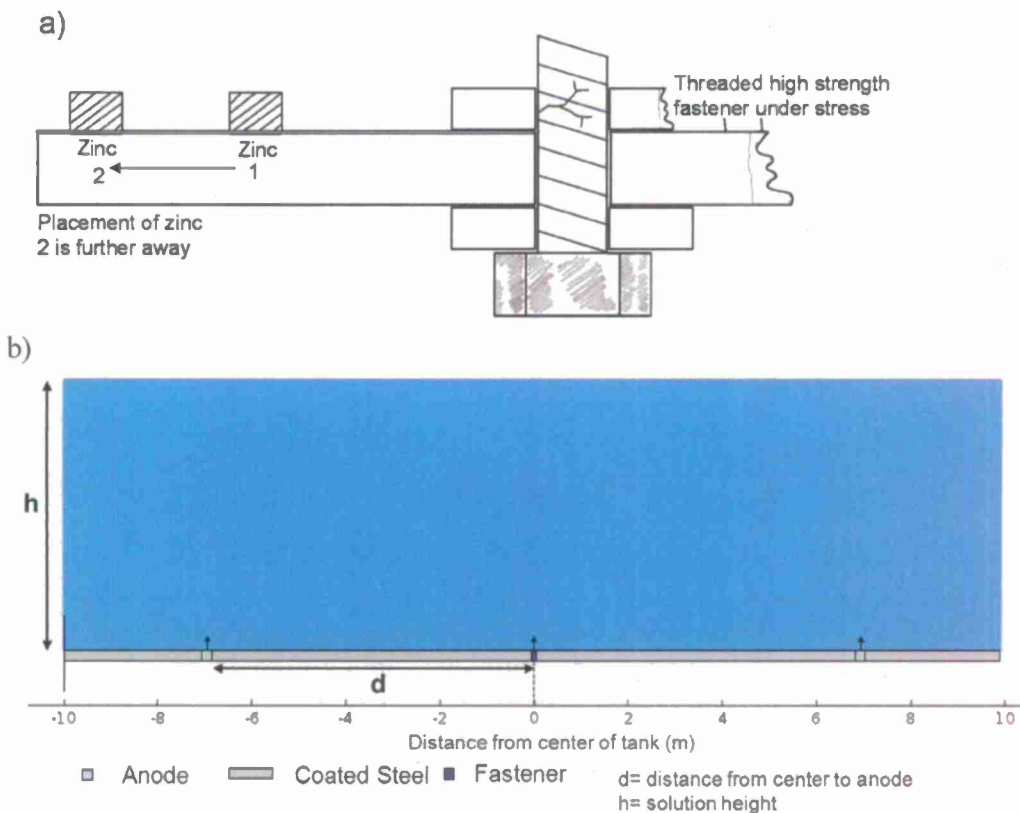


Figure 1. a) system being modeled, and b) model abstraction to be implemented. Three different materials: Zn/intermediate anode, Coated steel and Monel K-500 fastener/bolt.

## Brief Model Description

A commercial FEM was used to solve the Laplacian equation (i.e.  $\nabla^2 \Phi = 0$ ). The system can be exemplified by a ballast tank that is filled with seawater (or partially filled). A two dimensional approach was implemented and assumes non-transient conditions. The conductivity was assumed to be constant and assumed to be 2 S/m. The tank was assumed to be 20 meters long and 12 meters high. The height of the solution in the tank was varied between 10 m (base cases), 2 m, 1 m and 0.25 m. Three values were assumed for the  $E_{\text{anode}}$ : -1.1 V, -1. V and -0.9 V and assumed that the anodes were non-polarizable (i.e. potential constant at the anode)  $\frac{\partial \Phi}{\partial n} = 0$ , or flux equal to zero was

the boundary assumed for the wall on the left, the wall on the right and the interface between air and the solution. The boundary condition at the bottom of the tank for the coated steel and the fastener were given by electrochemical polarization curves obtained experimentally and fitted before placing them in the model (these are non-linear boundary conditions). The fastener was assumed to be at the center of the tank. Two anodes were assumed to be at either side of the fastener. Four distances were considered: 1 m, 3 m, 7 m and 9 m from the center of the tank. Each anode was assumed to be 20 cm long. Three coating conditions were modeled: 1% defective coating, 10% defective coating and pristine coating.

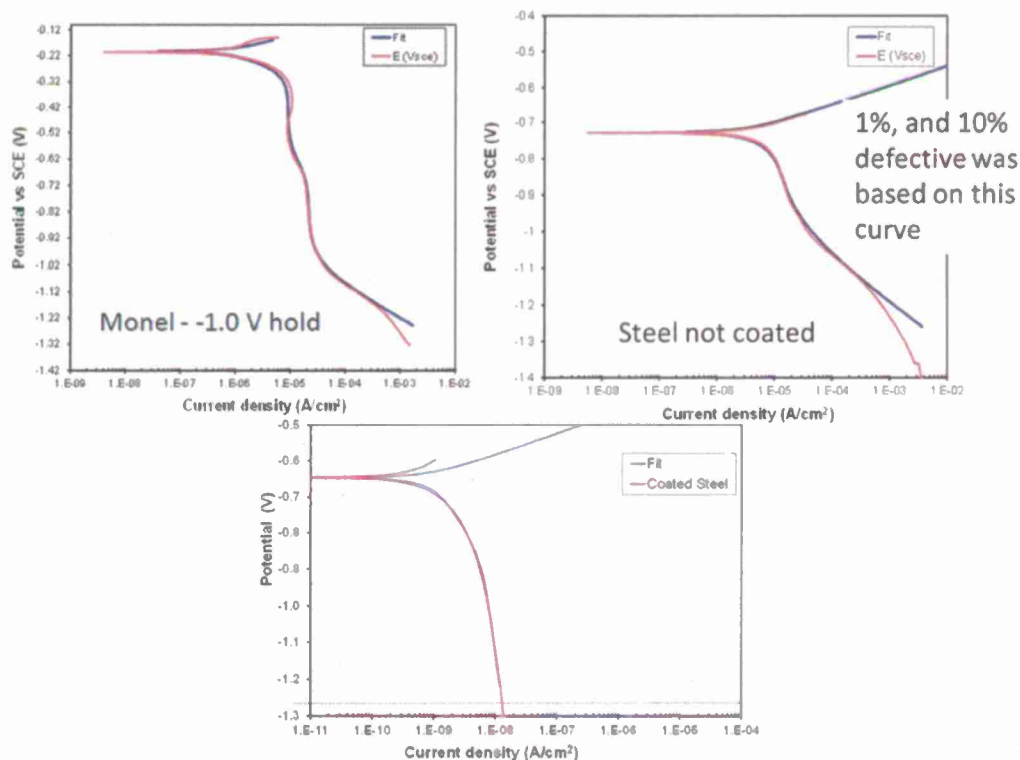


Figure 2. Polarization curves measured in simulated seawater pH 8.2 solution under natural aeration and no stirring.



## Results

The following pages present the computed cases, showing the potential maps obtained and references in general to a scale between -1.1 V and -0.85 V (in some cases to -0.78 V). The effect of anode distance from fastener,  $E_{\text{anode}}$ , coating condition, and water height will be presented.

### *Anode distance*

Anode distance affected the potential distribution. In the case of close anodes at 1 m distance, the potential at an exposed bolt is very similar to the OPC of the anode (Figures 3 to 4). However, at 3, 7 and 9 m, the potential experience at the bolt is 50-100 mV above the OCP of the sacrificial anode. This indicates a small effect of ohmic drop (Figures 3 to 4).

### *Coating Quality*

One of the largest factors is coating quality. There was negligible potential drop in the case of the pristine coating (Figure 5). In this case, the potential of the sacrificial anode sets the potential at the bolt. The plots from Figure 5 show that when the coating is in pristine conditions the fastener is polarized to a value very close to  $E_{\text{anode}}$ . Figures 5 and 6 show that significant polarization is observed throughout the bottom of the tank for cases with 1% coating defective, and the potential gradient is larger for those with 10% coating defective. The ohmic drop can be 100 mV with a 1% defective coating and 200 mV with a 10 % defective coating. However, even with an intermediate  $E_{\text{anode}} = -0.9 \text{ V}_{\text{SCE}}$  the fastener is polarized to  $-0.78 \text{ V}_{\text{SCE}}$  (Figure 6).

### *Solution height*

For cases where the anode is close to the fastener, e.g. 1 m, the net polarization at the fastener remains the same (Figure 7) as the solution height decreases. However, the polarization at the coated steel decreases when the solution height increases (Figure 7). At larger anode distance, e.g. 9 m, as the solution height decreases the polarization at the fastener is significantly reduced (Figure 8) but the polarization at the coated steel increases (Figure 8).

## Discussion

These results indicate that coating quality, anode open circuit potential and water height can all exhibit a large effect on the level of cathodic protection received by a Monel K-500 bolt. Since tank water height and coating quality will inevitably be controlled by other operational factors, this leaves as one thing that can be controlled by the corrosion engineer as the anode OCP. New pristine coatings in conjunction with zinc anodes at -1.1 V vs. SCE will run the risk of polarizing Monel K-500 bolts towards hydrogen embrittlement conditions regardless of zinc anode proximity and points towards the benefits of low voltage anodes.

**Anode Distance – (10% defective,  $h=10$  m,  $E_{\text{anode}}=-0.9\text{V}$ )**

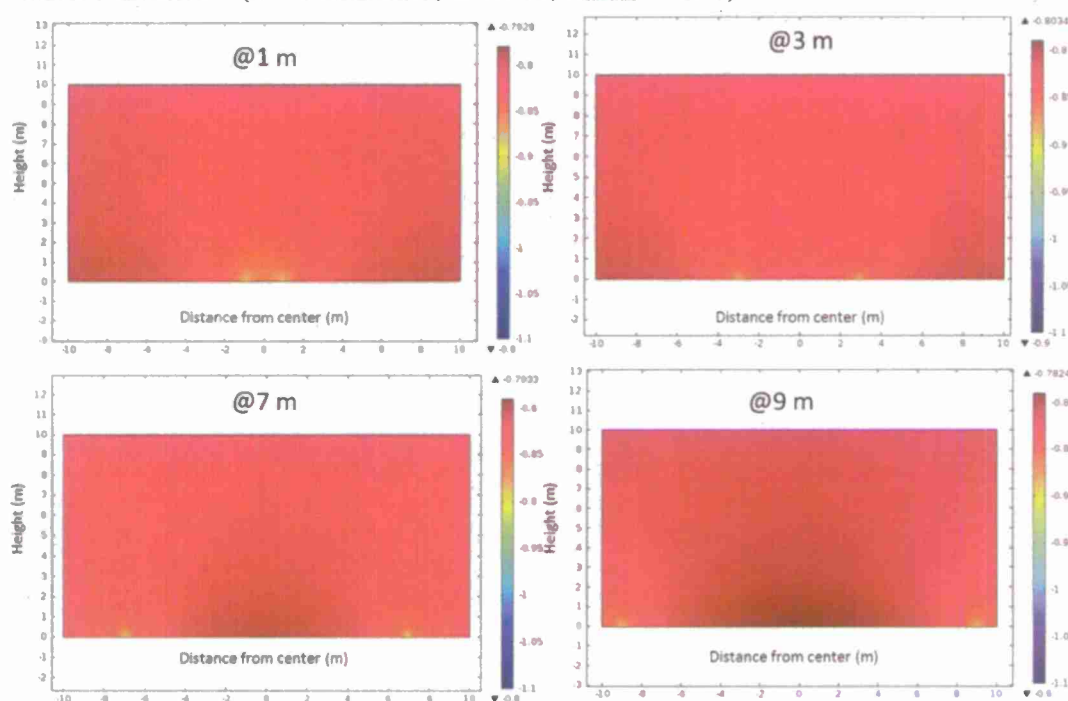


Figure 3. Potential map for cases with anode at various distances from the fastener, coating 10% def.

**Anode Distance – (1% defective,  $h=10$  m,  $E_{\text{anode}}=-0.9\text{V}$ )**

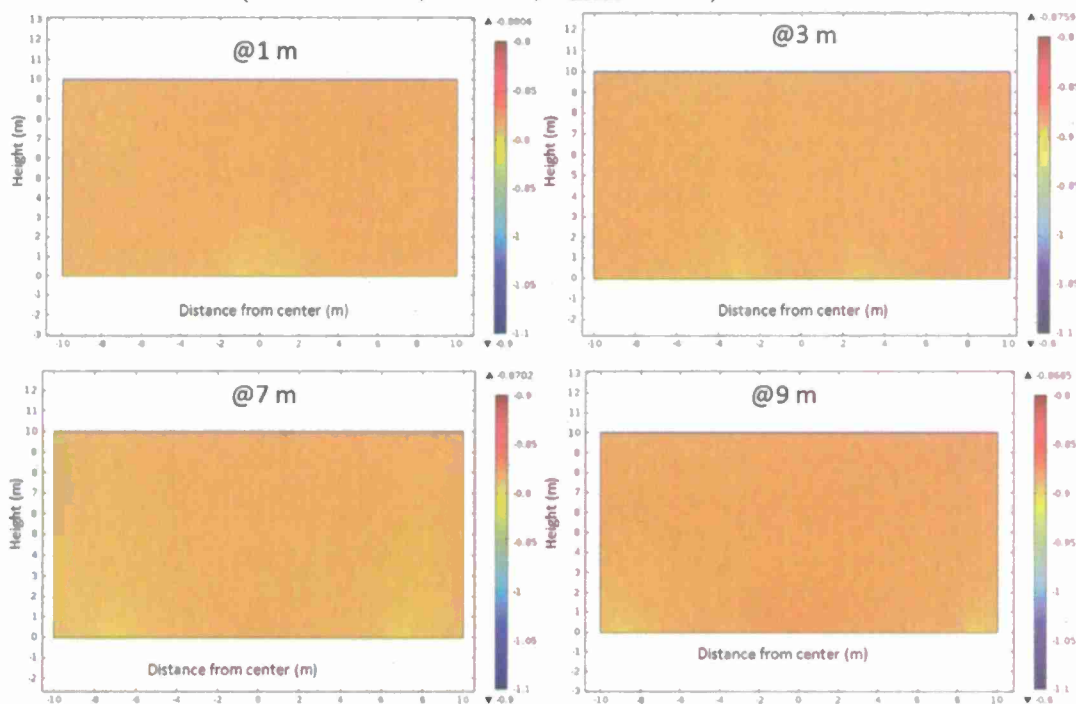


Figure 4. Potential map for cases with anode at various distances from the fastener, coating 1% def.  $E_{\text{anode}}$  effect, anodes at 9 m,  $h=10$  m, 1% coating defective (left) and 10% coating defective (right)

## Coating quality

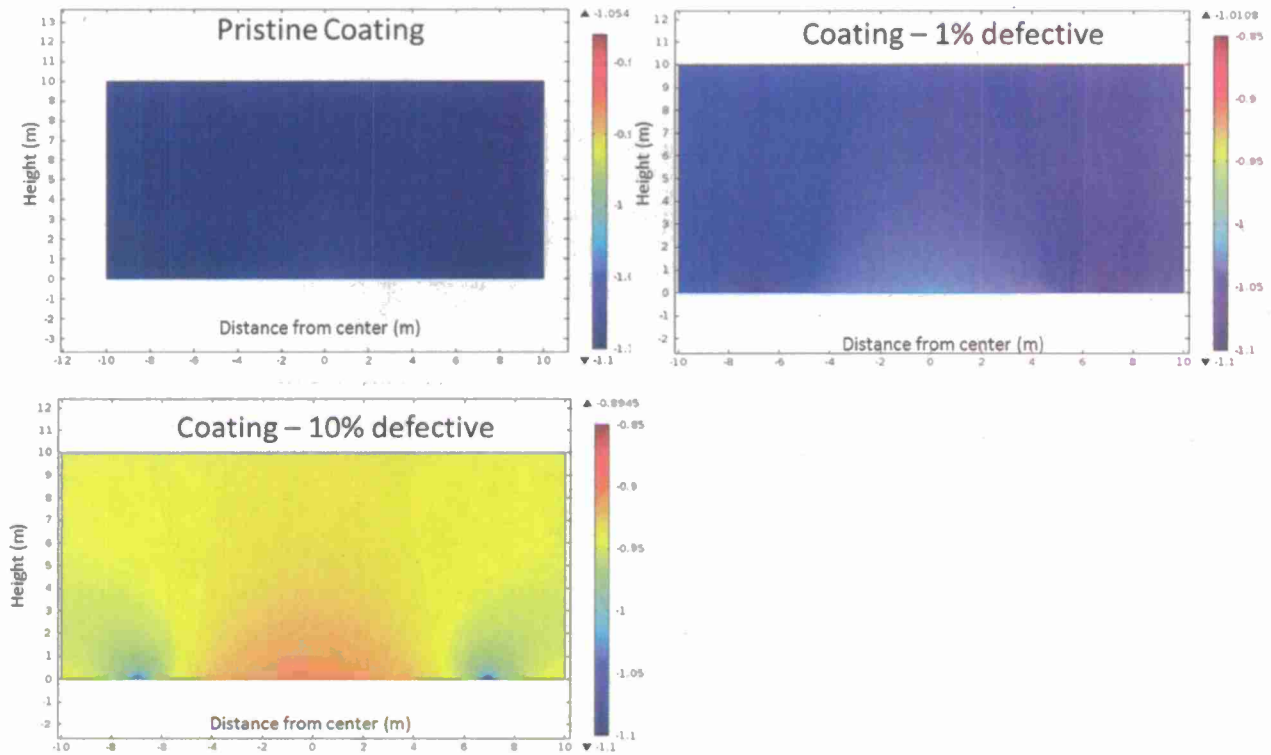


Figure 5. Comparison of coating quality on the amount of polarization for cases with  $E_{\text{anode}} = -1.1 \text{ V}$ ,  $h = 10 \text{ m}$ , anodes at 7 meters from the center of the tank, and  $2 \text{ S/m}$ .

## Coating quality

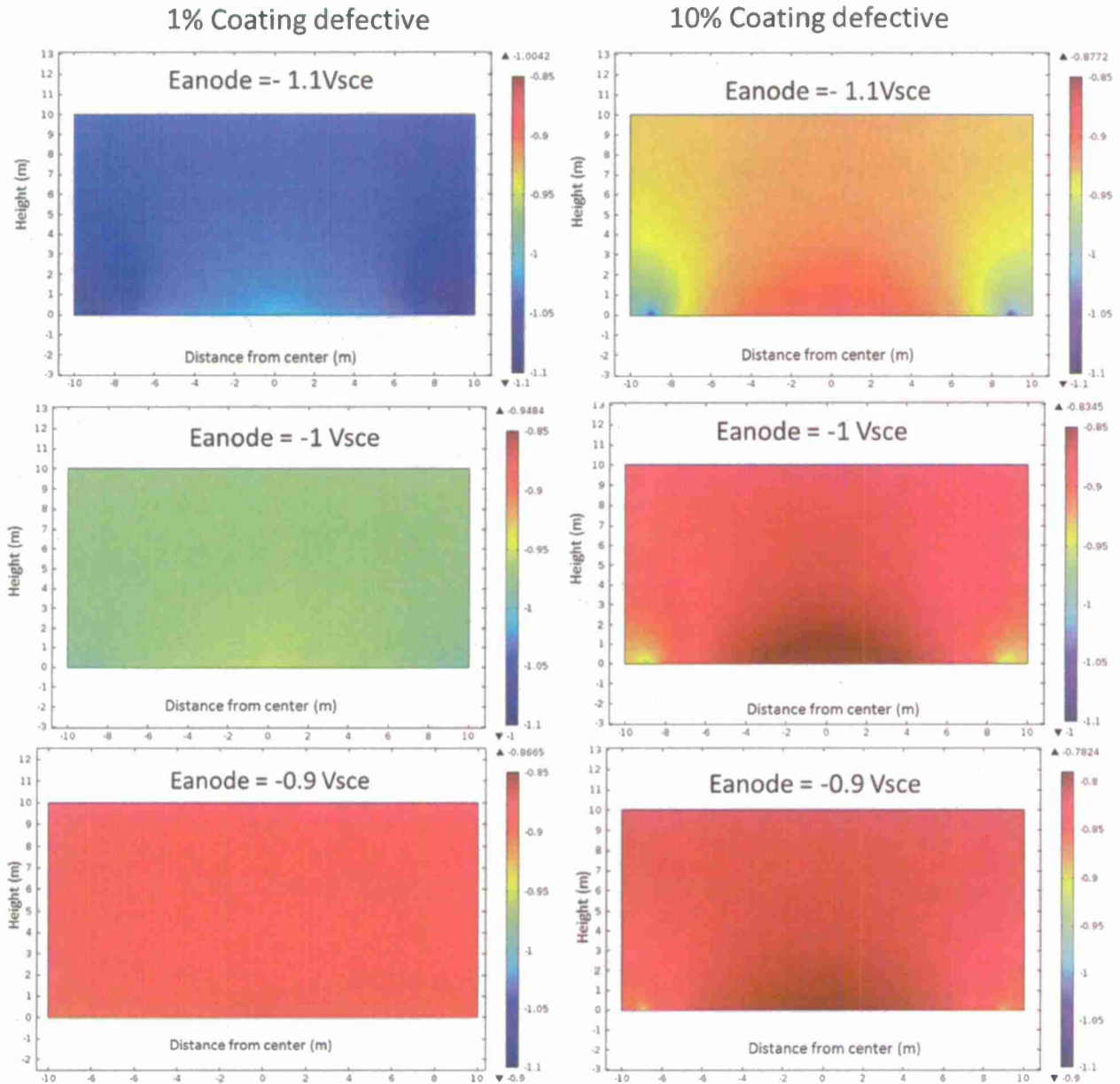


Figure 6. Potential map for Eanode ranging -1.1 V (top row), -1.V (center row), -0.9 bottom row. All cases had  $h = 10$  m, conductivity 2 S/m, anodes at 9 m from the center of the tank. Left column 1% coating defective and right column 10% coating defective

### Solution height effect

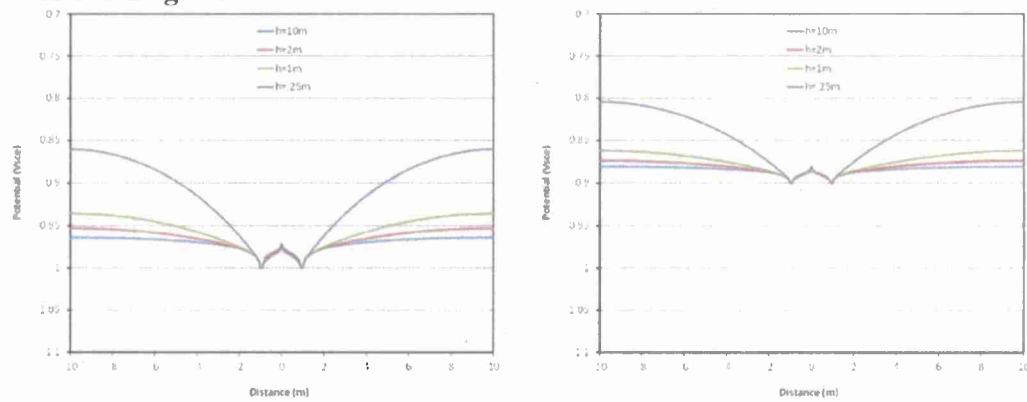


Figure 7. Potential at the bottom of the tank for cases with anodes at 1 m from the center of the tank. 1% defective coating.



## Solution height effect

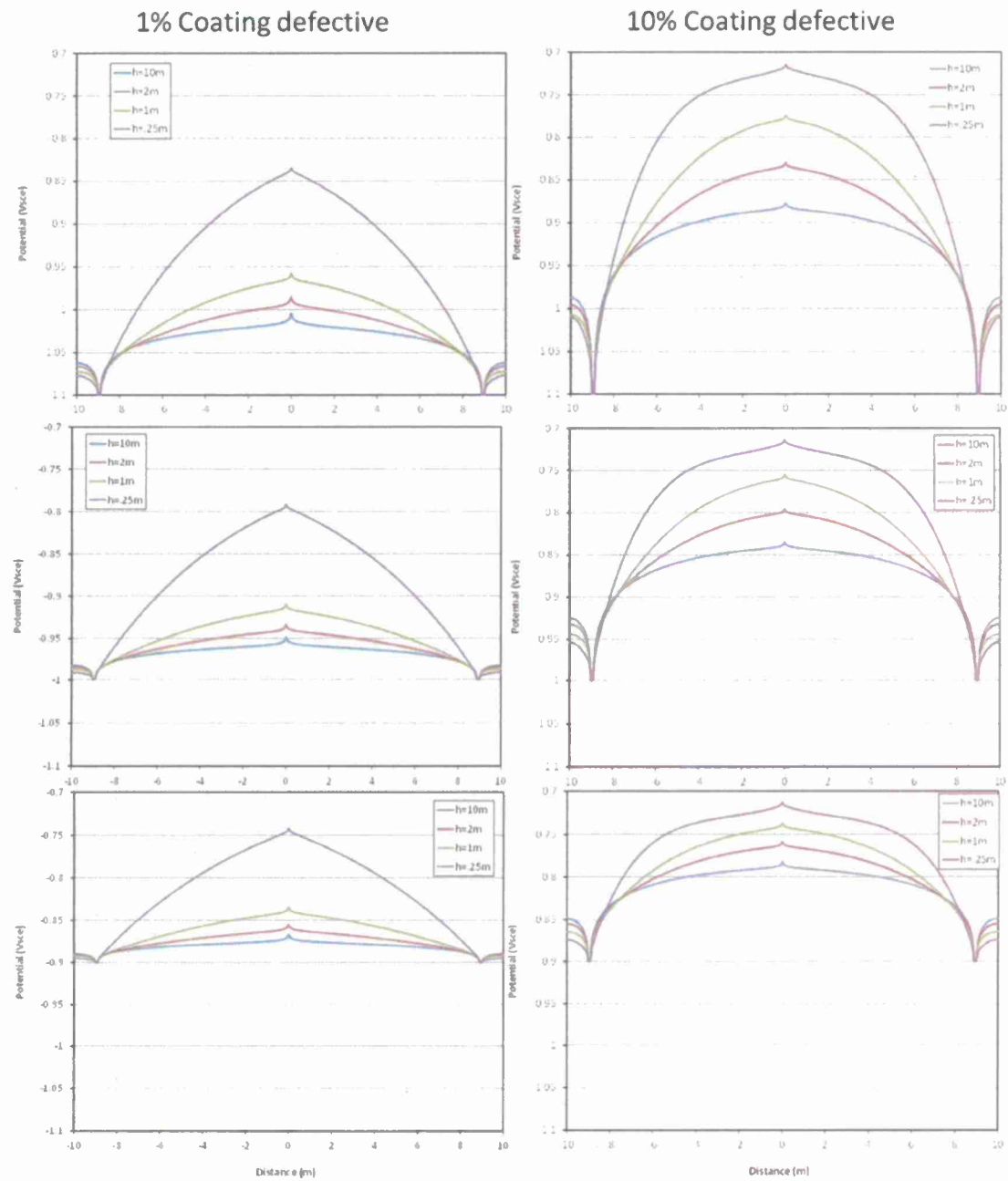


Figure 8. Comparison of solution height on the amount of polarization at the bottom of the tank. Cases with anodes at 9 meters from the center of the tank, and 2 S/m.

### **Conclusion**

These results demonstrate how the anode potential, coating defect area expressed as % defective, solution height and geometric distance all control the applied cathodic potential at the Monel bolt. In the case of pristine coatings with little current leakage, the potential of the sacrificial anode is the dominant factor that controls the cathodic potential of a Monel K-500 bolt and anode separate has little impact. In the case of a 1-10% defective coating ohmic voltage drop can be 100-200 mV and anode placement matters. The water height and anode OCP exhibit strong effects on the potential sensed by an exposed bolt assuming a defective coating but have little influence when the coating was pristine.

### **Acknowledgements**

We gratefully acknowledge support from ONR Grant N00014-10-1-0552 under the direction of Dr. Airan Perez. Special Metals Corporation is also acknowledged for supply of Monel K-500 rod as well as further discussions.

## References

1. X. Chen, X.G. Li, C.W. Du and Y.F. Cheng, *Corrosion Science*, **51**, p. 2242-2245 (2009)
2. I. Martinez, C. Andrade, I. Lasa, O.T. de Rincon and A.A. Torres-Acosta, *Corrosion Engineering Science and Technology*, **42**, p. 215-223 (2007)
3. M. Purcar, B. Van den Bossche, L. Bortels, J. Deconinck and P. Wesselius, *Corrosion*, **59**, p. 1019-1028 (2003)
4. R.A. Gummow, *Materials Performance*, **32**, p. 21-30 (1993)
5. H.C. Bi and J. Sykes, *Corrosion Science*, **53**, p. 3416-3425 (2011)
6. J. Garcia, F. Almeraya, C. Barrios, C. Gaona, R. Nunez, I. Lopez, M. Rodriguez, A. Martinez-Villafane and J.M. Bastidas, *Cement & Concrete Composites*, **34**, p. 242-247 (2012)
7. T. Kamimura and H. Kishikawa, *Corrosion*, **54**, p. 979-987 (1998)
8. O.O. Knudsen and U. Steinsmo, *Corrosion*, **56**, p. 256-264 (2000)
9. S. Martinez, L.V. Zulj and F. Kapor, *Corrosion Science*, **51**, p. 2253-2258 (2009)
10. P.A. Sorensen, K. Dam-Johansen, C.E. Weinell and S. Kiil, *Progress in Organic Coatings*, **68**, p. 283-292 (2010)
11. S. Touzain, Q. Le Thu and G. Bonnet, *Progress in Organic Coatings*, **52**, p. 311-319 (2005)
12. A. Abbassi, A. Mihi and R. Benbouda, *Materials and Corrosion-Werkstoffe Und Korrosion*, **59**, p. 942-947 (2008)
13. M. Cabrini, S. Lorenzi, P. Marcassoli and T. Pastore, *Corrosion Reviews*, **29**, p. 261-274 (2011)
14. G.C. Chai, S. Ronneteg, U. Kivisakk, R.L. Peng and S. Johansson, *Steel Research International*, **80**, p. 482-487 (2009)
15. V. Olden, C. Thaulow, R. Johnsen, E. Ostby and T. Berstad, *Engineering Fracture Mechanics*, **76**, p. 827-844 (2009)
16. M.S. Han, S.K. Jang and S.J. Kim, *Rare Metals*, **30**, p. 633-638 (2011)
17. B. Isecke and J. Mietz, *Steel Research*, **64**, p. 97-101 (1993)
18. M.R. Saeri and A. Keyvani, *Journal of Materials Science & Technology*, **27**, p. 785-792 (2011)
19. E. Tada and H. Kaneko, *ISIJ International*, **51**, p. 1882-1889 (2011)
20. T. Nakagawa, R. Sumi and H. Kaneko, *Journal of the Japan Institute of Metals*, **74**, p. 77-84 (2010)
21. A. Keyvani, M. Emamy, M. Saremi, H. Sina and M. Mahta, *Iranian Journal of Chemistry & Chemical Engineering-International English Edition*, **24**, p. 1-8 (2005)
22. B. Jabeera, T.S. Anirudhan and S.M.A. Shibli, *Journal of New Materials for Electrochemical Systems*, **8**, p. 291-297 (2005)
23. R.J. Kessler, R.G. Powers and I.R. Lasa, *Materials Performance*, **35**, p. 11-15 (1996)

### **Task 1**

**Diffusible and Trapped Hydrogen Concentrations in Monel k-500 as a  
function of Cathodic Potential**

# **Hydrogen Diffusion and Trapping in a Precipitation Hardened Nickel-Copper-Aluminum Alloy Monel K-500 (UNS N05500)**

Jiahe Ai, Hung Ha, Richard P. Gangloff and John R. Scully

Center for Electrochemical Science and Engineering, Department of Materials Science and  
Engineering, University of Virginia, Charlottesville, Virginia 22904, USA

Corresponding Author: J. R. Scully (jrs8d@virginia.edu)

## **Abstract**

Hydrogen uptake, diffusivity, and trap binding energies were measured for several microstructures of Nickel-Copper-Aluminum Alloy Monel K-500 (UNS N05500). Diffusible atomic hydrogen (H) concentration increased from 0 to 90 wppm as the cathodic over-potential decreased to  $-0.5 V_{SCE}$  in alkaline 3.5% NaCl electrolyte at 23°C. The room temperature H diffusion coefficient ranged from 0.9 to  $3.9 \times 10^{-14} \text{ m}^2/\text{sec}$  for single phase solid solution to aged as well as cold worked then aged microstructures. Diffusivity depended weakly on this range of metallurgical conditions, with slower H diffusion after aging. The apparent activation energy for H diffusion was in the range of 29 to  $41 \pm 1.5 \text{ kJ/mol}$  at the 95% confidence level. The lower value represented nearly perfect lattice transport, while the latter was strongly influenced by traps of low-intermediate strength. Atomic hydrogen trapping at metallurgical sites, strongly suggested to be spherical-coherent  $\gamma'$  ( $\text{Ni}_3\text{Al}$ ) precipitates, was evident in the aged compared to the SHT + water quenched condition. Both thermal desorption and classical Oriani trap state analyses suggested that the trap binding energy of H at  $\text{Ni}_3\text{Al}$  ( $10.2 \pm 4.6 \text{ kJ/mol}$ ) was significantly less than the activation energy for perfect lattice diffusion ( $25.6 \pm 0.5 \text{ kJ/mol}$ ) in this nickel-based alloy system.



## Introduction

Monel Alloy K-500 (UNS N05500) is a precipitation-hardenable nickel-copper (64%Ni-30%Cu-3%Al, wt. %) alloy strengthened by a combination of cold work and age hardening to form fine coherent precipitates [1]. The aged alloy contains spherical, coherent  $\text{Ni}_3(\text{Al},\text{X})$  and  $\text{Ni}_3\text{Fe}(\text{Al},\text{Fe})$  phases, with the former known as  $\gamma'$  where  $\text{X}=\text{Cu}, \text{Mn}, \text{Ti}$  or  $\text{Si}$ , present in a Ni-Cu face centered cubic solid solution [2]. The misfit strain is small which accounts for the spherical shape [3]. Notably these spherical, homogeneously nucleated and uniformly distributed precipitates are absent in alloys solution heat treated (SHT) above  $750^\circ\text{C}$  and rapidly water-quenched (W.Q.) [2]. This differs from other Ni-Al and Ni-Ti alloys where  $\gamma'$  forms readily on quenching [4]. The precipitates can form 6-7% by volume upon aging at  $700^\circ\text{C}$  or less, and remain spherical and coherent during coarsening [2]. Incoherent  $\text{TiC}$  phases also form in SHT/W.Q. alloys, but exhibit little shape or size change with aging [2].  $\text{M}_{23}\text{C}_6$  carbides where  $\text{M}=\text{Mn}, \text{Fe},$  or  $\text{Ni}$  form on isolated grain boundaries in Monel K-500 aged for long times. Lastly, annealing twins are prevalent in SHT/W.Q., air-cooled, or aged material; but their interface energy is believed to be a small percentage of the grain boundary energy [2, 5]. These metallurgical features are pertinent to H uptake and diffusion in Ni-Cu-Al alloys such as Monel K-500.

Monel K-500 was believed to be relatively immune to hydrogen environment assisted cracking (HEAC) and stress corrosion cracking (SCC) in various natural environments [6]. Stress corrosion cracking in  $\text{H}_2\text{S}$  environments under high stress, high pressure and temperature steam, in HF vapors, and in Hg was noted for Monel 400 or aged Monel K-500 [7]. Reports also began to indicate susceptibility to room temperature hydrogen environment embrittlement [8-10],

mainly seen as reductions in tensile ductility and notch strength ratio upon cathodic charging. Embrittlement of SHT/aged Monel K-500 (Rockwell C 25-35) occurred in seawater at room temperature when coupled to zinc and where dissolved hydrogen levels increased during prolonged exposure (8 weeks) to 50 wppm. A dynamic plastic strain rate effect was also observed even for pre-charged material [9, 11].

Since these initial reports, nickel-copper alloy bolt failures have been observed in age hardened Monel K-500 subjected to cathodic polarization. Failures by intergranular cracking were attributed to hydrogen production, uptake, and embrittlement as a result of cathodic polarization such as when coupled to aluminum anodes in seawater [7, 11]. This was first attributed to high thread root hardness (~HRC 39) due to age hardening after thread machining. Annealing then age hardening was recommended after threading to maintain hardness below a proposed limit (HRC 35) for Monel K-500 in sour systems. However, additional failures have occurred in roll-threaded Monel K-500 bolts annealed at 980~1050°C, water quenched, and precipitation hardened at 500~600°C for 16 h producing a Rockwell C hardness of only 25 [11]. This level is below one limit recommended by a U.S. Federal Specification for aged round products [12]. Embrittlement failures also occurred in bolts after about one year under a load of about 60% of the tensile yield strength and cathodically protected with anode grade aluminum, even after issuance of modified specifications [7, 11]. Intergranular cracking was reproduced in Monel K-500 under slow strain rate testing in air after H pre-charging when coupled to Al, or charged potentiostatically (annealed and SHT/aged Monel K-500), and to a lesser extent when coupled to steel or potentiostatically polarized to -800 mV vs. Ag/AgCl (STA/aged) in ASTM artificial ocean water [13].

The HEAC behavior of Ni-based superalloys stressed in gaseous  $H_2$  and various aqueous exposures has been reviewed in detail elsewhere [14]. The severity of this cracking problem is apparent in many nickel base alloys such as Alloy 718 [14]. However, few studies have documented the threshold stress intensity ( $K_{th}$ ) for HEAC of Monel K-500 and there are no reports on crack growth rate data for controlled testing. In limited work,  $K_{th}$  for aged Monel K-500 ( $R_C$  30) decreased from above  $70 \text{ MPa}\sqrt{\text{m}}$  at  $-0.7 V_{SCE}$  to less than  $18 \text{ MPa}\sqrt{\text{m}}$  when stressed in room temperature NaCl solution at  $-1.0 V_{SCE}$ , but crack growth rates were not reported [15]. Moreover, little is known about hydrogen uptake, transport and trapping behavior in this alloy that would contribute to a quantitative understanding and micromechanical model prediction of HEAC [14]. The effective hydrogen diffusion coefficient in pure, single crystal Ni was reported to be  $8.4 \times 10^{-10} \text{ cm}^2/\text{sec}$  at  $23^\circ\text{C}$  with an activation energy of  $39.5 \text{ kJ/mole}$  [16]. Computation using transition state theory indicates that the activation energy reaches  $45.7 \text{ kJ/mole}$  for a perfect Ni lattice [16]. A Ni-30 at. % Cu alloy had a hydrogen diffusivity of  $3 \times 10^{-10} \text{ cm}^2/\text{sec}$  at  $23^\circ\text{C}$  and an activation energy of  $\sim 41 \text{ kJ/mole}$  [13]. Limited data on hydrogen transport have been reported for Monel K-500 [17]. The effective diffusion coefficient which may be H-trap sensitive,  $D_{eff}$ , was reported to be  $5.6 \times 10^{-11} \text{ cm}^2/\text{sec}$  at  $23^\circ\text{C}$  [17] for material that was SHT at  $950^\circ\text{C}$ , which is well above the  $\gamma'$  solvus and radiatively cooled. The microstructure and hardness were not reported, and the degree of aging upon cooling was uncertain. Aged alloy X-750 (Ni-Cr-Fe-Al-Ti) shows a drop in effective hydrogen diffusivity of about a factor of nine from pure Ni, which is attributed to composition differences and H trapping at (Ti,Nb)C particles. An additional decrease by a factor of five in effective diffusivity was attributed to precipitation of  $\gamma'$   $\text{Ni}_3(\text{Al,Ti})$  [18]. These results substantiate the importance of H trapping in nickel based alloys and demonstrate that trapping depends on composition and microstructure in Ni-based alloys.

H-metal-microstructure interactions likely differ between Monel K-500, other nickel base alloys and high strength steels. This is because the activation energy for perfect lattice diffusion is low in high strength steel (i.e., 7 kJ/mol), while trap binding energies can be as high as 65 kJ/mole [19]. In contrast, nickel based face centered cubic lattices have high activation energies (~40 kJ/mol). Moreover, possible trapping sites will differ for precipitation hardened *fcc* Ni-based alloys compared to ferrous martensitic microstructures which also contain precipitates. Hydrogen assisted cracking susceptibility of many metals and alloys in aqueous environments is controlled by and increases with the crack tip diffusible hydrogen concentration which is, in turn, controlled by the hydrogen overpotential and production rate [20]. Metallurgical trap states are important and either serve as benign sinks for hydrogen, function as crack tip damage initiation sites and the crack propagation path itself, or function as a reservoir of hydrogen that can be supplied to the tensile triaxial stress field of the stationary or moving crack tip [17, 21-23]. Additionally, Stage II environmental crack velocities,  $[da/dt]_{II}$ , at the upper bounds of hydrogen uptake rates, where cracking is not surface uptake limited, are often controlled by the  $D_{eff}$  in the zone of material at the crack tip [23]. These parameters likely differ between SHT, cold worked and aged Monel K-500 and may help explain observed differences in HEAC susceptibility. For these reasons, the diffusible hydrogen concentration,  $C_{H,diff}$ , absorbed in the nickel base alloy as a function of cathodic potential, and  $D_{eff}$  for Hare critical to understand and model  $[da/dt]_{II}$  and  $K_{th}$  for Monel K-500. However,  $C_{H,diff}$  behavior has not been established as a function of hydrogen overpotential or cathodic hydrogen production rate for Monel K-500. Moreover,  $D_{eff}$  and trapping behavior have not been elucidated over a range of technologically significant microstructural conditions that include various combinations of solution heat treatment, cooling rate, cold work and aging time/temperature.

The objective of this study was to characterize  $C_{H,diff}$ ,  $D_{eff}$ , and microstructural H trapping behavior in Ni-Cu Monel K-500 by comparing SHT and water-quenched, SHT + artificially aged, SHT + cold worked, as well as SHT + cold-worked + aged variants of this alloy. Experimental data were acquired by the thermal desorption spectroscopy (TDS) method enabled by temperature programmed desorption, as well as by electrochemical hydrogen desorption methods.

## **Materials and Experimental Procedures**

### ***Materials***

Monel Alloy K-500 (UNS N05500) from two Special Metals Corp. lots with the compositions given in Table 1, were subjected to various heat treatments. One group was cut from rod which was solution heat treated (SHT) at 982°C (1800°F), aged at 593°C (1100°F) for 16h, then at 538°C (1000°F) for 6h, then at 482°C (900°F) for 8h and finally air-cooled. This condition is labeled SHT + aged. Solution heat treated (at 1038°C (1900°F)) + air-cooled Monel K-500 with subsequent 32% cold drawing (SHT+AC+CW) was also tested. This microstructure was further aged (SHT+AC+CW + aged) at 534°C (~1000°F) for 10h followed by cooling to 481°C (~900°F) at a rate of 15°F/h, and then holding at 481°C (~900°F) for 9.5h and finally air-cooling. One set of samples (19.3 mm diameter and 3 mm thickness) was solution heat treated at 1066°C for 1 h and then WQ, while another set of samples (19.3 mm diameter and 3 mm thickness) was SHT at 1038°C for 1 h then air cooled to investigate SHT+ WQ compared to SHT + AC microstructures. The hardness of samples after various heat treatments was measured using the appropriate Rockwell scale; an average was reported from at least five measurements and converted to the Brinell scale.



Microstructures were etched in Glyceria (50 mL glycerol + 20 mL 12 N HCl + 10 mL 15 N HNO<sub>3</sub> for 5 to 20 minutes) and observed by Scanning Electron Microscopy (SEM). X-ray diffraction (XRD) was utilized to identify precipitated phases. Precipitates for XRD analysis were extracted electrolytically in a solution of 1 wt.% (NH<sub>4</sub>)<sub>2</sub>SO<sub>4</sub> + 2 wt.% citric acid + H<sub>2</sub>O at an applied voltage of 20 V and room temperature [24], where the  $\gamma$  matrix was dissolved but metal carbides and precipitates were extracted then separated by centrifugation.

### ***Hydrogen Charging***

H charging for TDS analysis was conducted by cathodic polarization of Monel K-500 (0.20~0.30 mm thick or thinner) for time (t) estimated to produce saturation based on  $(D_{\text{eff}}t)^{1/2}$  calculations. The specimens were polished to 600 grit, followed by ultrasonic degreasing in methanol, and charged under three conditions. For saturation curve analysis,  $300 \pm 10$   $\mu\text{m}$  thick samples were H-charged for various times at room temperature and -0.9 V vs. SCE in 0.0214 M Na<sub>2</sub>B<sub>4</sub>O<sub>7</sub>·10H<sub>2</sub>O + 0.1144 M H<sub>3</sub>BO<sub>3</sub>(pH ~8.4). The second group was charged at 60°C and -1.475 V with respect to saturated MMSE for 10 days in 0.0214 M Na<sub>2</sub>B<sub>4</sub>O<sub>7</sub>·10H<sub>2</sub>O + 0.1144 M H<sub>3</sub>BO<sub>3</sub> (pH ~8.4) solution. The third group was H-charged for 10 days at room temperature at potentials ranging from -0.7 to -1.20 V vs. SCE in 0.6 M NaCl solution with the pH adjusted to 8.0 using NaOH solution to simulate seawater. All results are reported versus the hydrogen overpotential with respect to the reversible hydrogen potential. Potentials were also retained due to their technological significance with regard to cathodic protection in seawater. All solutions were prepared with 18.2 M $\Omega$ .cm deionized water. The pH was checked each day and adjusted if necessary.

TDS data was reported in the form of integration of hydrogen partial pressure after background subtraction, and conversion to mass of H per the mass of Monel K-500 as discussed elsewhere [25, 26]. This was independently corroborated with LECO hydrogen measurements according to ASTM Standard E1447-09/CTP 3008-1/IG using heating to 650°C [27, 28]. The hydrogen concentrations obtained by integration of TDS data heated to 550°C were multiplied by a calibration factor of 6.37 in the case of Figure 13, given the fact that the hydrogen concentrations measured by LECO method were 6.37 times higher than those determined by TDS under identical hydrogen charging conditions.<sup>1</sup>

#### ***Determination of $C_{H,diff}$ by Barnacle Cell Analysis***

An electrochemical extraction method [27, 28] was used to determine  $C_{H,diff}$ . Extraction occurred immediately after the hydrogen charging in Borate buffer solution (0.10 M  $H_3BO_3$  + 0.10 M NaOH at pH = 10) via hydrogen oxidation at -0.85 V vs. MMSE (-1.206 V vs. MMSE is the reversible hydrogen electrode potential for this pH). The solution was continuously de-aerated with  $N_2$  gas. Hydrogen charged samples were transferred to an extraction cell and slightly abraded with a 600 grit SiC paper.  $C_{H,diff}$  data were calculated from the first half hour of extraction using Equation 1 and assuming two plausible values of  $D_{eff}$  obtained from isothermal thermal desorption results extrapolated to room temperature.

$$C_{H,diff} = \frac{J_t}{zF} \left( \frac{D_{eff}}{\pi t} \right)^{-1/2} \quad (1)$$

---

<sup>1</sup>The difference in heating temperature was regarded to have a minor impact on the hydrogen concentration reported because no hydrogen peaks were observed above about 400 °C during TDS experiments. This does not assure an addition peak between 550-650 °C is not possible but the binding energy for such a trap state would exceed 130 kJ/mole.

where  $J_i$  is the current density associated with hydrogen egress and oxidation ( $A/cm^2$ ),  $z$  is the charge associated with hydrogen oxidation (1 equivalent/mole),  $t$  is the extraction time in seconds,  $F$  is Faraday's constant (96,498 coulombs/equivalent) and  $D_{eff}$  is the effective diffusion coefficient for hydrogen ( $cm^2/sec$ ). Equation 1 is valid as long as  $L^2/D_{eff}t_{max} < 4$  is satisfied where  $L$  is the depth over which a uniform  $C_{H,diff}$  is extracted and  $t_{max}$  is extraction time. The uniform  $C_{H,diff}$  condition was ensured for all experiments because maximum extraction times were over hundreds of seconds while charging times were over days. The extraction current density-time decay was corrected for background current. For consistency and comparison amongst solutions, the overall  $C_{H,diff}$  was calculated at an extraction time of 100 s and selected from a region with a slope of near -0.5.

#### ***Thermal Desorption Analysis of $D_{eff}$ , Apparent Activation Energy for H Desorption and Trap Binding Energy***

Hydrogen egress was measured by isothermal TDS in the range of 125~275°C as discussed elsewhere [19-22, 25]. The desired temperature was stabilized prior to specimen loading into the test chamber.  $D_{eff}$  versus temperature was obtained from isothermal outgassing from  $t_{0.5}$ , which is the time of outgassing when half of the total hydrogen absorbed is removed for a given flat specimen thickness [22, 29]. Egress half times were corrected for specimen heating time assuming isothermal heating of a thin specimen [30]. At low egress temperatures this correction was minor. The temperature dependence of effective H diffusivity was described by:

$$D_{eff}(T) = D_{o\,eff} \exp\left(-\frac{E_m^{app}}{RT}\right) \quad (2)$$

where  $D_{o\,eff}$  is the pre-exponential factor including a jump frequency term and  $E_m^{app}$  denotes

potentially trap affected “apparent” activation energy. The slope of  $\ln D_{\text{eff}}$  vs  $1/T$  was fit to experimental data with a 95% confidence limit on the slope and multiplied by  $R$  to obtain the  $\pm E_m^{\text{app}}$  values reported.

$D_{\text{eff}}$  was also determined from the increase in integrated-absorbed hydrogen level in a plate of known thickness,  $l$ . The solution of the diffusion equation when uptake is considered to be a diffusion controlled process with a constant  $D_{\text{eff}}$  [31] is:

$$\frac{M_t}{M_\infty} = 1 - \frac{8}{\pi^2} \sum_{m=0}^{\infty} \frac{1}{(2m+1)^2} \exp\left\{-D_{\text{eff}}(2m+1)^2 \pi^2 t / l^2\right\} \quad (3)$$

where  $M_t$  is the total amount of H absorbed by the sheet at time  $t$ , and  $M_\infty$  is the equilibrium sorption attained theoretically after infinite time. The following equation was used when the half-time  $t_{0.5}$  of an absorption process is measured [31]:

$$D = 0.049 \cdot l^2 / t_{0.5} \quad (4)$$

Experimental  $M_t$  data were obtained at various charging times by integrating the quantity of hydrogen outgassed during temperature programmed desorption.  $M_\infty$  was taken as the amount of hydrogen in a H saturated sample after 1000 h of charging. Background hydrogen signals were subtracted from  $M_t$  by ramping an empty TDS chamber. Moreover, a plot of experimental  $M_t/M_\infty(t)$  versus  $t^{1/2}$  was compared to a plot of Equation 3 assuming various values for  $D_{\text{eff}}$ .

Desorption energies,  $E_d$ , were determined from ramped TDS. Thermal desorption of H from a homogeneously charged specimen is described by [32, 33]:

$$\frac{dX_d}{dt} = v_x (1-X_d)^n \exp\left(\frac{-E_d}{RT}\right) \quad (5)$$

where  $X_d$  is the fraction of an integrated quantity of H desorbed from a single desorption site and single resolved TDS intensity peak,  $v_x$  is a constant,  $E_d$  is the activation energy for H desorption,  $R$  is the gas constant (8.31 J/mol-K), and  $T$  is absolute temperature.  $E_d$  can be calculated for each desorption site observed using ramped TDS data obtained at different heating rates which produce a different desorption peak temperature,  $T_m$ . The  $T_m$  increases with heating rate,  $dT/dt$ , as demonstrated in TDS and differential thermal analysis,  $E_d$  depends on  $T_m$  and  $dT/dt$  according to [34]:

$$\frac{d \left[ \ln \left( \frac{dT/dt}{T_m^2} \right) \right]}{d[1/T_m]} = -\frac{E_d}{R} \quad (6)$$

$E_d$  was calculated from the linear regression of the slope of  $\ln[(dT/dt)/T_m^2]$  vs  $1/T_m$  data, obtained from desorption maxima observed from experiments as a function of  $dT/dt$ . A slope was fit to the experimental data with a 95% confidence limit and multiplied by  $R$  to obtain the  $\pm E_d$  values reported. In the case of multiple peaks, OriginPro 7.5 was used to perform non-linear curve fitting of the TDS measurements based on a Gaussian model to extract  $T_m$  for individual and sometimes overlapping peaks. Individual peak heights and widths were chosen by the software when the sum of the peak areas of individual peaks matched the peak area for the experimental data. The lowest  $T_m$  value observed was assumed to be the lattice hydrogen concentration in accordance with trap theory [35]. The  $E_d$  values were used to estimate the binding energy for H trapping associated with each of the observed states with a trap binding energy  $E_b$ .  $E_d$  was assumed to equal  $E_m + E_b$ , where  $E_m$  is the activation energy for H diffusion by an interstitial jump mechanism in the trap-free or perfect lattice. This sum is a valid description of the energetics of desorption provided that detrapping and lattice diffusion are the dominant processes

during H desorption and the activation energy barrier for trapping equals  $E_m$  while detrapping to interstitial sites equals  $E_m + E_b$ .

## Results

### *Microstructure and Hardness of Monel K-500*

A typical microstructure of SHT + aged K-500 is shown in Figure 1(A). EDX analysis indicates that there are carbides (Ti-rich)C (Fig.1(B)) and inclusions (Mg, Mn, Al, Ti, Fe)S (Fig.1(C)). The  $\gamma$ -matrix was electrochemically dissolved and metallic carbide MC and  $\gamma'$  phases were extracted and separated [24]. Plotted in Figure 2 are the XRD patterns for the extracted phase(s). The  $Ni_3Al$   $\gamma'$  phase was clearly detected in (A) SHT + aged, (B) SHT+AC+CW and (C) SHT+AC+CW+aged cases. The  $\gamma'$  phase was also present in the SHT + AC case, but notably absent from the SHT+WQ microstructure but only when thin sections were rapidly cooled. Figure 1 showed that TiC and possible  $Cr_{23}C_6$  were present in a very small amount which was not resolved by XRD. Quantitative analysis indicated that the extracted precipitate phases accounted for approximately 4.6wt% of the dissolved alloy in the SHT+aged case, compared to 14.4 wt% for the SHT+AC+CW+aged case, but only 1.8 wt% in the SHT+AC and about 1.6wt% in the SHT+AC+CW case. The similar-low amounts of  $\gamma'$  in SHT+AC cases with and without cold-worked material can be attributed to the fact that air cooling after SHT was not fast enough to avoid nucleation and growth of the precipitate. Notably, cold work did not exacerbate  $\gamma'$  formation during this cooling, but CW did promote  $\gamma'$  precipitation during isothermal aging.



Tables 2 and 3 report the manufacturer's typical room-temperature mechanical properties and the average hardness values found in this study for Monel K-500 after various heat treatments. For all cases, the mechanical properties determined by Special Metals Corp. are consistent with those given in US Federal Specification QQ-N-286 [12]. The SHT+WQ samples displayed the lowest hardness (~Brinell 130) consistent with absence or low level of  $\gamma'$ , followed by the SHT + AC (Brinell 137), SHT+AC+CW (Brinell 251), and SHT + aged Monel K-500 (Brinell 293). The SHT+AC+CW+aged material exhibited the highest hardness (Brinell 341 or HRC 36.7).

#### ***Hydrogen Trap States in SHT + Aged Monel K-500***

Temperature programmed TDS experiments were performed for SHT + aged Monel K-500. Plotted in Figure 3 is hydrogen desorption rate,  $dC_H/dt$ , as a function of temperature. The hydrogen desorption rate  $dC_H/dt$  at each temperature, and the total absorbed hydrogen concentration, given by the total area defined by a TDS spectrum, increased as the cathodic potential and therefore absolute value of the over-potential for H production increased (Figure 3). The experiment H desorption peak shape in Figure 3 suggests that there are at least two hydrogen trapping states in the SHT + aged Monel K-500, as each curve could be fitted by assuming two overlapping peaks. Each of these peaks increases in height as cathodic overpotential increased. The lower temperature (left) peak was substantially reduced, but the right peak remained after an H precharged sample was baked at 47°C for 5 days, as shown in Figure 4. This suggests that the left peak is associated with diffusible hydrogen<sup>2</sup>.

---

<sup>2</sup>This was further confirmed by a one year bake at room temperature where the right peak remained.

### *Hydrogen Trap State Desorption Energies as a Function of Monel K-500 Heat Treatment*

Hydrogen desorption rate versus temperature data, and the curve fit deconvoluted peaks for SHT + aged Monel K-500, are plotted in Figure 5 where the samples were H-charged for 10 days at 60°C and -1.475 V vs. Hg/HgSO<sub>4</sub> in 0.0214 M Na<sub>2</sub>B<sub>4</sub>O<sub>7</sub>·10H<sub>2</sub>O + 0.1144 M H<sub>3</sub>BO<sub>3</sub> (pH ~8.4). A broad experimental peak was observed with a low temperature shoulder. The peak temperature increases with heating rate as expected for a thermally controlled and activated desorption process [36, 37]. The apparent activation energy for H desorption was 33.3 kJ/mole ±1.1 kJ/mol assuming a single peak, as shown in Figure 5(B). Each broad experimental peak in Figure 5 can be fit with two fitted peaks, as supported by the results shown in Figures 3 and 6, where the samples were H-charged for 10 days at room temperature and -1.20 V vs. SCE in 0.6 M NaCl solution with a pH adjusted to 8.0 with NaOH solution. The desorption activation energies for the left and right peaks were determined by Equation 6 and regression analysis to be 28.2± 1.0 kJ/mole and 35.0±1.1 kJ/mole, respectively, for the borate buffer solution (Figure 5(B)). The 95% confidence intervals is indicated in all cases by the ± data. The desorption activation energies for the left and right peaks were 24.6 ± 2.2 kJ/mol and 38.1±4.9 kJ/mole, respectively, for the NaCl charging solution (Figure 6). Similar behavior was observed for SHT + CW + aged Monel K-500 (Figure 7) where the desorption activation energies for the low temperature and high temperature peaks were 24.3±1.4 kJ/mol and 33.5±4.3 kJ/mol. However, in the SHT + WQ case (Fig. 8), only one narrow peak was resolved in the hydrogen desorption rate versus temperature plot for each hydrogen charging condition examined. This was observed in the borate or chloride solution at 60°C or at room temperature at all heating rates. This was only true, however, when thin foils were rapidly quenched in ice water. The activation energy for hydrogen desorption

from SHT +WQ Monel K-500 was calculated to be  $25.6 \pm 0.5$  kJ/mole, which is statistically similar to the activation energy for the left fitted peak in both the SHT + aged ( $28.2 \pm 1.0$  kJ/mol for borax and  $24.6 \pm 2.2$  kJ/mol for NaCl) and SHT + CW + aged ( $24.3 \pm 1.4$  kJ/mol) cases. In the SHT + AC + CW case (Fig. 9), only one peak was resolved in the hydrogen desorption rate versus temperature plot. The single activation energy for desorption was  $29.8 \pm 2.0$  kJ/mole, resolvably higher and statistically distinct at the 95% confidence level than that measured for the SHT +WQ case ( $25.6 \pm 0.5$  kJ/mol). This difference is apparently attributed to superposition of either the trapping effect of the 1.6 wt% precipitated  $\gamma'$  phase found by XRD, or dislocation-cell structure trapping due to cold work. The activation energies for hydrogen desorption from the fitted, higher temperature peak in the SHT+aged and SHT+CW+aged cases are statistically greater at the 95% confidence limit than that of the single peak in the SHT+WQ case.

#### *Effective Hydrogen Diffusivity and Activation Energy as a function of Monel K-500 Heat Treatment*

Both effective H diffusivity and the activation energy,  $E_m^{app}$ , for H diffusion in Monel K-500 were determined from isothermal TDS measurements and analysis. Isothermal H egress results are plotted in Figure 10 for SHT + aged Monel K-500. From these data,  $D_{eff}$  at each temperature was calculated. The results are plotted in Figure 11a, fit to Equation 2 and compared to literature findings for Monel K-500 heated to 950°C and cooled [17]. There is good agreement. In Figure 11b, the data are reported (as lines) compared to single crystal Ni and 70%Ni-30%Cu. In Table 4, the complete set of comparisons including Ni, Cu and a 70%Ni-30%Cu alloy of an uncertain microstructure are reported. The Monel K-500 diffusivity data are slower than the reported H diffusivities for pure single crystal Ni or Cu, and are about the same as reported for the Ni-Cu

binary alloy. The  $E_m^{app}$  values determined for the various microstructures of Monel K-500 investigated in this study, from  $D_{eff}$  vs.  $1/T$  and Equation 2, were in the range of 28.9~41.2 kJ/mol with a 95% confidence limit of about  $\pm 1$  to  $\pm 4$  kJ/mol. Included in these data are high temperature data and the combination of high temperature and room temperature data discussed below. Compared to literature results, as summarized in Table 4 and shown in Figure 11, there is some uncertainty in the exact values, given the need for heating time correction and limited data points. However, SHT+WQ has a lower  $E_m^{app}$  than SHT + aged Monel K-500 ( $28.9 \pm 1.1$  kJ/mol versus  $38.1 \pm 3.6$  kJ/mol, respectively). The higher activation energy in the aged material compared to the solid solution condition may reflect additional transport barriers due to the H trapping. Such influence of solid solution composition on H transport is evidenced by the drop in  $D_{eff}(T)$  in the Ni-Cu alloy compared with pure copper. The room temperature  $D_{eff}$  depends on the exact activation energy used, but it is clear that  $D_{eff}(25^\circ\text{C})$  reported in Figure 11 and Table 4, as calculated from Equation 2, may be on the order of  $\sim 3 \times 10^{-14}$  m<sup>2</sup>/sec in Monel K-500 which is in very good agreement with previous estimates from fracture surfaces of  $10^{-14}$  m<sup>2</sup>/sec [8, 9] and  $7.6 \times 10^{-15}$  m<sup>2</sup>/sec (at 25°C) from gas phase permeation [17].

#### *Effective Hydrogen Diffusivity for SHT + Aged Monel K-500 through Time-dependent H Saturation*

Figure 12 presents the quantity of absorbed hydrogen, measured by TDS and normalized by the saturated amount measured after 1000 h,  $M_T/M_\infty$  versus hydrogen charging time to the  $1/2$  power suggested by Equation 3 for SHT + aged Monel K-500 given as square symbols. The circles are

for SHT+ WQ Monel K-500.<sup>3</sup> The total hydrogen concentration, for a given room temperature H charging time, was obtained through integration of the  $dC_H/dt$  vs. temperature plots taken from ramped TDS experiments performed at a linear heating rate of 3°C/min. Figure 12 shows that the absorbed hydrogen concentration increases with increasing H-charging time and becomes saturated after nearly 1000 h of H charging. A series of assumed H diffusion coefficients were used with Equation 3 to produce the calculated H uptake curves represented by the set of lines. The curve assuming that  $D_{eff}$  is between  $7.5 \times 10^{-15}$  and  $1.0 \times 10^{-14} \text{ m}^2/\text{s}$  matches the SHT+aged experimental data well, indicating that the room-temperature H diffusion coefficient for SHT + aged Monel K-500 is about  $10^{-14} \text{ m}^2/\text{s}$ . Moreover, using Eq.4 and a half time of 11.4 hrs, a  $D_{eff}$  of  $7.1 \times 10^{-15} \text{ m}^2/\text{sec}$  was found for SHT + aged material. Diffusivity is slightly faster in SHT + WQ Monel K-500. These data are also summarized in Table 4, and are in reasonable agreement with the literature and other measurements in this study.

#### *Diffusible Hydrogen Concentration in Monel K-500 as a Function of Hydrogen Over-potential*

Both diffusible and total H concentration were determined for SHT+aged Monel K-500, exposed at a variety of hydrogen over-potentials, and the results are presented in Figure 13. The  $C_{H,diff}$  were obtained by the Barnacle-cell method [27].  $C_{H,diff}$  was determined using Equation 1 and an assumed  $D_{eff}$  value of  $1.3 \times 10^{-10} \text{ cm}^2/\text{s}$ , or  $5 \times 10^{-11} \text{ cm}^2/\text{s}$ . Figure 13 also shows hydrogen concentration from integration of TDS-measured H desorption for SHT + aged Monel K-500 (Figure 3) taken from: (a) the low temperature peak ( $\square$ ) and (b) the total hydrogen concentration,  $C_{H,total}$ , from both low and high temperature peaks summed (O). In addition  $C_{H,total}$  was

---

<sup>3</sup>Individual thin foils were SHT and WQ in order to produce these data. SHT and WQ of thick samples and a poor quench in warm water could produce the dual TDS peak structure of Figures 3,4 and 7 suggesting residual  $\gamma'$ .

determined independently by the LECO method at 650 °C. In Figure 13, the total hydrogen concentrations obtained for the SHT + aged K-500 based on TDS were calibrated by the LECO method as discussed above so the good agreement is guaranteed. The diffusible hydrogen concentrations determined by the Barnacle-cell method are lower than the low temperature peak TDS results calibrated by LECO, based on the H diffusivity of  $1.3 \times 10^{-10} \text{ cm}^2/\text{s}$  at room temperature. Barnacle cell measurements after charging at -500 mV hydrogen overpotential and baking at 47°C as reported in Figure 4 removed all of the measurable diffusible hydrogen charged. Hence, Barnacle cell and TSD data are consistent with one another suggesting a large portion of left peak is diffusible hydrogen. The reason for this difference between TDS estimated diffusible hydrogen and that found by BC is unclear.

## Discussion

The present results provide new insights regarding H interaction with the Monel K-500 microstructure, as well as an important foundation for understanding and modeling HEAC in this alloy class.

### *Diffusible H Concentration*

The diffusible hydrogen concentration represents mobile H at a specific temperature, and includes the sum of hydrogen in lattice interstitial sites and lattice hydrogen interchanging in equilibrium with low energy trap sites activated by sufficient thermal energy (e.g.,  $E_B \sim kT$ ) to be practically indistinguishable from lattice sites. This interpretation is often focused on H which is mobile at ambient temperature. These traps likely include copper solute in the nickel solid solution, dislocations, twin boundaries and low energy grain boundaries [18, 38]. Nickel and



copper have similar electronegativity and atomic size, and are unlikely to function as strong H traps when mixed in solid solution. Never-the-less, some solute trapping of H is suggested by the 10-fold lower value of  $D_{\text{eff}}$  measured for SHT+WQ Monel K-500 compared to pure Cu (Table 4). Grain boundaries and dislocations likely trap hydrogen as reported elsewhere for nickel [13], but have low site densities on the order of  $1-10 \times 10^{17}$  sites/cm<sup>3</sup> except in extremely fine grain sized materials. This expectation is evidenced by the observation of a single desorption peak in ramped TDS of SHT + WQ Monel K-500, and a relatively low hydrogen desorption activation energy of 25.6 kJ/mol, obtained for SHT + WQ Monel K-500 (Figure 8) which was essentially single phase. Except for Lomer-Cottrell dislocation locks, the H-dislocation trap binding energy may be 10 kJ/mol or less and have a site density on the order of  $10^{-18}$  sites/cm<sup>3</sup> [13]. It is uncertain whether this trap state could be resolved given the intermediate site density, low binding energy and high desorption energy. Twin boundaries (Figure 1) have 3% of the energy of grain boundaries in Ni-Cu alloys and are therefore unlikely trap sites [13]. A low site density, modest trap binding energy, and large  $E_m^{\text{app}}$  all obscure observation of these trap sites by TDS. This does not mean that they are not present, but they are not directly assessed by TDS. Both diffusible concentration and total H concentrations are increased by stronger-reversible trapping due to coherent precipitates such as metal carbides in steels [19], and to an extent,  $\gamma'$  in Ni superalloys. As such trap strength increases, reversible trapping is shifted to temperatures above ambient. The diffusible hydrogen content for SHT + aged Monel K-500 is illustrated in Figure 4 where baking at 47°C removes mobile or diffusible hydrogen with a thermal desorption energy in the range of 24.6-28.2 kJ/mol. Particularly, note that this outgassing treatment has essentially eliminated the low temperature shoulder which is otherwise present as part of the total peak for the as-charged condition (Figure 4). This baking

also eliminated diffusible hydrogen, as measured by the Barnacle Cell method applied at 23°C. The low hydrogen partial pressure associated with heating in air is nearly equal to the low H fugacity associated with electrochemical extraction.  $C_{H,diff}$  is higher in aged Monel K-500 compared to aged ultra-high strength steels due to the greater hydrogen solubility of H in the face-centered cubic (*fcc*) nickel-based alloy compared to bcc high strength steels even with a high trap density [22]. It is well known that hydrogen solubility is greater in Ni than Fe [39].

$C_{H,diff}$  and  $C_{H,tot}$  are each a strong function of hydrogen over-potential (Figure 13).  $C_{H,diff}$  increases with the hydrogen over-potential applied to materials with a high density of low energy traps such as in ultra-high strength trap rich steels compared to iron and low alloy high strength steels [22]. This is not necessarily the case in UNS N05500 where SHT+WQ, SHT+AC+CW, SHT+CW+aged and SHT+aged materials all had comparable  $C_{H,diff}$  values apparently dominated by lattice hydrogen and weak traps that are independent of heat treatment. The total hydrogen concentration in aged precipitate-bearing Monel K-500 is associated with stronger trapping in addition to more diffusible hydrogen, as supported by the results in Figures 3~7 and 13. The TDS data indicate a higher energy trap state seen as the high temperature peak in Figures 3~7. Moreover, trapping is indicated in Figure 5 by a higher apparent activation energy for desorption, and in Figure 13 by a  $C_{H,tot}$  value that is greater than  $C_{H,diff}$  in aged material, as determined by two methods (LECO and TDS) ways. Secondary phases, especially the part of  $\gamma'$   $Ni_3(Al,X)$  precipitates which are incoherent, and carbides are likely-strong trap sites, as seen in other alloys[18, 40]. The  $\gamma'$  phase exists in the SHT + age and SHT + AC conditions, but not in the thin section SHT/WQ condition of Monel K-500.

### ***H-Trap Interaction Energy***

It is reasonable to assume that the energy for H desorption equals the sum of trap binding energy and H-migration energy for perfect lattice diffusion; that is  $E_d = E_m + E_b$ , where  $E_m$  represents the near perfect lattice interstitial migration energy and  $E_b$  is the H-trap binding energy for a given state. The two peaks appearing in both the SHT+aged and SHT+AC+CW+aged cases correspond to two hydrogen states, the higher temperature peak to reversibly-to-irreversibly trapped hydrogen and the lower temperature (left) peak to lattice diffusible and possibly some other weakly trapped hydrogen (Figure 3, 5-7). Both experimental and analytical procedures to determine  $E_m^{app}$  for trap-free H diffusion in Monel K-500 suggest that it is approximately equal to or less than the desorption energy  $E_d$  determined for the SHT+WQ case,  $25.6 \pm 0.5$  kJ/mol (in Figure 8). This conclusion is supported by TDS data in which all the desorption activation energies for the lower temperature peak shown in Figures 5(A) ( $28.2 \pm 1.0$  kJ/mol), 6(A) ( $24.6 \pm 2.2$  kJ/mol) and 7(A) ( $24.3 \pm 1.4$  kJ/mol) are statistically equal to that value at the 95% confidence level (with the exception of the result for the borax solution (Figure 5(A))). The suggestion is that the lower temperature peak in all TDS studies represents perfect lattice migration and egress with a desorption energy of  $24.3 \pm 1.4 \sim 28.2 \pm 1.0$  kJ/mole.

The higher temperature peak is suggested to be a higher energy-stronger trap state with a desorption energy of  $33.5 \pm 4.3 \sim 38.1 \pm 4.9$  kJ/mole. It was confirmed that the low temperature peak was absent, but the higher temperature peak remained after the sample was baked at  $47^\circ\text{C}$  for 5 days which was interpreted to reflect the removal of lattice and weakly trapped hydrogen.

Assuming that  $E_d = E_m + E_b$ , literature reports of  $E_m^{app}$  for aged Monel K-500 (Table 4) may not have taken this fact into consideration [17]. As such,  $E_m^{app}$  from permeation experiments in non-precharged material likely reflects both perfect lattice migration and reversible trapping [41].

This is why  $D_{\text{eff}}$  from permeation or uptake in uncharged material is often lower than determined from egress of H from precharged material.

In both the SHT + aged and SHT + CW + aged cases, the hydrogen trapping sites were assumed to be mainly located at the interface between the matrix and  $\text{Ni}_3\text{Al}$  precipitates. For the SHT + AC + CW case, the primary trap sites may also have been  $\text{Ni}_3\text{Al}$  precipitates, but only a small amount of precipitate formed on air cooling, as indicated in Figure 2, and the trapped H concentration was presumably smaller. Since the  $E_d$  for the higher temperature peak is greater than  $E_m$ , the apparent trap binding energy can be determined for aged Monel K-500 from thermal desorption data, as conducted routinely in the case of bcc steels [42, 43]. With  $E_m$  of  $25.6 \pm 0.5$  kJ/mol  $E_d$  for the low temperature peak in  $\gamma'$ -free SHT + WQ, and  $E_d$  of  $35.8 \pm 4.6$  kJ/mole from the average of the two high temperature peak measurements in the artificially aged Monel K-500 microstructures which contain  $\gamma'$ ,  $E_d = E_m + E_b$  suggests that the H-trap binding energy for this single feature is, on average, 10.2 kJ/mol with an uncertainty of  $\pm 4.6$  kJ/mol at the 95% confidence level. Thus,  $E_b$  is considerably smaller than the perfect lattice migration energy,  $E_m$ , in Monel K-500. This is quite reasonable given the low misfit strain between  $\gamma'$   $\text{Ni}_3\text{Al}$  and the  $\gamma$  phase with a reported misfit less than about 0.003 based on lattice parameters for the  $\gamma$  phase of 0.3565 versus 0.3567 for  $\gamma'$  phase [2] in this alloy. This value of  $E_b$  agrees well with H-trap binding energies reported for other coherent precipitates in iron-based alloys such as  $\text{M}_2\text{C}$  carbides in steel [19]; such precipitates were demonstrated to be strong-reversible traps of H which lower  $D_{\text{eff}}$  compared to lattice migration. The TiC precipitate has greater difference in lattice parameters and may be an incoherent trap site which exhibits a very high  $E_b$  on the order of 90 kJ/mol [38, 44, 45]. In Monel K-500 TiC is present as a large inclusion (Figure 1B), but in a very low volume fraction which precludes this phase from acting as a dominant trap of H.

Diffusion analysis [19] can also be utilized to estimate trap density and binding energy using the Oriani expression modified to account for two dominant trap states that influence  $D_{\text{eff}}$ . This trap sensitive H diffusivity is given as follows based on the assumption that H mobility is affected by two trap states, coherent  $\gamma'$  precipitates and dislocations [46, 47].

$$D_{\text{eff}}(T) = \frac{D_L(T)}{1 + \frac{N_{\text{Dislocation}}}{N_L} \exp\left(\frac{E_{b-\text{Dislocation}}}{RT}\right) + \frac{N_{\text{Ni}_3\text{Al}}}{N_L} \exp\left(\frac{E_{b-\text{Ni}_3\text{Al}}}{RT}\right)} \quad (7)$$

where  $D_L$  is the diffusivity of H through perfect lattice sites ( $8.4 \times 10^{-14} \text{ m}^2/\text{sec}$  at  $T = 300 \text{ K}$  as indicated for pure single crystal Ni or as indicated in Table 4),  $N_L$  is the number of octahedral lattice sites per unit volume ( $N_L = 8.9 \times 10^{28}$  interstitial sites per  $\text{m}^3$  in fcc Ni).  $N_{\text{Dislocation}}$  is the number of dislocation trap sites per volume which may reach  $10^{25}$  trap sites/ $\text{m}^3$  (dislocation density of  $10^{15} \text{ m}^{-2} \times 10^{10}$  hydrogen trap sites per m of dislocation line).  $N_{\text{Ni}_3\text{Al}}$  is the number of coherent  $\gamma'$  trap sites,  $E_{b-i}$  are the binding energies for the dislocation and  $\gamma'$  traps, and  $R$  and  $T$  have the usual meanings. TiC is excluded from Eq. (7) because  $N_{\text{TiC}}/N_L$  is very low. This trap analysis [19] yields an apparent binding energy of  $E_B = 9$  to  $16 \text{ kJ/mole}$  for  $\text{Ni}_3\text{Al}$  trap sites when the ratio  $N_{\text{Ni}_3\text{Al}}/N_L$  is assumed to be 0.05 to 0.34. (When this ratio is taken to be 0.05,  $N_{\text{Ni}_3\text{Al}}$  is  $4.4 \times 10^{27}$  sites/ $\text{m}^3$ .) This range of site ratios is possible in the case of a coherent precipitate that is present at 6-7% by volume, is in the form of nanometer scale coherent spheres and traps at the matrix particle interface [2]. Under these conditions,  $E_m^{\text{app}}$  for SHT + aged Monel K-500 should be in the range of 34~41 kJ/mol if the activation energy for the observed low temperature peak representing perfect lattice transport is taken as 25 kJ/mol. This is exactly as seen when low temperature saturation data are taken into account to determine  $D_{\text{eff}}(T)$  for aged Monel K-500

(Figure 11 and 12, Table 4). This effect accounts for the historically high apparent activation energy reported in Table 4.<sup>4</sup> In first break through and lag time determinations of  $D_{\text{eff}}$  from permeation experiments (Table 4), the additional transport impedance caused by such traps cannot be readily separated from lattice transport and the apparent diffusion rate produces a high  $E_m^{\text{app}}$  as reported in Table 4.

The assignment of the H-trap state dominating H mobility to  $\text{Ni}_3\text{Al}$  is justified. Such a high  $N_{\text{trap}}/N_L$  value cannot be obtained if hydrogen is trapped by other low density sites such as incoherent interfaces associated with  $\text{TiC}$  or  $(\text{Mn,Mg})\text{S}$  inclusions. Moreover, these latter phases are likely unchanged by aging. In contrast, aging formed  $\gamma'$  which produced an observable effect on trapping. This leaves the  $\text{Ni}_3\text{Al}$  phases as the likely dominant intermediate strength trap in this alloy. This is consistent with previous results for a  $\gamma'$  strengthened Ni-Cr-Fe-Al-Ti alloy (X-750) where  $\text{Ni}_3(\text{Al,Ti})$  was found to be an intermediate strength trap [18] and carbide, dislocation and grain boundary trapping were all discounted. In fact, a trap binding energy of 19.2 kJ/mol was reported for  $\gamma'$  in alloy 903 with a different misfit strain of 0.0075 [13].

High angle grain boundaries also likely trap hydrogen as reported elsewhere for nickel [13], but have extremely low site densities except in extremely fine grain sized materials. The lack of a high temperature TDS peak for grain boundaries suggests: (a) a low site density, (b) modest trap binding energy confounded by the high  $E_d$  value in nickel base materials and (c) perhaps TDS detection limit/background issues. If  $E_b$  for grain boundary sites exceeds 10 kJ/mol, as is likely,

---

<sup>4</sup>Wimmer's data [48] suggest 45.7 kJ/mol as the  $E_m$  for a perfect Ni lattice, but this calculation neglects the 70%Ni and 30% Cu solid solution composition of this alloy with the associated change in lattice parameter.  $E_m^{\text{app}}$  is lower in Cu as well as unaged Ni-Cu alloys in Table 4 suggesting that perfect lattice H migration energy may decrease upon alloying with Cu.

then weakly trapped hydrogen at  $\gamma'$  can repartition to grain boundaries under tensile stress where hydrogen is retrapped to trigger intergranular fracture [13, 18, 49]

### Conclusions

Hydrogen diffusivity, trapping and binding energy were determined for heat treatments which produced several variations in the microstructure of Ni-based Alloy Monel K-500 (UNS N05500). Diffusible hydrogen concentration ranged from 0 to 60 wppm H as the cathodic overpotential for H production increased to as low as -0.3V (-1.014 V vs. SCE) in NaCl + NaOH electrolyte. Room temperature H diffusivity ranged from 0.9 to  $3.9 \times 10^{-14}$  m<sup>2</sup>/sec for solution heat treated, SHT + aged, SHT + AC + CW, and SHT + AC + CW + aged Monel K-500. The apparent activation energy for H diffusion was in the range of  $29.1 \pm 1.1$  to  $41.2 \pm 1.7$  kJ/mol, depending on metallurgical condition. The higher activation energy reflects reversible trapping at Ni<sub>3</sub>Al precipitates as well as perfect lattice transport of H. The lower values reflect perfect fcc-lattice transport. Hydrogen trapping at a metallurgical site was evident in the SHT + aged and SHT + AC + CW as well as SHT + AC + CW + aged microstructures compared to the precipitate free SHT + WQ Monel K-500. This was indicated by desorption rate vs. ramped temperature spectra from TDS which contained two peaks, corresponding to hydrogen states for lattice hydrogen and trapped hydrogen. The SHT + AC microstructure indicated  $\gamma'$  based on XRD and trapping by TDS. Both thermal desorption experiments and theoretical Oriani trap state analyses suggest that trap binding energies are less than the activation energy for H migration ( $25.6 \pm 0.5$  kJ/mol) in this nickel-based alloy. This intermediate strength trap binding energy was estimated to be  $10.2 \pm 4.6$  kJ/mole for  $\gamma'$  Ni<sub>3</sub>Al in SHT + aged and in SHT + AC + CW + aged Monel K-500.



## Acknowledgements

We gratefully acknowledge support from ONR Grant N00014-06-1-0366 and N00014-10-1-0552 under the direction of Dr. Airan Perez. Special Metals Corporation is also acknowledged for supply of Monel K-500 rod as well as further discussions.

## References

- [1] *Special Metals product data sheet on Monel Alloy K-500 (UNS N05500)*, [www.specialmetals.com](http://www.specialmetals.com).
- [2] Dey GK, Mukhopadhyay P. *Mater. Sci. Eng.* 1986; 84: 177.
- [3] Hagel WC, Beattie JHJ. *Trans. Inst. Min. Metall. Eng.* 1959; 215: 967.
- [4] Ardell AJ, Nicholson RB. *Acta Metall.* 1966; 14: 1295.
- [5] Murr LE, Smith PJ, Gilmore CM. *Philos. Mag.* 1968; 17: 89.
- [6] Copson HR, Cheng CF. *Corrosion* 1956; 12: 647.
- [7] Efird KD. *Mater. Performance* 1985; 24: 37.
- [8] Harris JA, Stephens CD, Scarberry R. *Corrosion* 1972; 28: 57.
- [9] Scully JR, Vassilaros MG. *The Hydrogen Embrittlement Susceptibility of Monel Alloy K-500*. in *DTNSRDC SME 84-69*. 1984.
- [10] Price C, Fredell R. *Metall. Mater. Trans. A* 1986; 17: 889.
- [11] Wolfe LH, Joosten MW. *SPE Production Engineering*, 1988; p. 382-386.
- [12] *QQ-N-286G Federal Specification for Nickel-Copper-Aluminum Alloy, Wrought (UNS N05500) provided by HIS*. 07 December 2000.
- [13] Moody NR, Robinson SL, Myers SM, Greulich FA. *Acta Metall.* 1989; 37: 281.
- [14] Gangloff RP. *Hydrogen Assisted Cracking of High Strength Alloys*, in *Comprehensive Structural Integrity*, New York: Elsevier Science, Scott JPaP (Ed.). New York: Elsevier Science. 2003; p. 31-101.
- [15] Raymond L. *LRA report # CTC"071024*. 2008.
- [16] Sakamoto Y, Takao K. *J. Jpn. Inst. Met.* 1982; 46: 285.
- [17] Mitchell DJ, Edge EM. *J. Appl. Phys.* 1985; 57: 5226.
- [18] Turnbull A, Ballinger R, Hwang I, Morra M, Psaila-Dombrowski M, Gates R. *Metall. Mater. Trans. A* 1992; 23: 3231.
- [19] Li D, Gangloff R, Scully J. *Metall. Mater. Trans. A* 2004; 35: 849.
- [20] Kehler BA, Scully JR. *Corrosion* 2008; 64: 465.

- [21] Dogan H, Li D, Scully JR. *Corrosion* 2007; 63: 689.
- [22] Thomas R, Scully J, Gangloff R. *Metall. Mater. Trans. A* 2003; 34: 327.
- [23] Gangloff RP. *Diffusion Control of Hydrogen Environment Embrittlement in High Strength Alloys*, in *Hydrogen Effects on Material Behavior and Corrosion Deformation Interactions*, Moody NR, Thompson AW, Ricker RE, Was GS, Jones RH. (Eds.). The Minerals, Metals & Materials Society: Warrendale, PA. 2003; p. 477-497.
- [24] Wang GL, Wu CW, Zhang Maicang, Dong JX, Xie XS, Radavich J, Lindsley BA, Shen G. *Mater. Sci. Eng. A* 2003; 358: 71.
- [25] Smith S, Scully J. *Metall. Mater. Trans. A* 2000; 31: 179.
- [26] Smith SW. in *Materials Science and Engineering*. The University of Virginia: Charlottesville, 1995.
- [27] DeLuccia JJ, Berman DA. *Electrochemical Corrosion Testing in ASTM STP 727*. 1981. p. 256-273.
- [28] ASTM, *Standard Test Method for Electrochemical Measurement of Diffusible Hydrogen in Steels (Barnacle Electrode)*. ASTM Intl.; 2005.
- [29] Iacoviello F, Galland J, Habashi M. *Corros. Sci.* 1998; 40: 1281.
- [30] Geiger GH, Poirier DR. *Transport Phenomena in Metallurgy*. Addison-Wesley Series in Metallurgy and Materials. Addison-Wesley Publishing Company; 1973.
- [31] Crank J. *The Mathematics of Diffusion*. 2nd ed. Oxford: Clarendon Press; 1975.
- [32] Woodruff DP, Delchar TA. *Modern Techniques of Surface Science*. Cambridge, UK: Cambridge University Press; 1986.
- [33] Lee Y, Lee JL, Choo WY. *Current Solutions to Hydrogen Problems in Steels*. Metals Park, OH: ASM, 1982.
- [34] Kissinger HE. *Anal. Chem.* 1957; 29: 1702.
- [35] Johnson HH, Quick N, Kumnick AJ. *Scripta Metall.* 1979; 13: 67.
- [36] Ono K, Meshii M. *Acta Metall. Mater.* 1992; 40: 1357.
- [37] Turnbull A, Hutchings RB. *Mater. Sci. Eng. A* 1994; 177: 161.
- [38] Hirth J. *Metall. Mater. Trans. A* 1980; 11: 861.
- [39] Fowler RH, Smithells CJ. *Proceedings of the Royal Society of London. Series A - Mathematical and Physical Sciences* 1937; 160: 37.
- [40] Angelo JE, Moody NR, Baskes MI, *Modell. Simul. Mater. Sci. Eng.* 1995; 3: 289.
- [41] Sakamoto Y, Shimizu O, Hirayama K, Baba K. *J. Phys. Chem. Solids* 1988; 49: 897.
- [42] Völkl J, Alefeld G. in *Hydrogen in Metals I – Basic Properties*, Alefeld G, Völkl J (Eds.). New York: Springer-Verlag; 1978; p. 326-329.

- [43] Fisher DJ. *Hydrogen Diffusion in Metals, A 30-Year Retrospective*. Zuerich-Uetikon, Switzerland: SCITEC Publications Ltd., 1999
- [44] Pressouyre G, Bernstein I. *Metall. Mater. Trans. A* 1978; 9: 1571.
- [45] Wei FG, Tsuzaki K. *Hydrogen Trapping in Martensitic Steels*, in *Gaseous Hydrogen Embrittlement of Materials in Energy Technologies*, Gangloff RP, Somerday BP (Eds.). Cambridge, UK: Woodhead Publishing Ltd.; 2012; p. 493-525
- [46] Oriani RA. *Acta Metall.* 1970; 18: 147.
- [47] Scully J, Van Den Avyle J, Cieslak M, Romig A, Hills C. *Metall. Mater. Trans. A* 1991; 22: 2429.
- [48] Wimmer E, Wolf W, Sticht J, Saxe P, Geller CB, Najafabadi R, Young GA. *Phys. Rev. B* 2008; 77: 134305.
- [49] Pound BG. *Acta Metall. Mater.* 1990; 38: 2373.
- [50] Ahila S, Reynders B, Grabke HJ. *Corros. Sci.* 1996; 38: 1991.
- [51] Guthrie JW, Beavis LC, Begeal DR, Perkins WG. *J. Nucl. Mater.* 1974; 53: 313.
- [52] Katz L, Guinan M, Borg RJ. *Phys. Rev. B* 1971; 4: 330.
- [53] Hagi H. *J. Jpn. Inst. Met.* 1983; 47: 1029.

Table 1. Compositions (wt%) of Monel Alloy K-500 (UNS N05500) .

Elements	Ni %	Cu %	Al %	Fe %	Mn %	Si %	Ti %	C %	Co %	Cr %	Mo %	V %	Ta %	S ppm	P ppm	Sn ppm	Pb ppm	B ppm
SHT+AC+CW;SHT+AC+CW+aged*	64.21	30.41	3.00	0.71	0.76	0.074	0.55	0.15	0.014	0.05	0.01	0.006	0.0002	35	134	26	2	42
SHT + aged; SHT + W.Q.; SHT+A.C.*	63.69	30.20	2.69	1.66	0.58	0.14	0.61	0.169	0.007	0.11	0.061	0.008	0.016	<20	70	10	50	47
SHT + aged; SHT + W.Q.; SHT+A.C.**	64.26	30.35	2.97	0.84	0.74	0.11	0.56	0.16						<10	90	0.7	7.7	
QQ-N-286G Federal Specification [12]	>63.0	27.0; 33.0	2.3- 3.15	<2.0	<1.5	<0.5	0.35- 0.85	<0.18	<0.25	-	-	-	-	<60	<200	<60	<60	-

Note: \* measured by QUANT Corp on Special Metals Materials; \*\* provided by Special Metals Corp.

Table 2.Manufacturer reported nominal room-temperature mechanical properties of Monel Alloy K-500 (UNS N05500) [50]

Metallurgical Condition	$\sigma_{UTS}$ (MPa)	$\sigma_{YS}$ (MPa)	Elongation,%	Reduction of Area, %
SHT + aged <sup>a</sup>	1146	783	25.6	48
SHT+cold-worked+aged <sup>b</sup>	1276	1034	14	35
SHT + water-quenched <sup>c</sup>	627	248	51	73
SHT + air-cooled <sup>d</sup>	641	262	49	72
SHT + air-cooled+cold-worked <sup>d</sup>	827	745	18	52
QQ-N-286G U.S. Federal Specification[12]	> 896	> 621	> 20	-

Note: Prior SHT at <sup>a</sup>: 982°C; <sup>b</sup>: 1038°C; <sup>c</sup>: 1066°C and <sup>d</sup>: 1038°C. Subsequent aging at <sup>a</sup>: heating to 593°C for 16h, and at 538°C for 6h, then at 482°C for 8h and finally air-cooling; <sup>b</sup>: heating at 534°C for 10h followed by cooling to 481°C at 15°F/h and then holding at 481°C for 9.5h and finally air-cooling.

Table 3.Experimental determined hardness values of Monel Alloy K-500 (UNS N05500) found in this study

Metallurgical Condition	HRB	HRC	Brinell
SHT + aged	-	31.2±0.6	287±5.4
SHT + AC + CW + aged	-	36.7±0.4	341±3.6
SHT + WQ	72.3±0.4	-	130±0.6
SHT+AC	75.9±0.4	-	137±0.8
SHT+AC + CW	-	25.5±1.3	251.3±12.6
QQ-N-286G Federal Specification [12]or Special Metals Product Data Sheet Monel alloy K-500[50]	-	23*	245*

Note: \*: hot-finished condition, not aged

Table 4. Effective Diffusivity, Activation Energy and Analysis Method for hydrogen diffusion in Cu, Ni, Ni-Cu alloys and Monel Alloy K-500 (UNS N05500).  $\pm$  data indicates the 95% confidence interval.

Materials	Conditions	$E_m^{app}$ (kJ/mol)	$D_{o-eff}$ ( $m^2/s$ )	$D_{eff}(T=25^\circ C)$ ( $m^2/s$ )	Method/Reference
Cu 1	T=292~339K, $i=10A/m^2$ , annealed (also cold worked which exhibited lower D and higher $E_m^{eff}$ )	36.82	$3.69 \times 10^{-7}$	$1.29 \times 10^{-13}$	Galvanostatic charging conditions, electrochemical permeation [16]
Cu 2	200~300 °C	38.41	$1.06 \times 10^{-6}$	$1.95 \times 10^{-13}$	Permeation time-lag methods [51]
SC Ni	Single crystal, 99.999%, 670~1270 K	39.5	$7.04 \times 10^{-7}$	$8.41 \times 10^{-14}$	Out-gassing rate-measurements of specimens which were initially saturated [52]
Ni	Perfect lattice fcc interstitial sites	45.72	$3.84 \times 10^{-6}$	$3.74 \times 10^{-14}$	Computation using transition state theory [48]
Ni-Cu 1	T=260~1000K, E max at 70at% Cu	41.4	$9.20 \times 10^{-7}$	$5.09 \times 10^{-14}$	Electrochemical and gas permeation [53]
Ni-Cu 2	Annealed, 30at% Cu (H diffusivity decreased as %Cu increased), T=296~333K	40.92	$4.86 \times 10^{-7}$	$3.26 \times 10^{-14}$	Electrochemical permeation [41]
Monel K-500	T=200~400°C, HT: SHT 1°C/s to 950°C in vacuum, hold 950°C for 50s, cool radiatively	45.35	$6.76 \times 10^{-7}$	$7.64 \times 10^{-15}$	Gas-phase permeation breakthrough [17]
SHT/Aged K-500	Isothermal heating at 125, 150, 175, 200, 225, 250 and 275°C, in ultra-high vacuum, TDS analysis.	38.1 $\pm$ 3.6	$6.9 \times 10^{-8}$	$1.3 \times 10^{-14}$	Isothermal TDS <i>this work</i>
SHT/WQ K-500		28.9 $\pm$ 1.1	$4.9 \times 10^{-9}$	$3.9 \times 10^{-14}$	
SHT/AC/CW K-500		33.0 $\pm$ 1.8	$1.8 \times 10^{-8}$	$2.7 \times 10^{-14}$	
SHT/CW/Aged K-500		29.6 $\pm$ 2.4	$5.6 \times 10^{-9}$	$3.3 \times 10^{-14}$	
SHT/Aged K-500	Ramped heating at 3°C/min from 25°C to 550°C	-	-	$9.0 \times 10^{-15}$	Saturation curve analysis using ramped TDS, <i>this work</i>
SHT/WQ K-500		-	-	$1.3 \times 10^{-14}$	
SHT/Aged K-500	Isothermal tests over a range of temperatures and room temperature saturation curve analysis by ramped heating	41.2 $\pm$ 1.7	$1.5 \times 10^{-7}$	$9.1 \times 10^{-15}$	mix of isothermal TDS & saturation data at room temperature, <i>this work</i>
SHT/WQ K-500		35.9 $\pm$ 1.6	$2.8 \times 10^{-8}$	$1.5 \times 10^{-14}$	

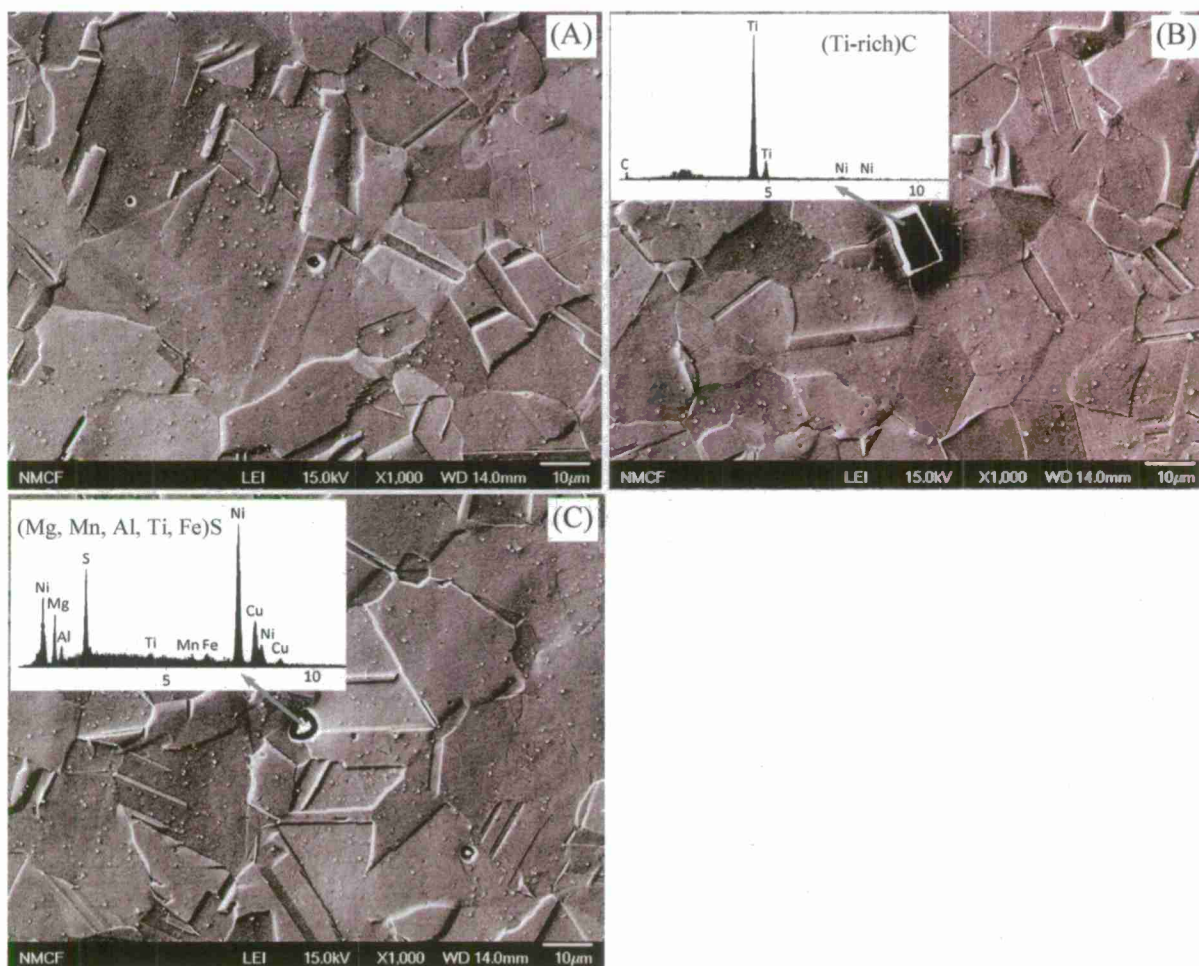


Figure 1. SEM images for SHT + aged Monel K-500, (A) typical microstructure, (B) (Ti-rich)C and (C) inclusion (Mg, Mn, Al, Ti, Fe)S determined by EDX analysis. Samples were etched by Glyceria (30 mL glycerol + 20 mL 12 N HCl + 10 mL 15 N HNO<sub>3</sub>) for 5 to 20 minutes.



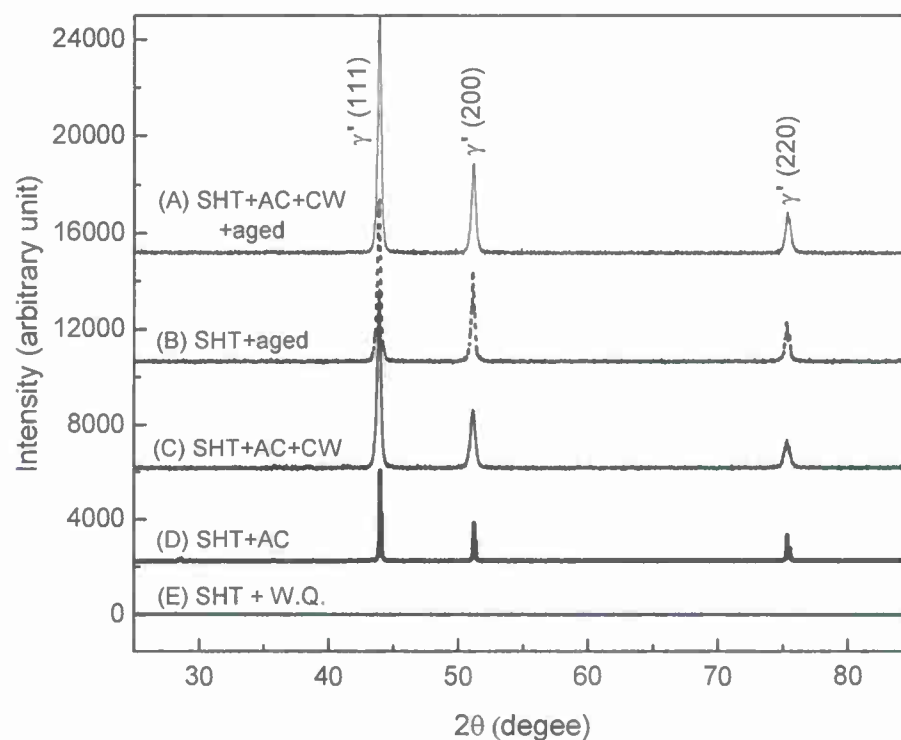


Figure 2. XRD patterns of extracted precipitates from Monel K-500 in: (A) SHT at 1038°C + CW + aged, (B) SHT at 982°C + aged, (C) SHT at 1038°C + AC + CW and (D) SHT at 1038°C + AC cases after removal of the  $\gamma$  phase matrix and (E) SHT at 1066°C + WQ (little residue powder phase collected). Note: (A), (B), (C) and (D) pattern origins are at 15000, 10500, 6000 and 2000 units, respectively.



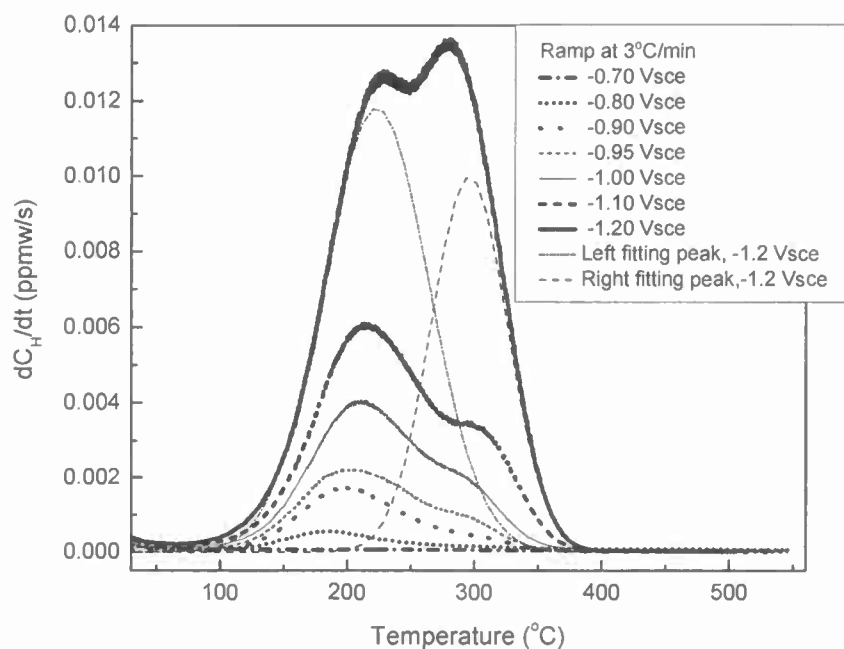


Figure 3. H desorption rate ( $dC_H/dt$ ) as a function of temperature from the ramped TDS experiment with SHT + aged Monel K-500 at the ramp rate of  $3^{\circ}\text{C}/\text{min}$ . Specimens were H-charged for 10 days at room temperature and the various potentials in 0.6 M NaCl solution with pH adjusted to 8.0 with NaOH.

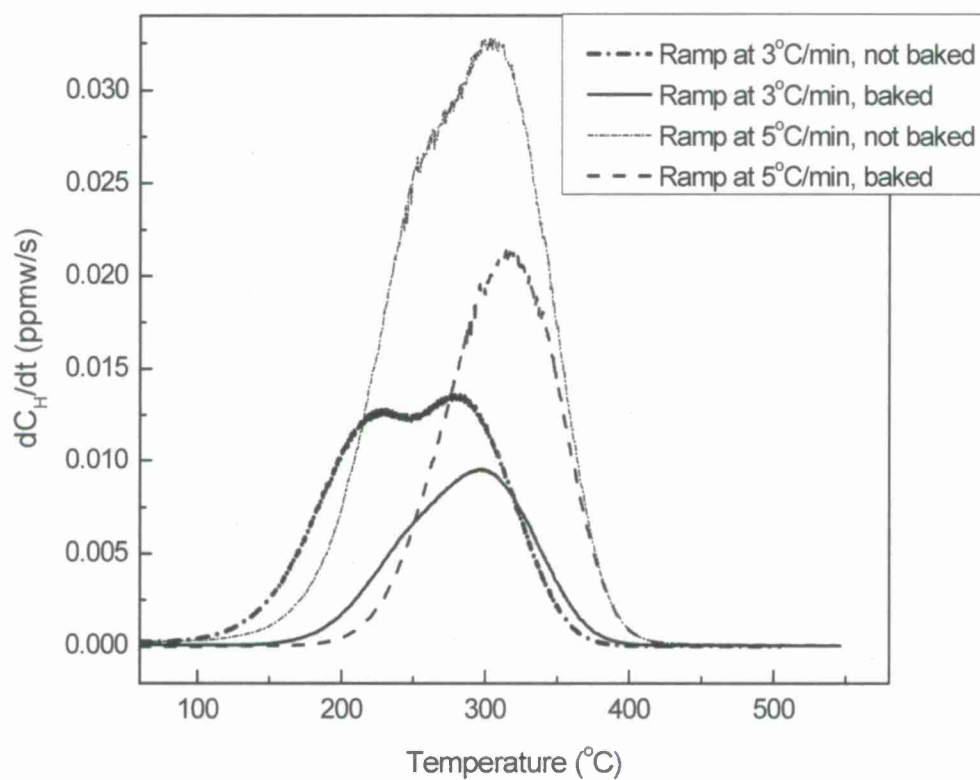


Figure 4. H desorption rate ( $dC_H/dt$ ) as a function of temperature from TDS experiments at various ramp rates for SHT + aged Monel K-500. Specimens were H-charged for 10 days at room temperature at -1.20 V vs. SCE in 0.6 M NaCl solution with pH adjusted to 8.0 with NaOH solution and then either tested immediately or after baking at 47°C for 5 days in air.

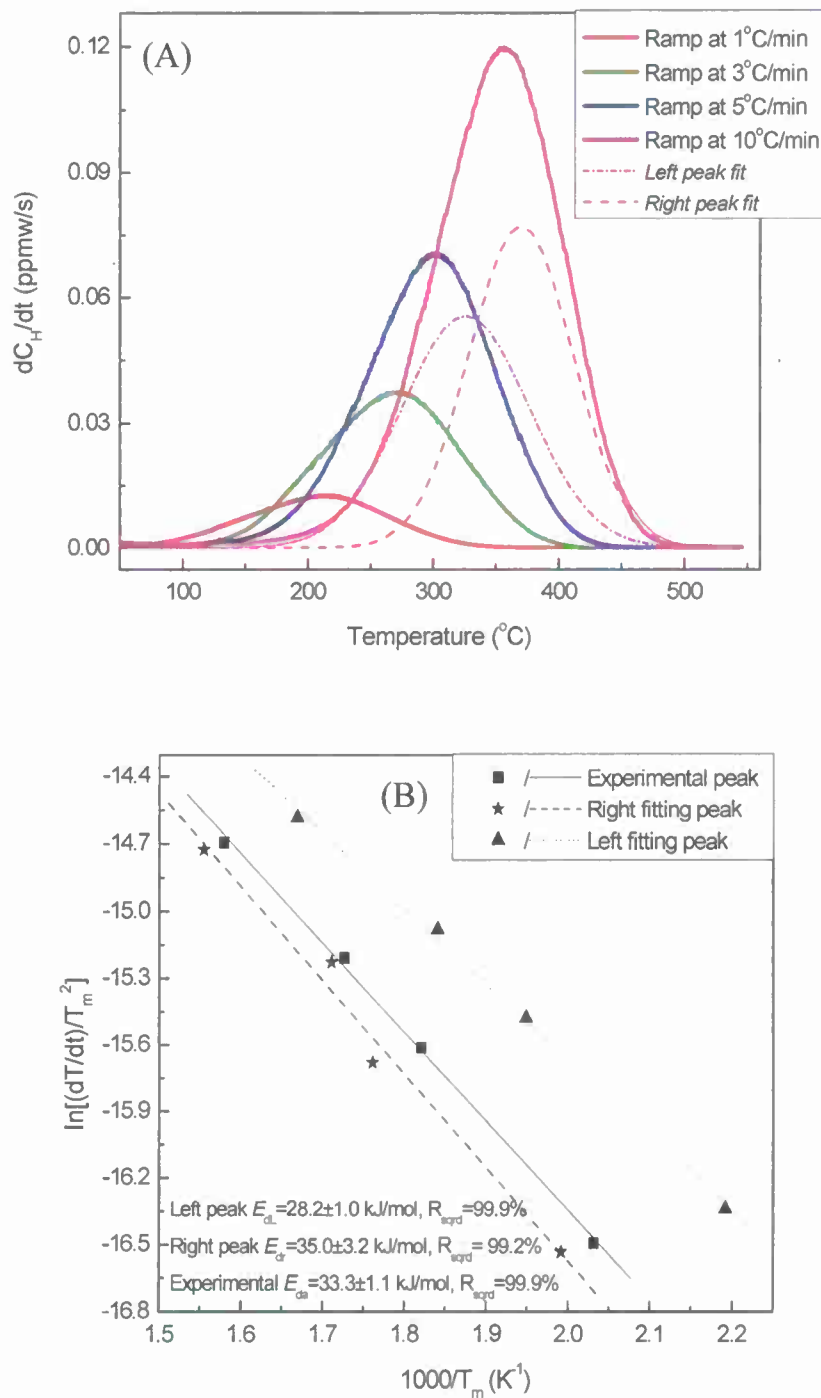


Figure 5. TDS experimental results at various ramp rates for SHT + aged Monel K-500: (A) H desorption rate ( $dC_H/dt$ ) as a function of temperature and the curve fit deconvoluted peaks, (B) determination of the apparent activation energy  $E_{da}$  for H desorption, the left fit peak activation energy  $E_{dL}$  and the right fit peak activation energy  $E_{dR}$  from the TDS results in (A) and their 95% confidence intervals. Specimens were H-charged for 10 days at 60 $^{\circ}\text{C}$  and -1.475 V vs. Hg/HgSO<sub>4</sub> in 0.0214 M Na<sub>2</sub>B<sub>4</sub>O<sub>7</sub>·10H<sub>2</sub>O + 0.1144 M H<sub>3</sub>BO<sub>3</sub> (pH ~8.4).

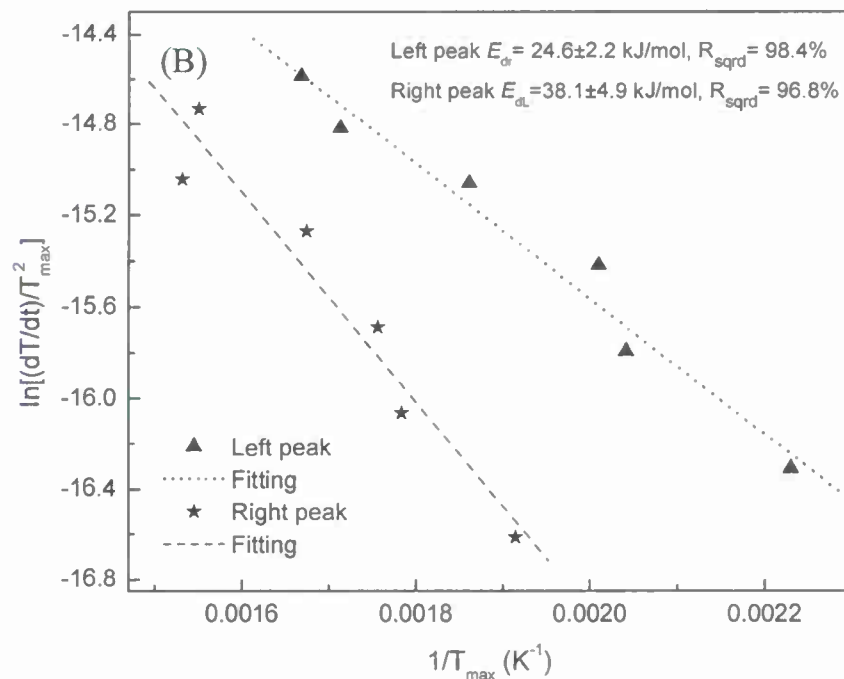
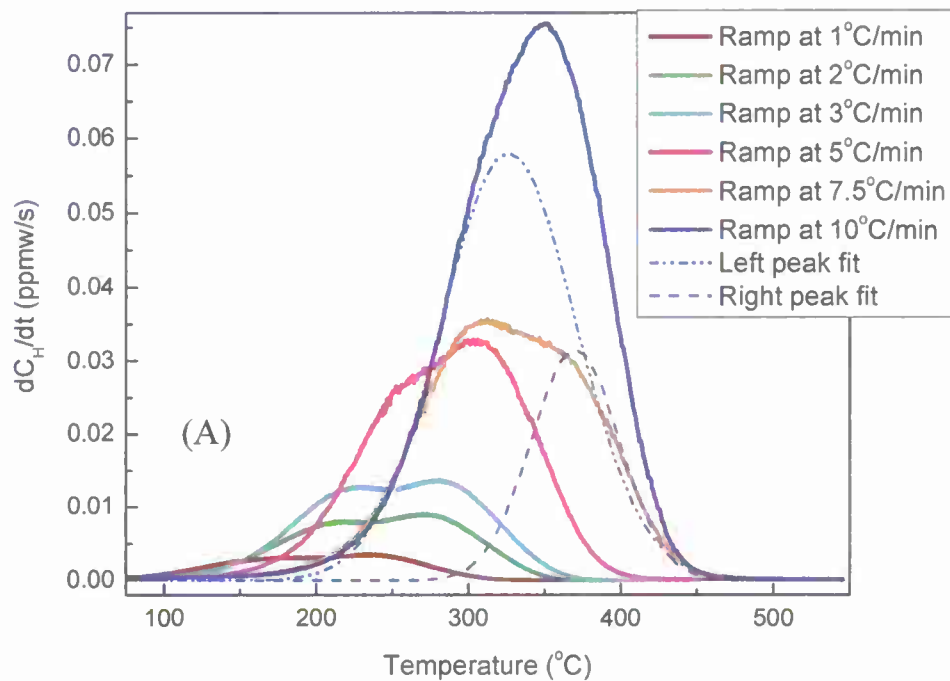


Figure 6. Ramped TDS experimental results at the various ramp rates for SHT + aged Monel K-500: (A) H desorption rate ( $dC_H/dt$ ) as a function of temperature and curve fitting, and (B) determination of the activation energies for the two fit H desorption peaks and their 95% confidence intervals. Specimens were H-charged for 10 days at room temperature and -1.20 V

vs. SCE in 0.6 M NaCl solution with pH adjusted to 8.0 with NaOH solution.

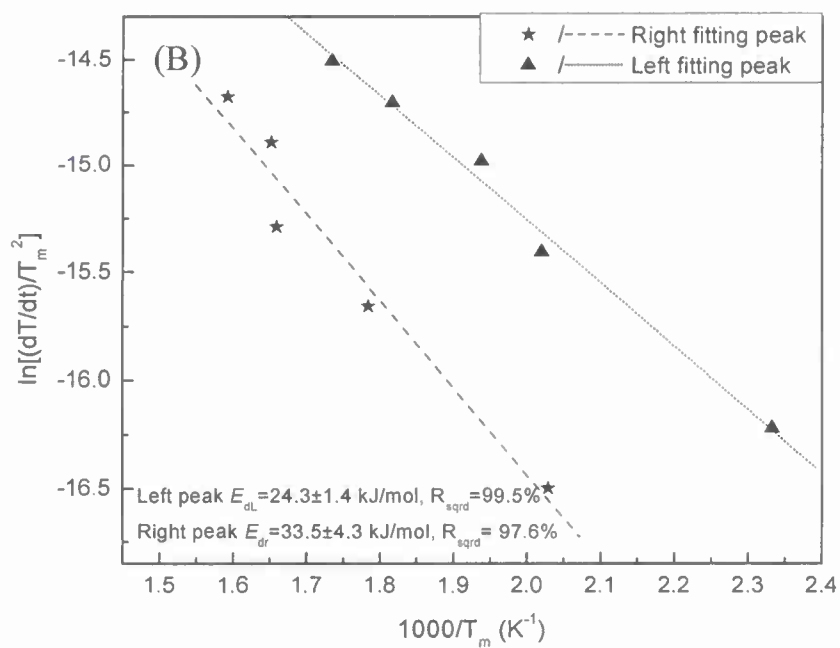
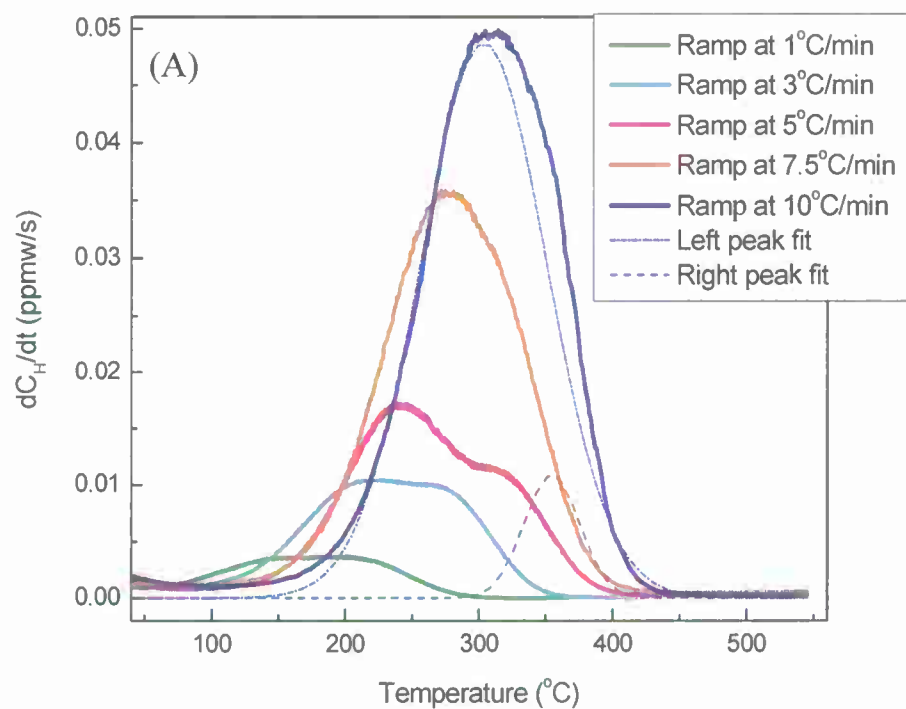


Figure 7. (A) H desorption rate ( $dC_H/dt$ ) as a function of temperature and (B) determination of the activation energies,  $E_{dr}$  and  $E_{dL}$  for the right and left peaks, respectively, and their 95% confidence intervals for H desorption from the ramped TDS experiments for SHT + CW + aged Monel K-500. Specimens were H-charged for 10 days at room temperature and -1.20 V vs. SCE in 0.6 M NaCl solution with pH adjusted to 8.0 with NaOH solution.

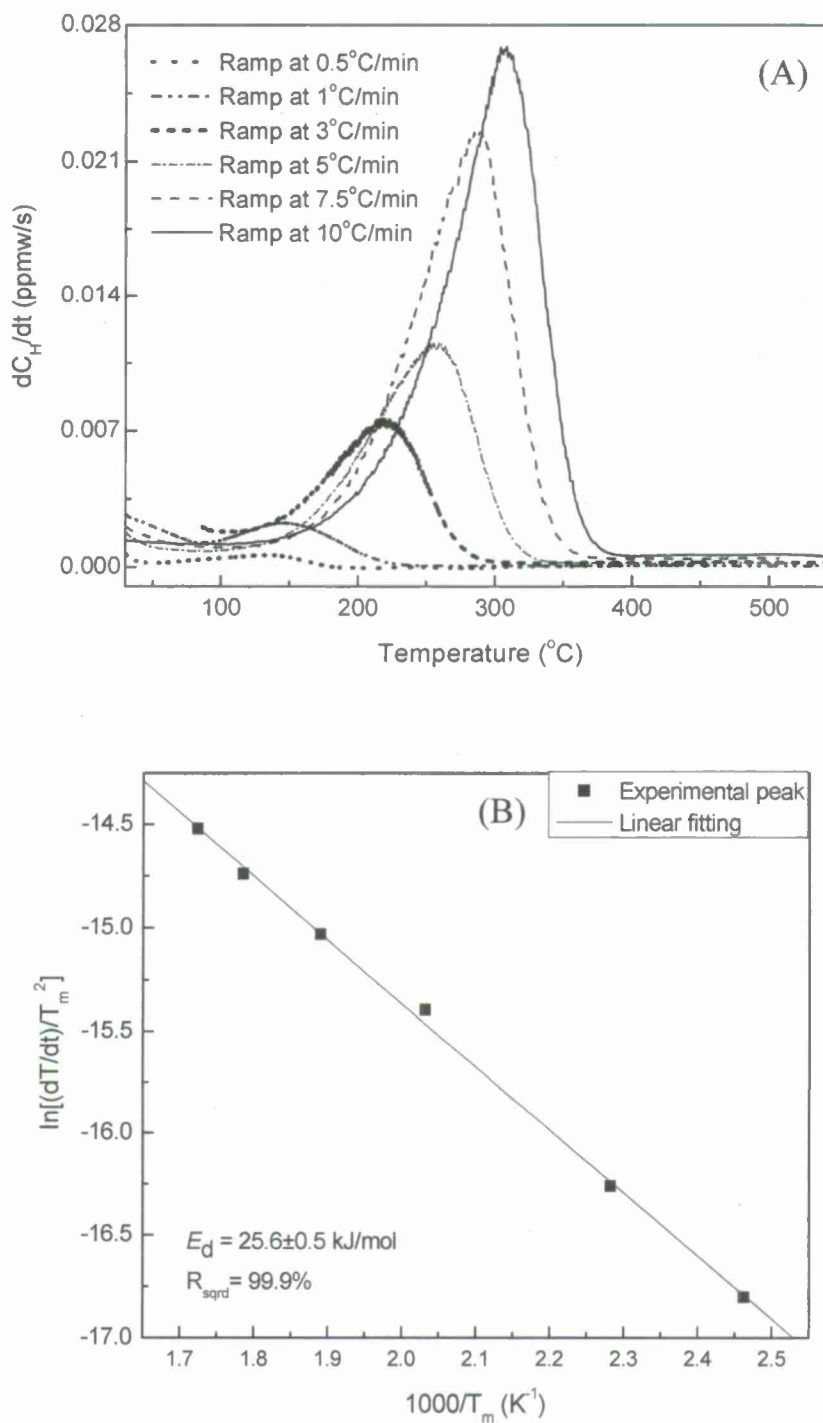
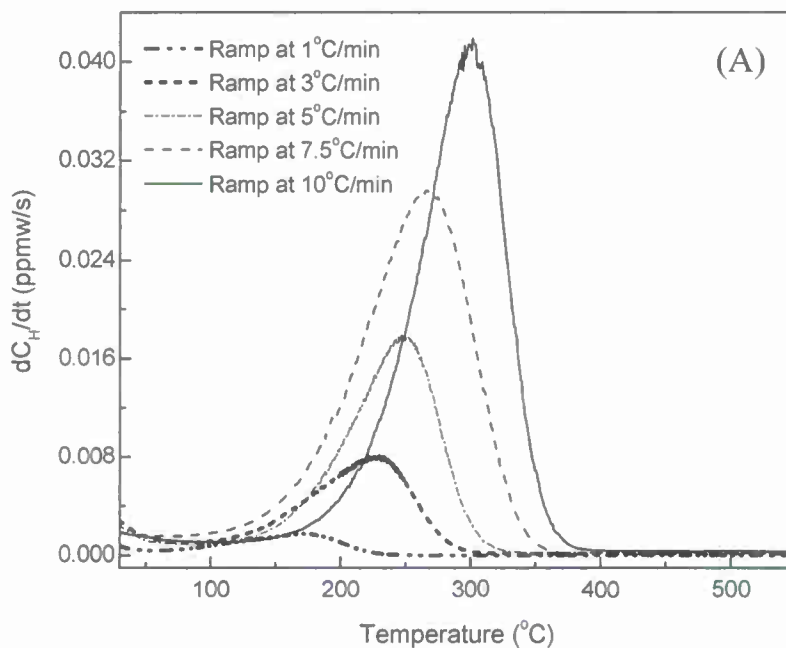


Figure 8. (A) H desorption rate ( $dC_H/dt$ ) as a function of temperature and (B) determination of the activation energy and its 95% confidence interval for H desorption from the ramped TDS results for SHT + WQ Monel K-500. Specimens were H-charged for 10 days at room temperature and -1.20 V vs. SCE in 0.6 M NaCl solution with pH adjusted to 8.0 with NaOH solution.





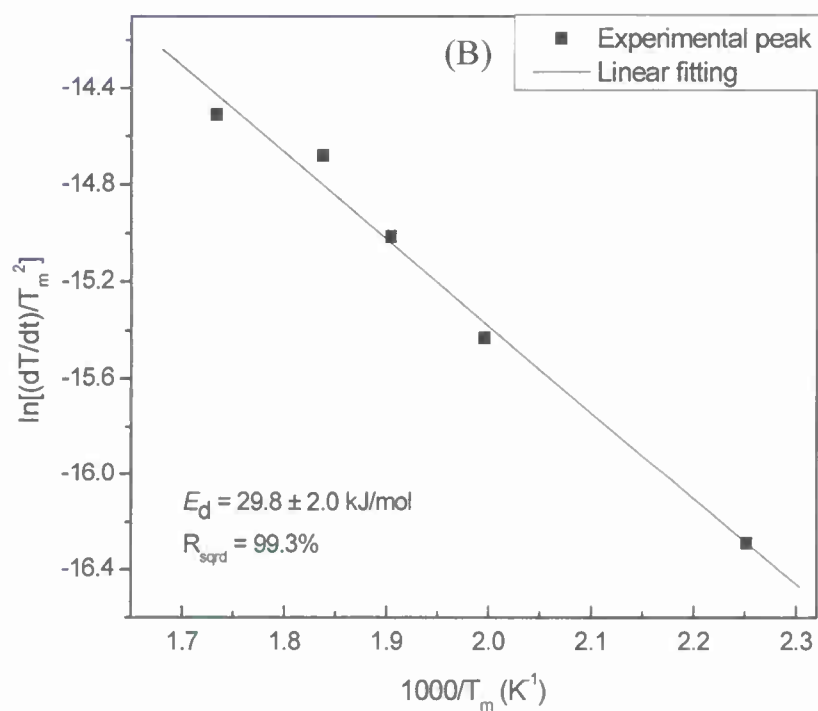


Figure 9. (A) H desorption rate ( $dC_H/dt$ ) as a function of temperature and (B) determination of the activation energy and its 95% confidence interval for H desorption from the ramped TDS results for SHT + AC + CW Monel K-500. Specimens were H-charged for 10 days at room temperature and -1.20 V vs. SCE in 0.6 M NaCl solution with pH adjusted to 8.0 with NaOH solution.

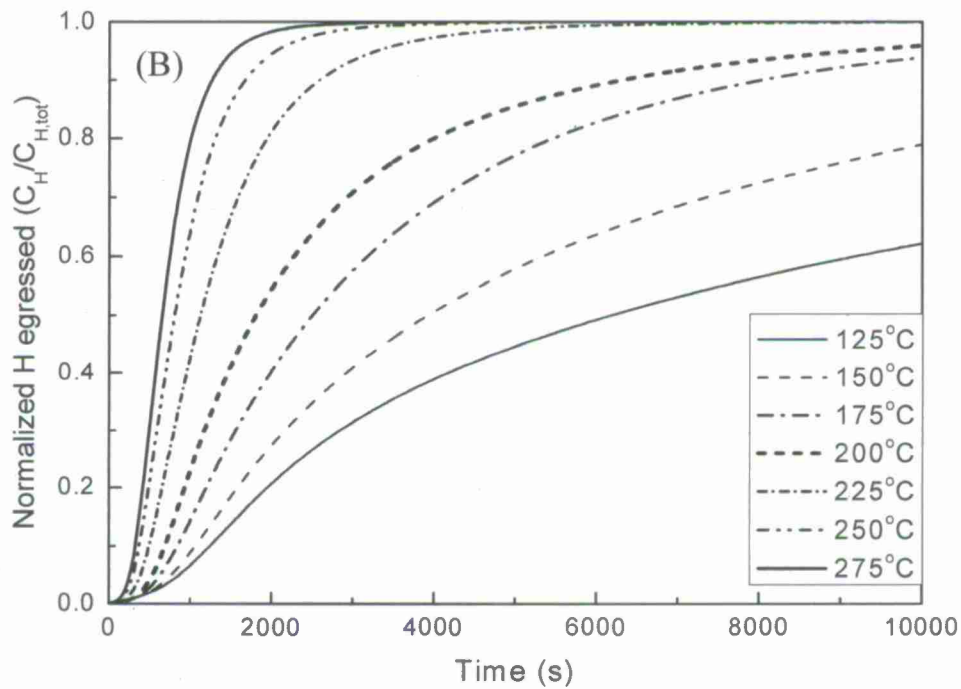
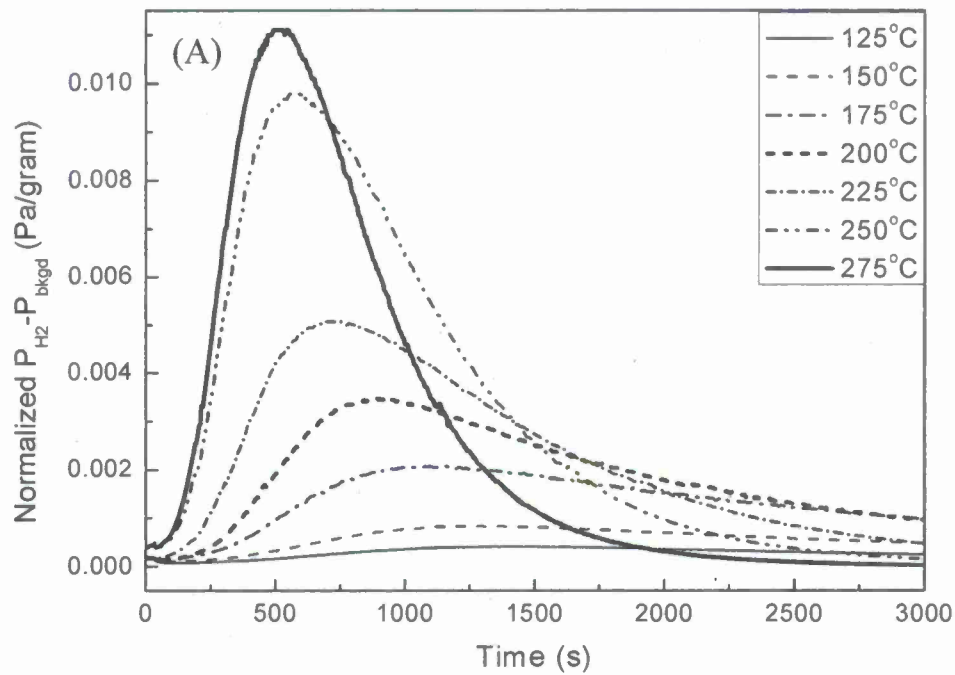


Figure 10. Isothermal TDS results measured at various temperatures for SHT + aged Monel K-500 specimens. (A) net H<sub>2</sub> pressure as a function of time, (B) normalized H concentration egressed,  $C_H$  by total H concentration,  $C_{H,tot}$ , from integrated pressure vs. time data showing fraction of  $C_{H,tot}$  egressed as a function of time. Specimens were H-charged for 10 days at 60°C

and -1.475 V vs. Hg/HgSO<sub>4</sub> in 0.0214 M Na<sub>2</sub>B<sub>4</sub>O<sub>7</sub>·10H<sub>2</sub>O + 0.1144 M H<sub>3</sub>BO<sub>3</sub> (pH ~8.4).

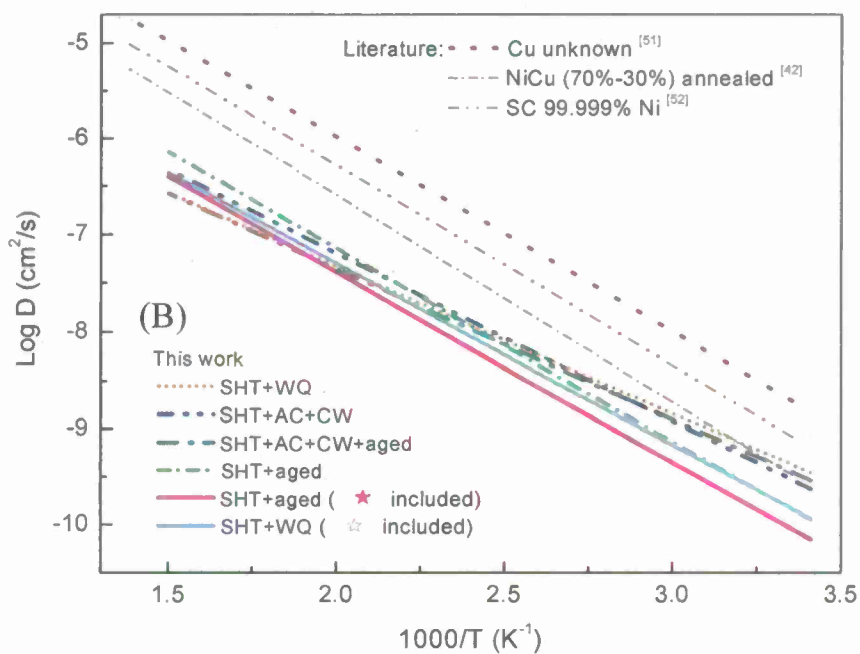
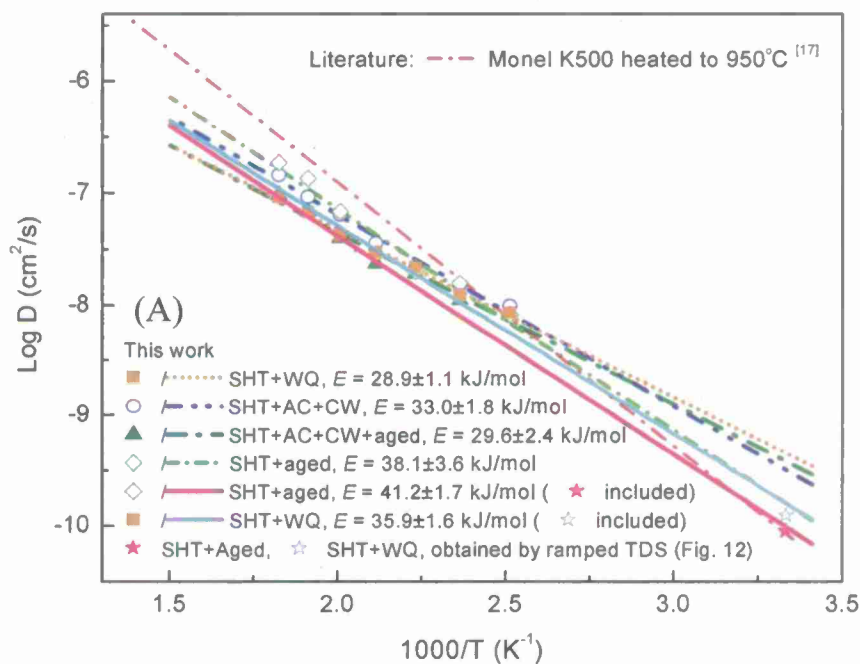


Figure 11. (A) The temperature dependence of effective H diffusivity for SHT + AC + CW, SHT + AC + CW + aged, SHT + WQ, and SHT + aged Monel K-500 and (B) compared to literature results (Table 4). Specimens used in this work were H-charged for 10 days at 60°C and -1.475 V vs. Hg/HgSO<sub>4</sub> in 0.0214 M Na<sub>2</sub>B<sub>4</sub>O<sub>7</sub>·10H<sub>2</sub>O + 0.1144 M H<sub>3</sub>BO<sub>3</sub> (pH ~8.4). The room temperature data were obtained by saturation curve analysis and all high temperature H diffusivities were obtained by isothermal TDS.

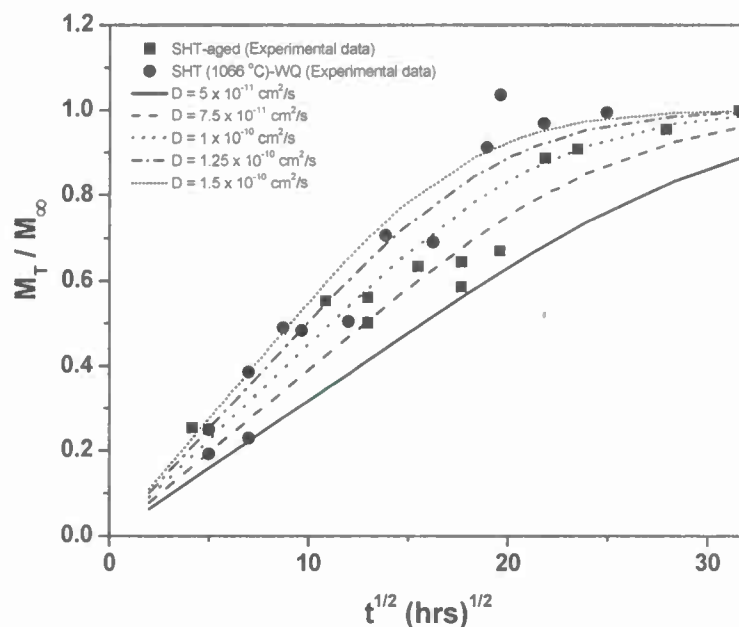


Figure 12. Absorbed hydrogen concentration expressed as fractional fully saturated level,  $M_T/M_\infty$ , versus hydrogen charging time to the  $1/2$  power. A series of assumed H diffusion coefficients are plotted as lines utilizing Equation 3. The experimental data were determined by TDS for the SHT at 982°C + aged Monel K-500 and SHT at 1066°C + WQ Monel K-500 after various exposure times after hydrogen charging at -0.9 V<sub>SCE</sub> and room temperature in 0.0214 M Na<sub>2</sub>B<sub>4</sub>O<sub>7</sub>·10H<sub>2</sub>O + 0.1144 M H<sub>3</sub>BO<sub>3</sub> (pH ~8.4) solution.

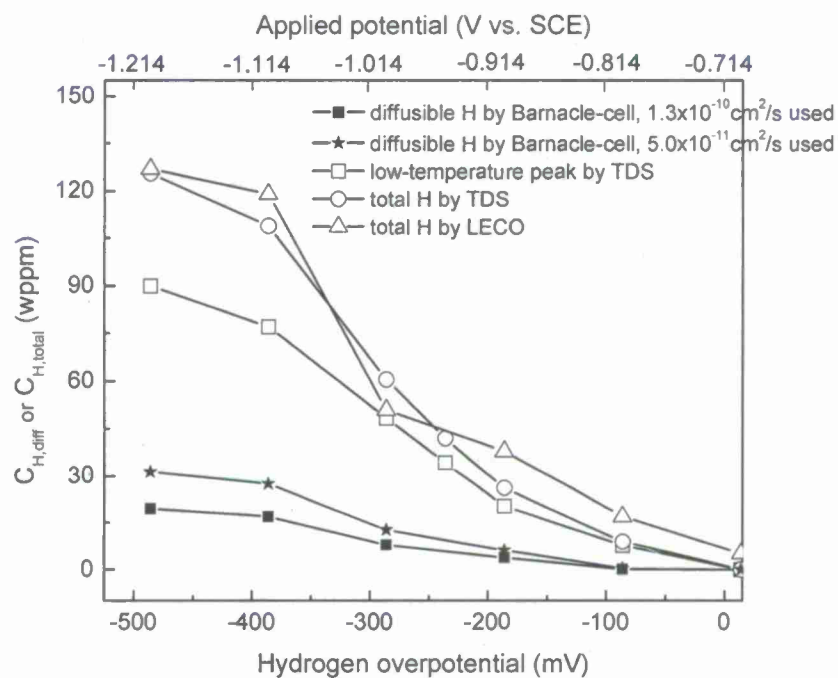


Figure 13. Comparison of H concentration results obtained by Barnacle-cell, TDS and LECO methods for SHT + aged Monel K-500:  $C_{H, diff}$  or  $C_{H, total}$  vs. over-potential. Before TDS or LECO, samples were H-charged for 10 days at room temperature and various over-potentials in 0.6 M NaCl solution with pH adjusted to 8.0 with NaOH solution. The H diffusion coefficients shown in the legend represent intermediate and lower bound values from TDS analyses.

## **Task 1**

**Crack Tip Hydrogen Concentrations Determined from Rescaled Crevices to  
Simulate Crack Tips**

**Predicting Diffusible Hydrogen Concentrations in Simulated Monel K-500 Crack Tips  
Using Rescaled Crevices and Finite Element Modeling of Current and Potential  
Distributions**

Hung M. Ha<sup>1</sup>, Francisco Presuel-Moreno<sup>2</sup>, John. R. Scully<sup>1</sup>

<sup>1</sup>Center for Electrochemical Science and Engineering  
Department of Materials Science and Engineering  
University of Virginia, Charlottesville VA 22904

<sup>2</sup>Florida Atlantic University  
Dept. Ocean & Mechanical Engineering  
101 North Beach Road  
Dania Beach, FL 3300

**Abstract**

Rescaled crevices were employed to determine local potential and pH information applicable to a simulated crack tip. The information on hydrogen over potential based on local applied potential and pH was used to calculate the diffusible hydrogen concentration,  $C_{H,diff}$ . The procedures and results for determining  $C_{H,diff}$  using the Barnacle cell method and TDS are reported elsewhere [1].  $C_{H,diff}$  versus potential data was acquired on planar electrodes in solutions at various pH levels. This data was used to assign a  $C_{H,diff}$  value at various  $x/G$  and  $x^2/G$  values in rescaled crevices corresponding to the precise local overpotential and pH existing as a function of position at a given applied potential at the crack mouth.  $C_{H,diff}$  was a strong function of applied cathodic potential and highest at the mouth at all cathodic applied potentials and decreased with increase in  $X^2/G$ . However,  $C_{H,diff}$  in rescaled crevices reached an approximately constant level at  $X^2/G$  greater than 100.  $C_{H,diff}$  as 20 wppm was obtained at -1.1 V vs. SCE for an  $X^2/G$  value of 90 cm suggested to represent a crack tip. At the surface of Monel K-500 the  $C_{H,diff}$  could be as high as >35 wppm.



## Introduction

Hydrogen embrittlement (HE) has significant impact on the integrity of components and structure [2]. HE cracking may result in fast fracture after environmental slow crack over long periods determined by the environment assisted crack velocity [3-8]. Many quantitative models have been proposed to predict the HE crack growth rate based on different assumption about the rate determining process for crack growth [9-16]. One of the important input parameters for these models is the H concentration at the crack tip fracture process zone relative to a critical hydrogen concentration for HE [10, 12, 13, 15]. The critical fracture process zone dimensions and the effective H diffusivity are other necessary parameters to predict the H environmental assisted crack velocity.

This paper reports the predicted diffusible H concentration at a simulated crack tip in Ni base alloy Monel K-500 at different cathodic applied potentials in 0.6 M NaCl solution. The dependence of diffusible H concentration at the crack tip on electrochemical potential and pH was reported elsewhere [1]. The potential and pH distribution inside the simulated crack tip was determined using rescaled crevice experiment. A computational finite element method was also utilized to predict the potential distribution inside the crack tip (not reported). Diffusible H concentration was calculated based on experimental and computational potential-pH information. The values obtained from these two approaches were comparable to each other.

## Experiment

Monel Alloy K-500 (UNS N05500) with the composition given in Table 1 was used in this study. The material was solution heat treated at 982°C (1800°F) followed by aging at 593°C (1100°F) for 16h, then at 538°C (1000°F) for 6h, then at 482°C (900°F) for 8h and finally air-cooled.

Table 1. Compositions (wt%) of Monel Alloy K-500 (UNS N05500) .

Elements	Ni %	Cu %	Al %	Fe %	Mn %	Si %	Ti %	C %	Co %	Cr %	Mo %	V %	Ta %	S+P+Sn+ Pb+B ppm
Wt%	63.69	30.20	2.69	1.66	0.58	0.14	0.61	0.169	0.007	0.11	0.061	0.008	0.016	<200

The rescaled crevice cell was constructed using three main parts: an acrylic bottom plate in which 6 specimens were embedded and shorted to form a continuous working electrode, a plastic shim to create the crevice gap and an acrylic top plate which forms the crevice and holds the micro reference electrodes (REs) for local potential measurements. A schematic of the crevice cell parts and a side-view of an assembled crevice cell are shown in Figure 1. Six Monel K-500 specimens each with surface areas around  $3 \text{ cm}^2$  were polished to a 600-grit finish and degreased with ethanol. The specimens were then mounted in the bottom acrylic plate. The specimens are at the distances of  $x = 1, 3, 5, 7,$  and  $9 \text{ cm}$  away from the crevice opening. The specimens were shorted together to form a continuous working electrode (WE). The plastic shim was used to create a  $1 \text{ mm}$  crevice gap (G). The top plate could then be placed on top of the plastic shim to create the crevice with a  $1 \text{ mm}$  gap. Vacuum grease was used to maintain a tight seal on the crevice components. Local potential values were measured using Ag/AgCl micro-Res prepared by the procedure reported elsewhere [17]. The Ag/AgCl micro reference electrodes were calibrated against the SCE reference electrode before each run. Local pH values were measured using pH indicator paper inserted into the crevice cell. The electrolyte in all experiments was  $0.6 \text{ M NaCl}$  and the cell was open to air.

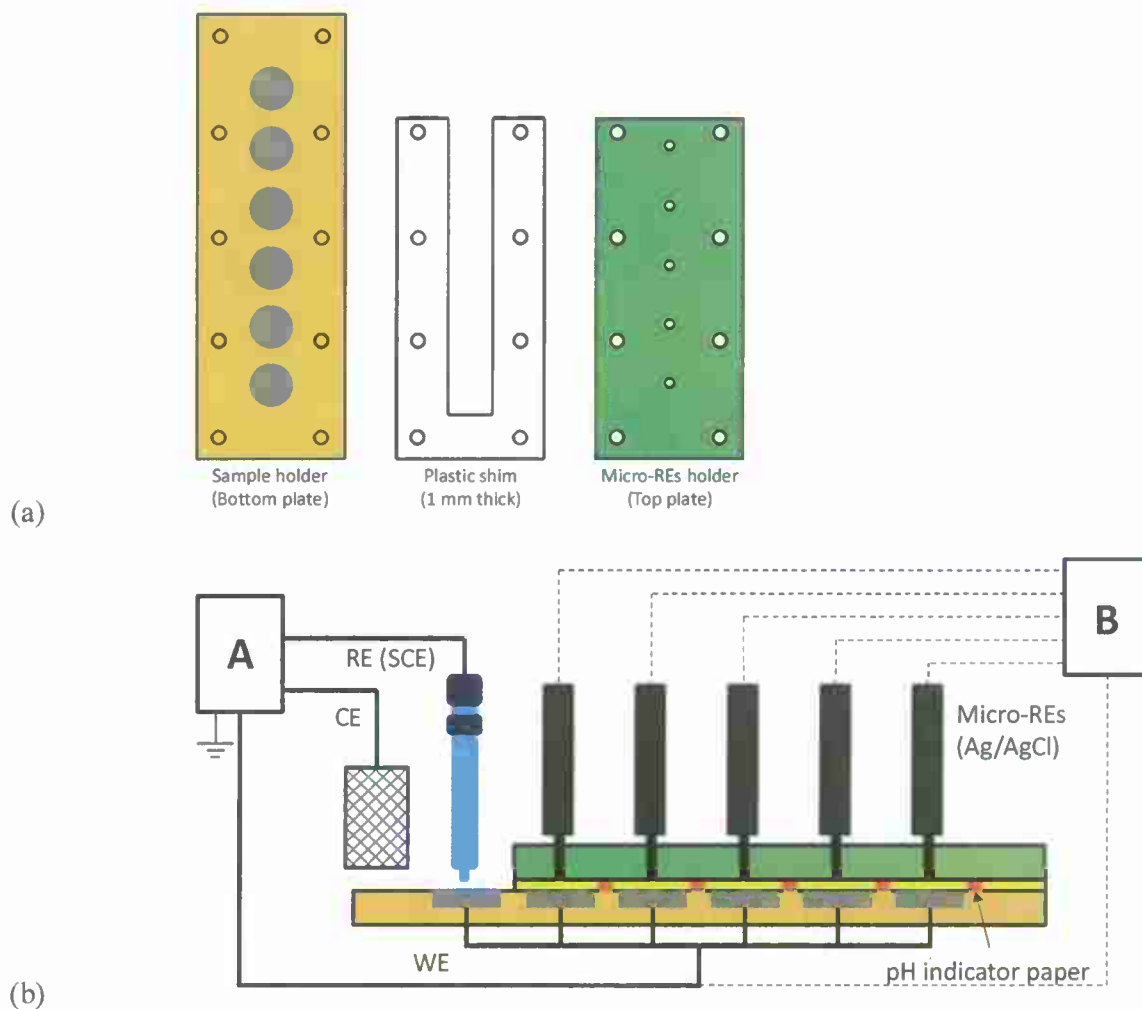


Figure 1. (a) The rescaled crevice basic components: bottom plate sample holder, plastic shim, and top plate with micro-REs holder, (b) An illustration of the rescaled crevice electrochemical cell components where A is the PAR model 273A Potentiostat, B is the Keithley 2001 multimeter used to measure local potential.

## Results

Figure 2 shows the local potential measured at different distances from the crevice opening at different applied potentials of -0.6, -0.7, -0.8, -0.9 and -1.0  $V_{SCE}$ . In all experiments, a potential gradient inside the crevice was established after the external potential was applied. It was observed that the local potential increased as the distance from the crevice opening increased. In addition, the local potentials and the potential gradient decreased with time.

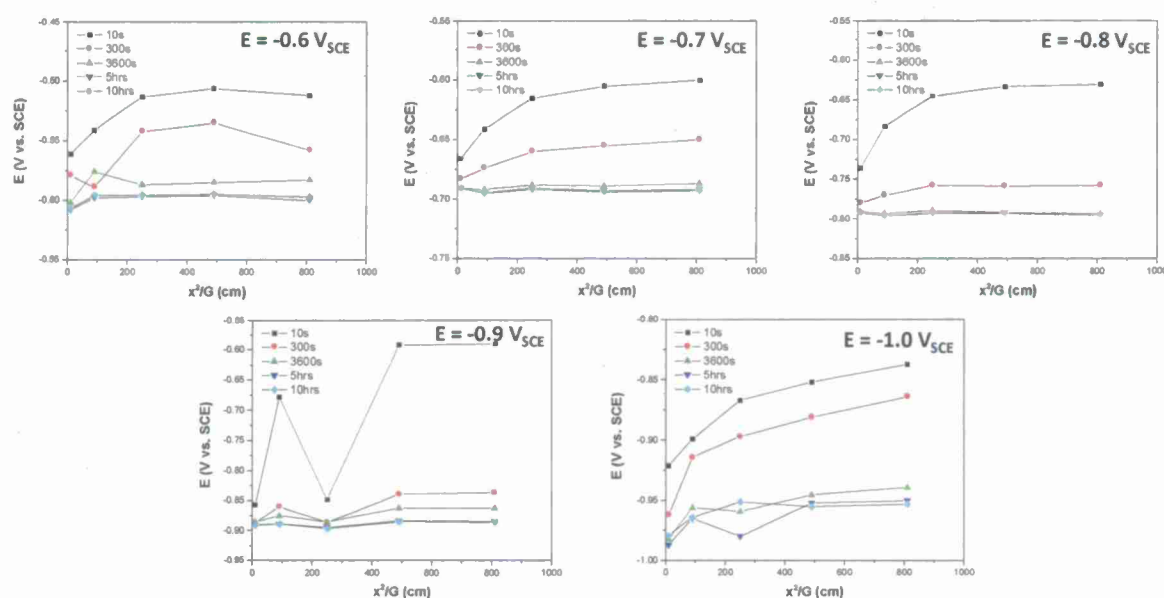


Figure 2. Local potential measured at different locations along the crevice at different external applied potential of (a) -0.6, (b) -0.7, (c) -0.8, (d) -0.9 and (e) -1.0  $V_{SCE}$ . The crevice gap was fixed at  $G = 1$  mm.

Figure 3 shows the pH distribution outside ( $x = 0$ ) and inside the crevice ( $x = 1, 3, 5, 7$  and  $9$  cm) at different external applied potentials after 300 seconds and 10 hours. No significant pH difference was observed inside the crevice. However, pH values were dependent on the applied potential and the time after the potential was applied. The pH increased with more negative applied potential and with time. The maximum pH was recorded at 11 after 10 hours at all applied potentials.

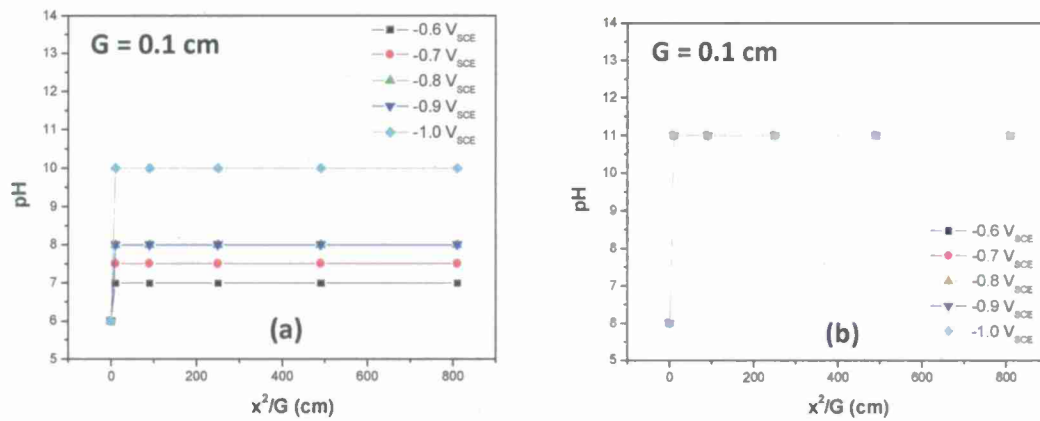


Figure 3. Local pH measured at different locations along the crevice at different external applied potential of -0.6, (b) -0.7, (c) -0.8, (d) -0.9 and (e) -1.0 V<sub>SCE</sub>. The measurement was recorded at (a) 300 seconds and (b) 10 hours after the external potential was applied. The crevice gap was fixed at G = 1 mm.

The distribution of the hydrogen overpotential inside the crevice at different applied potential after 300 seconds and 10 hours is shown in Figure 4. At the applied potentials of -0.6 and -0.7 V<sub>SCE</sub>, the overpotentials for H evolution were positive which suggests no H was generated. At more negative potentials such as -0.8 and -0.9 V<sub>SCE</sub>, the H overpotential was negative for a short time (e.g. 300 seconds) but increased to positive for longer time (e.g. 10 hours). At -1.0 V<sub>SCE</sub>, the overpotential for H evolution was negative during the whole experiment indicating H was generated at all time. However, the overpotential became less negative with distance from the crevice opening and with time.

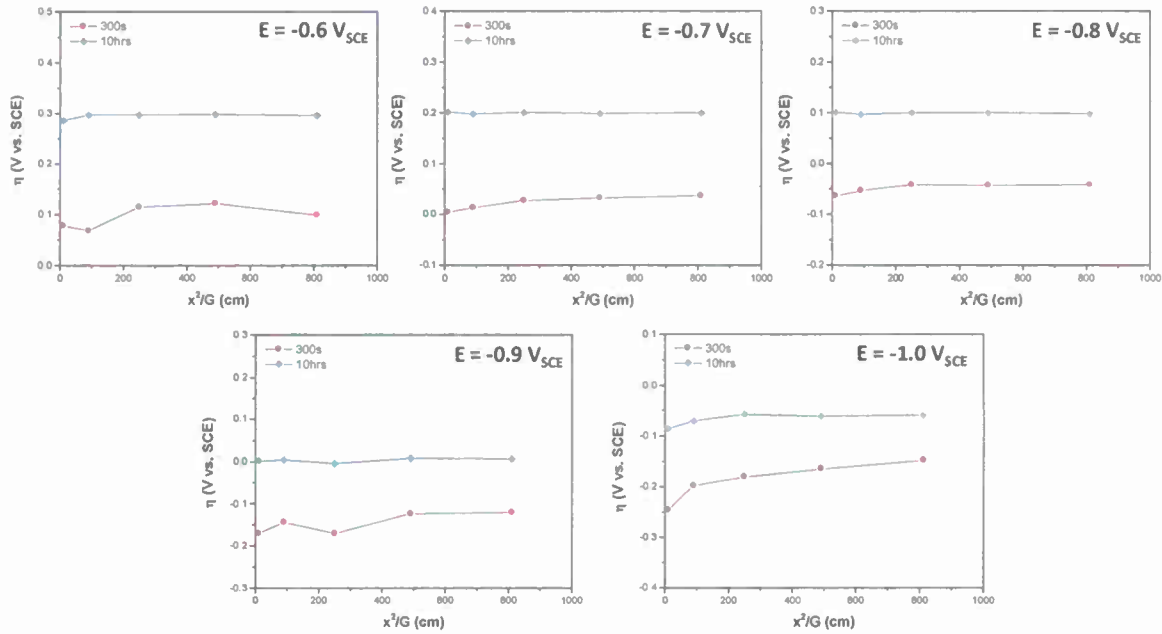


Figure 4. Local overpotential calculated at different locations along the crevice at different external applied potential of -0.6, (b) -0.7, (c) -0.8, (d) -0.9 and (e) -1.0  $\text{V}_{\text{SCE}}$ . The values were calculated at (a) 300 seconds and (b) 10 hours after the external potential was applied. The crevice gap was fixed at  $G = 1 \text{ mm}$ .

The information on hydrogen over potential based on local applied potential and pH was combined and used to calculate the subsurface diffusible H concentration,  $C_{\text{H,diff}}$ . The procedures and results for determining  $C_{\text{H,diff}}$  using the Barnacle cell method and TDS are reported elsewhere [1].  $C_{\text{H,diff}}$  versus potential data was acquired on planar electrodes in solutions at various pH levels. This data was used to assign a  $C_{\text{H,diff}}$  value at various  $x^2/G$  values in rescaled crevices corresponding to the precise overpotential and pH existing at that applied potential at the crack mouth. The plots showing the pH values used in the calculations are reported in Figures 3. This data could be used to determined  $C_{\text{H,diff}}$  versus  $x^2/G$  and applied potential that is representative of cracks.

The calculated subsurface  $C_{\text{H,diff}}$  inside the rescaled crevice as function of the applied potential is shown in Figure 5a. At a constant distance from the crevice mouth, i.e. constant  $x^2/G$ ,  $C_{\text{H,diff}}$  decreased with increasing the applied potential to more anodic direction (Figure 5a). Figure 5b shows an inverse relationship between  $C_{\text{H,diff}}$  and the distance from the crevice mouth. Moreover, In addition,  $C_{\text{H,diff}}$  decreased faster at locations near the crevice month compared to

locations deep inside the crevice (Figure 5a). For instance, at the applied potential of  $-1.0 \text{ V}_{\text{SCE}}$  the  $C_{\text{H,diff}}$  decreased from 72 to 41 wppm as  $x^2/G$  increased from 0 to 10 cm, however, it only decreased further to 22 wppm as  $x^2/G$  increased to 810 cm. The relationships between  $C_{\text{H,diff}}$  and  $E_{\text{applied}}$  and between  $C_{\text{H,diff}}$  and  $x^2/G$  (Figure 5) is the result of the dependence of the H evolution overpotential on  $E_{\text{applied}}$  at the crevice mouth and pH inside the crevice.

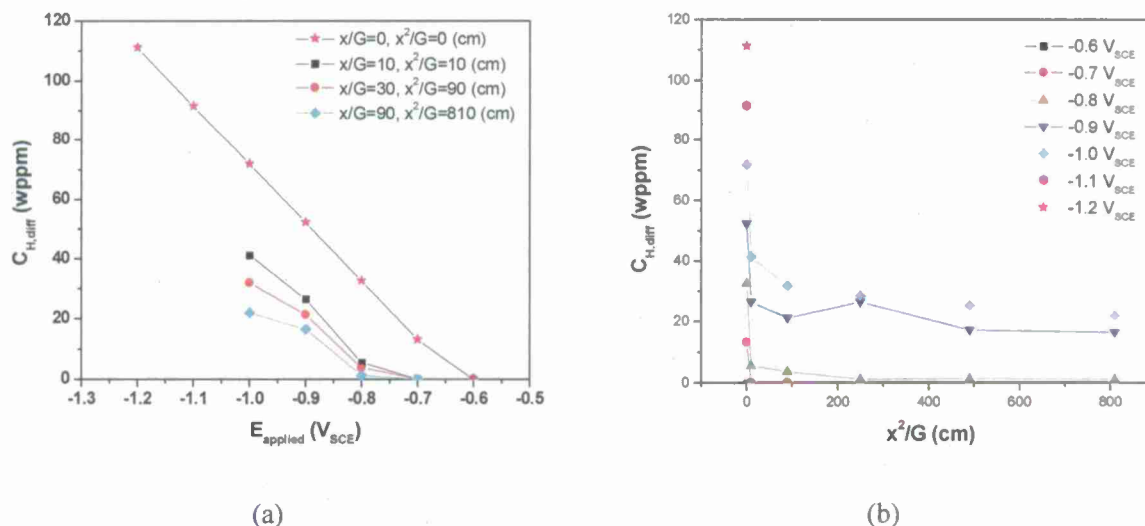


Figure 5. Calculated subsurface diffusible H concentration at different locations inside the rescaled crevice made of Monel K-500 provided by Special Metals. The applied potential varied from  $-0.6$  to  $-1.2 \text{ V}_{\text{SCE}}$ . (a)  $C_{\text{H,diff}}$  distribution as a function of applied potential and (b)  $C_{\text{H,diff}}$  distribution as a function of  $x^2/G$ . The calculation of  $C_{\text{H,diff}}$  based on the measured values of the potential and pH distribution at specific locations inside the rescaled crevice.

## Conclusions

Rescaled crevices were quantified as a function of the  $X^2/G$  and  $x/G$  scaling parameters. Diffusible hydrogen concentration ( $C_{\text{H,diff}}$ ) was determined at re-scaled crack tips from information on pH and local  $E_{\text{app}}$ . Hydrogen overpotential could be determined from this information as a function of crevice position quantified as  $X^2/G$ . From the relationships between  $E_{\text{app}}$ , pH and diffusible hydrogen concentration, the hydrogen concentration versus externally applied potential was determined at various  $X^2/G$  values. A value of  $C_{\text{H,diff}}$  of 20 wppm was



obtained at -1.1 V vs. SCE for an  $X^2/G$  value of 90 cm suggested to represent a crack tip. At the surface of Monel K-500 the  $C_{H,diff}$  could be as high as >35 wppm at the same potential.

### Acknowledgements

We gratefully acknowledge support from ONR Grant N00014-10-1-0552 under the direction of Dr. Airan Perez. Special Metals Corporation is also acknowledged for supply of Monel K-500 rod as well as further discussions.

### References

1. J. Ai, H. Ha, R.P. Gangloff and J.R. Scully, *Submitted to Acta Materialia*,
2. R.P. Gangloff, in *Comprehensive Structural Integrity*, (New York: Elsevier Science, J.P.a.P. Scott, Editor, p. 31-101, Elsevier Science: New York.(2003)
3. R.A. Oriani, in *Fundamental Aspects in Stress Corrosion Cracking*, R.W. Staehle, A.J. Forty and D.V. Rooyen, Editors, p. 32-50, NACE, Houston, TX (1967)
4. R.A. Oriani, *Berichte der Bunsengesellschaft für physikalische Chemie*, **76**, p. 848-857 (1972)
5. R.A. Oriani and P.H. Josephic, *Acta Metallurgica*, **25**, p. 979-988 (1977)
6. A. Turnbull, *Corrosion Science*, **34**, p. 921-960 (1993)
7. J.R. Scully and M.G. Vassilaros, in *DTNSRDC SME 84-69*, p. 1-28, (1984)
8. C. Price and R. Fredell, *Metallurgical and Materials Transactions A*, **17**, p. 889-898 (1986)
9. W. Gerberich and Y. Chen, *Metallurgical and Materials Transactions A*, **6**, p. 271-278 (1975)
10. W. Gerberich, Y. Chen and C. John, *Metallurgical and Materials Transactions A*, **6**, p. 1485-1498 (1975)
11. W. Gerberich, T. Livne, X. Chen and M. Kaczorowski, *Metallurgical and Materials Transactions A*, **19**, p. 1319-1334 (1988)
12. N.R. Moody, M.W. Perra and S.L. Robinson, *Scripta Metallurgica*, **22**, p. 1261-1266 (1988)
13. R.W. Pasco and P.J. Ficalora, *Acta Metallurgica*, **31**, p. 541-558 (1983)
14. H.P. Van Leeuwen, *Engineering Fracture Mechanics*, **6**, p. 141-161 (1974)
15. J. Galvele, *Corrosion Science*, **27**, p. 1-33 (1987)
16. Y. Lee and R. Gangloff, *Metallurgical and Materials Transactions A*, **38**, p. 2174-2190 (2007)
17. A.W. Hassel, K. Fushimi and M. Seo, *Electrochemistry Communications*, **1**, p. 180-183 (1999)

**Task 2**  
**Predictions of the Effect of Crack Tip H Concentration and Diffusivity on**  
**Crack Propagation Properties and Component Performance**

## MEASUREMENT AND MODELING OF HYDROGEN ENVIRONMENT ASSISTED CRACKING IN MONEL K-500

Richard P. Gangloff, Hung Ha, James T. Burns and John R. Scully

Center for Electrochemical Science and Engineering  
Department of Materials Science and Engineering  
University of Virginia  
Charlottesville, VA 22904-4745

### ABSTRACT

The objectives of this research are to: (1) quantitatively characterize the hydrogen environment assisted cracking (HEAC) kinetics of aged Monel K-500 relevant to aqueous chloride exposure and cathodic polarization, (2) determine the concentration dependence of diffusible hydrogen (H) produced in the crack tip fracture process zone, versus applied-cathodic potential, (3) model the applied potential dependence of threshold stress intensity and Stage II crack growth rate based on crack tip H uptake and process H zone embrittlement mechanisms, and (4) employ accelerated-laboratory test results to probabilistically simulate the HEAC behavior of a component in marine service.

The rising displacement test method, with continuous-precision dcPD monitoring of a small crack provides an effective-accelerated characterization of environmental cracking in Monel K-500, particularly when enhanced to account for artifacts due to crack surface electrical contact, highly localized crack tip plasticity under small-scale yielding, and small-specimen ligament plasticity. An analytical J-integral analysis characterizes HEAC in Monel K-500, without the need to measure displacement or unloading compliance, thus providing material-property data for simulation of cracking in a larger and elastically loaded structure. Solution treated and aged Monel K-500 is susceptible to severe intergranular HEAC in NaCl solution when under cathodic polarization in the range of  $-800 \text{ mV}_{\text{SCE}}$  and higher. Such cracking is eliminated by reduced cathodic polarization in the range of  $-750 \text{ mV}_{\text{SCE}}$  and lower. HEAC in Monel K-500 is exacerbated

by rising  $K$  and active crack tip strain rate, compared to quasi-static loading, but only for environmental conditions where cracking is mild to moderate.

A rescaled crevice model, coupled with measured-local crevice potential and pH, was combined with a H uptake law measured by thermal desorption spectroscopy for Monel K-500, to establish the strong effect of applied potential on crack tip H concentration. Diffusible H concentration produced at the crack tip in Monel K-500 decreased with increasing applied potential and was essentially below the experimental resolution limit for applied potentials above  $-764 \text{ mV}_{\text{SCE}}$ . Good agreement between the measured and micromechanical model predicted dependencies of  $K_{\text{TH}}$  and Stage II crack growth rate on applied-cathodic potential supports the conclusion that a critical level of cathodic polarization must be exceeded before HEAC can progress at a significant rate in Monel K-500 stressed in NaCl. The precise level of this potential could depend on subtle differences in Monel metallurgy through microstructure and composition effects on H uptake, as well as on key parameters in the micromechanical models.

A probabilistic fracture mechanics-based program, *SCCrack*, predicts distributions of cracked-component life as limited by HEAC using the input from accelerated laboratory experiments strengthened by electrochemical measurements of crack tip H and micromechanical mechanism-based modeling. The effect of a distribution of applied-cathodic polarization on component life is strikingly strong, reflecting the dominant influence of cathodic polarization on rates of IG HEAC.

## INTRODUCTION

Monel K-500, an austenitic Ni-Cu-Al alloy, is precipitation hardened for relatively high yield high strength and fracture toughness, and resists marine-environment corrosion. However, failure analyses and laboratory testing demonstrate that this alloy is susceptible to significant environment assisted cracking (EAC) when stressed in chloride solutions with applied cathodic polarization in the range of  $-1000 \text{ mV}_{\text{SCE}}$ . Failures from EAC were reported for threaded bolts in North Sea oil and gas platforms [1-9] and submarine components [10,11] where cathodic polarization protects carbon and low alloy steels proximate to the Monel. Cracking was intergranular and limited transgranular EAC in Monel K-500 was reported for hydrofluoric acid vapor environments [12]. The perception is that EAC progresses over relatively long times on the order of 1 to 10 years in service. This field-cracking behavior is not unexpected given the well known susceptibility of precipitation hardened Ni-based superalloys to intergranular and transgranular EAC [13-16].

The mechanism for intergranular EAC of Monel K-500 in aqueous chloride solutions is broadly accepted to be hydrogen environment assisted cracking (HEAC). Atomic hydrogen (H) is produced on boldly exposed and occluded-crack tip surfaces by water reduction and migrates to the highly stressed crack tip fracture process zone (FPZ) [13]. While HEAC in a precracked specimen is often dominated by H production and uptake on crack tip surfaces due to the short diffusion distance ( $\sim 1 \text{ }\mu\text{m}$ ) [13], the long times for HEAC in Monel K-500 and possibility for reduced crack tip overpotential for H production relative to boldly exposed surfaces under cathodic polarization [17] suggest that both sources of H must be considered. Hydrogen cracking is likely promoted by hydrogen enhanced decohesion (HEDE), hydrogen enhanced localized plasticity (HELP), or adsorption induced dislocation emission (AIDE) [13,18]. Face-centered cubic hydride phase  $((\text{Ni,Cu})_x\text{H})$  can form at  $23^\circ\text{C}$  with H solubility in Monel K-500 in the range of 10 to 25 parts-per-million by weight (wppm) [19,20]. The mechanism for H-assisted cracking is controversial, but recent transmission electron microscopy suggests interactive HEDE and HELP; boundary decohesion is enabled by local stress elevation from strain hardening and H transport from dislocation plasticity [21]. This microscopy did not

evidence either hydride phase [20] or the hypothesized presence of nano-scale cracking from hydride precipitation [20] or super-abundant vacancy stabilization [22].

The case for the intergranular HEAC mechanism is circumstantial but strong. Pure Ni is susceptible to intergranular HEAC in electrolytes, particularly under cathodic polarization and in acid solutions [16], as well as in low pressure-high purity H<sub>2</sub> [23]. Precharged H causes intergranular H assisted cracking (IHAC) in pure Ni [24,25], Ni-Cu solid solutions [20], and Fe-based and Ni superalloys [26,27]. The extent of intergranular cracking and degradation in mechanical property, each decreases with increasing H concentration. Quantitative studies on IN718 showed that the threshold stress intensity factor for HEAC in either high pressure H<sub>2</sub> or acidified chloride decreased as a unique function of increasing H produced at the crack tip [14]. The crack path transitioned from slip-band based transgranular to intergranular with increasing concentration of crack tip H [14]. Such a detailed quantitative correlation has not been reported for Monel K-500 in aqueous chloride solution, but the severity of HEAC in this system appears to increase with increasing applied-cathodic potential [2,28,29], which increases the overpotential for H production from water reduction and the amount of H uptake on bold surfaces and at the crack tip [17]. Several studies established that the normally ductile microvoid cracking mechanism in Monel K-500 transitions to intergranular cracking due to precharged H followed by static loading in moist air (at 175 – 260°C) [30], slow-rate monotonic deformation in air at 25°C [29,31], and air fatigue at 25°C [32] (crack path not reported). Harris et al. reported that the extent of intergranular cracking increased with increasing concentration of precharged H [31]. Finally, a lower strength solid solution alloy (Monel K-400) was susceptible to intergranular (and transgranular) cracking from liquid mercury embrittlement and precharged H embrittlement [33,34].

The majority of studies used the slow strain rate method applied to a smooth specimen to demonstrate HEAC of Monel K-500 in chloride solutions and isolate causal factors [2-6,10,29,31,35,36]. These experiments and analyses of field failures did not identify a particular metallurgical factor responsible for HEAC of Monel K-500. Candidates included high hardness (~R<sub>C</sub> 35-40) from cold work prior to aging, major-element composition variation, grain boundary carbides/graphite, segregated impurities such as S, P or Se [24], and grain boundary misorientation [37]. While these results

suggest that HEAC is intrinsic to Monel K-500, consistent with general experience with Ni-based alloy EAC [16], additional study of critical metallurgical factor(s) is required using refined probes and models of HEAC, H uptake, and grain boundary chemistry and structure. This issue is outside the scope of the present study. The present study focuses on measurement and application of fracture mechanics-based crack growth rate data in mechanism-based and component prognosis modeling. Except for limited studies which reported apparent threshold properties [28,38], fracture mechanics-based results are lacking for Monel K-500 in aqueous chloride solutions as detailed in the Discussion.

It is critical to develop mechanism-based models which predict quantitative HEAC kinetics to leverage experimental data and trends which are time-consuming to obtain. The HEDE mechanism provides a basis for micromechanical models which predict threshold stress intensity ( $K_{TH}$ ) as well as the K-independent Stage II crack growth rate ( $da/dt_{II}$ ) which is controlled by the rate limiting step in the H production and diffusion steps associated with crack tip FPZ damage [13]. The model for  $K_{TH}$  developed by Gerberich and coworkers [39] successfully predicted the applied potential and  $H_2$  pressure dependencies of HEAC in high strength steels [39-41]:

$$K_{TH} = \frac{1}{\beta'} \exp \frac{(k_{IG} - \alpha C_{H\sigma})^2}{\alpha'' \sigma_{YS}} \quad (1)$$

where  $\beta'$  ( $(MPa\sqrt{m})^{-1}$ ) and  $\alpha''$  ( $MPa \cdot m$ ) are constants in the dislocation based model of crack tip stresses [39],  $C_{H\sigma}$  (atom fraction) is the crack tip diffusible and stress enhanced H concentration trapped adjacent to the H-assisted crack path in the FPZ, and  $\alpha$  ( $(MPa\sqrt{m}(\text{atom fraction H})^{-1})$ ) is an adjustable weighting factor which defines the lowering of the Griffith toughness ( $k_{IG}$ ,  $MPa\sqrt{m}$ ) per unit H concentration. The upper bound model for the Stage II rate of K-independent H cracking ( $da/dt_{II}$ ) was validated for FPZ-H diffusion control in a wide variety of high strength alloys [42]:

$$\left(\frac{da}{dt}\right)_{II} = \frac{4D_H}{x_{crit}} \left\{ \text{erf}^{-1} \left( 1 - \frac{C_{crit}}{C_{H\sigma}} \right) \right\}^2 \quad (2)$$

where  $D_H$  is the trap affected diffusivity of H,  $x_{crit}$  is the critical distance ahead of the crack tip where H cracking nucleates,  $C_{crit}$  is the critical concentration of H for cracking. For



both Eqn. 1 and 2,  $C_{H\sigma}$  is the crack tip H in equilibrium with the local over-potential for H production:

$$C_{H\sigma} = C_L \exp\left(\frac{\sigma_H V_H + E_B}{RT}\right) = C_{H-Diff} \exp\left(\frac{\sigma_H V_H}{RT}\right) \quad (3)$$

where  $C_L$  is the concentration of lattice-dissolved H,  $\sigma_H$  is crack tip hydrostatic stress typically given by a factor of 3 to 10 times the alloy yield strength ( $\sigma_{YS}$ ) [43],  $V_H$  is the partial molar volume of H in Ni,  $E_B$  is the binding energy of H to the microstructure adjacent to the crack tip,  $C_{H-Diff}$  is the concentration of diffusible H, and  $RT$  has the usual meaning. Both  $C_L$  and  $C_{H-Diff}$  in Eqn. 3 are estimated for the location adjacent to the H crack path. A range of EAC data for Ti, Fe, Al and Ni-based alloys suggested that  $x_{crit}$  is 1  $\mu m$  for the fastest possible  $da/dt_{II}$  where  $C_{H\sigma}$  approaches  $C_{Crit}$  and the inverse error function term tends toward 1.0. The  $D_H$  for H in aged Monel K-500 at 25°C was reported to be  $5 \times 10^{-11} \text{ cm}^2/\text{s}$  [32],  $1.5$  to  $1.9 \times 10^{-10} \text{ cm}^2/\text{s}$  [31], and  $9 \times 10^{-11}$  to  $4 \times 10^{-10} \text{ cm}^2/\text{s}$  [17], suggesting that the upper bound  $da/dt_{II}$  is 20 to 160 nm/s. This is a very slow rate, expected for fcc alloys, and demonstrates the experimental challenge in measuring HEAC. Recent research on H uptake and trap-sensitive H diffusion in Monel K-500 established the applied potential dependence of crack tip diffusible H concentration,  $C_{H-Diff}$ , necessary to test the models represented in Eqns. 1 through 3 [17].

The very slow crack growth rates expected for Monel K-500, and dependence on level of applied cathodic polarization, provide an ideal system for application of a fracture mechanics based crack growth rate approach to component life prediction [44-46]. To date, control of EAC focused on alloy selection and design to not exceed a threshold stress or stress intensity factor in service (for example [28]). This approach may be overly conservative for Monel K-500 in seawater. The present work examines use of a probabilistic component prognosis program, *SCCrack* [47], to simulate the EAC propagation life of a threaded bolt and laboratory test specimen of Monel K-500 [11].

The objectives of this research are to: (1) quantitatively characterize the HEAC kinetics of aged Monel K-500 relevant to aqueous chloride exposure and cathodic polarization, and enhance an existing-accelerated test method [40,47] (2) measure and scale the crack tip uptake of H, versus applied potential, (3) model the applied potential

dependence of threshold stress intensity and  $da/dt_{II}$  based on crack tip H uptake and process zone embrittlement mechanisms, and (4) employ accelerated-laboratory test results to probabilistically simulate the HEAC behavior of a component in marine service. Precracked specimens are loaded under slow-rising displacement, crack growth is monitored by a high precision direct current potential difference (dcPD) method, and the crack tip driving force is defined by a quantitative elastic-plastic J-integral analysis which has typically not been utilized to characterize EAC [38,48-51]. Measured crack growth kinetics are used to validate two micromechanical models of HEAC and as input for *SCCrack* simulations. Crack tip electrochemistry and H results, as well as crack growth rate vs applied stress intensity from the J-integral, are presented in this final report. Mechanism-based and component scale modeling are ongoing.

## EXPERIMENTAL PROCEDURE

### Material and Specimen Design

Hot finished and aged bar (15.9 mm diameter) of Monel K-500 (UNS05500) was purchased from ATI Allvac with vendor reported chemical composition in Table 1 and mechanical properties in Table 2. These properties were developed by solution treatment then age hardening (ST-A); 16 h at 593°C, cool at 14°C/n to 482°C, air cool to ambient temperature. This heat treatment was reported to result in coherent-spherical  $Ni_3Al$  precipitate ( $\gamma'$  phase of order 5 nm radius, 8-10 volume percent, and possibly with dissolved Ti, Cu, Si or Mn) strengthened Ni-Cu solid solution austenite (face-centered cubic  $\gamma$  phase) [52]. Ramberg-Osgood flow rule constants [53] were established for Monel K-500:  $\alpha = 0.53$ ,  $n = 11.5$ ,  $E = 183,900$  MPa, and  $\sigma_0 = \sigma_{YS}$ .

**Table 1. Chemical Composition of Monel K-500 (Weight Percent)**

Ni	Cu	Fe	C	Mn	Al	Ti	P	S
66.12	28.57	0.80	0.166	0.81	2.89	0.45	.015	.0005

Si = 0.08, Cr = 0.04, Zr = 0.03, Nb, Ta, W, V < 0.01, Bi, Pb, Ag, Sn < 0.0005 wt pct

<b>Table 2. Mechanical Properties of Monel K-500 (ST-A)</b>					
HRC	$\sigma_{YS}$ (MPa)	$\sigma_{UTS}$ (MPa)	Reduction in Area (pct)	E (GPa)	$K_{IC}$ (MPa $\sqrt{m}$ )
31	773	1,169	49.7	184 [54]	198 to 340 [28,38,55]

Small single edge micronotch tensile (SENT) specimens were machined with a width ( $W$ ) of 10.7 mm and thickness ( $B$ ) of 2.54 mm. The Mode I loading axis was parallel to longitudinal direction ( $L$ ) of the rod with crack growth in the radial ( $R$ ) direction. The notch was wire electrospark discharge machined to a depth of  $200 \pm 10 \mu\text{m}$  and mouth opening of  $235 \pm 20 \mu\text{m}$ . The SENT specimen was fatigue precracked to a total notch plus crack depth ( $a_0$ ) of 850-1,150  $\mu\text{m}$  in moist air with maximum-elastic stress intensity factor ( $K$ ) decreasing from 18 MPa $\sqrt{m}$  to 13 MPa $\sqrt{m}$  at constant stress ratio of 0.10.

#### Crack Length Measurement

The direct current electrical potential difference (dcPD) method was used to measure crack length [56]. A constant  $4.000 \pm 0.005$  A direct current was applied to the specimen grips. Platinum wires were spot welded just outside and above/below the notch edges across the specimen thickness to measure potential difference that was input to a 10,000-gain direct current amplifier. Voltage measurements were unaffected by electrochemical polarization, and vice-versa, because conflicting ground levels were avoided. The resolution in measured potential was 0.1  $\mu\text{V}$ , which corresponded to a resolvable average crack extension,  $\Delta a$ , of 0.5  $\mu\text{m}$ . A reference probe pair was located well away from the crack to measure and eliminate potential changes in the broad-gauge volume caused by temperature, elastic strain, and plasticity dependent resistance changes [57]. Crack length was recorded every 2 to 5 minutes. For every dcPD data point recorded, 50 measurements were averaged over 1 s, the current polarity was reversed and amplifier output stabilized for 0.5 s, and 50 readings were taken over 1 s. Thermal voltage contribution was eliminated by averaging the positive and negative

polarity signals. This process was repeated 20 to 50 times for the active and reference probes, with the total time required equaling 60 s to 150 s. The recorded potential was the overall average of these multiple readings. Each dcPD value was converted to crack length ( $a$ ) by Johnson's equation using the measured potential associated with the notch depth to determine the adjustable constant,  $V_o$ , in this equation [58]. All crack lengths from dcPD were corrected linearly using the final optically measured crack length which was averaged at 5 locations across the crack front. Typically, predicted and measured crack lengths differed by less than 5% prior to this linear correction.

To calculate crack growth rate at a given time ( $t$ ), a 2<sup>nd</sup> order polynomial was fit to  $a$  vs  $t$  data over  $t \pm 7$  data points. The slope of the tangent at the mid-time point was  $da/dt$  and this process was repeated to obtain  $da/dt$  at every value of  $a$ . The secant method was used to determine  $da/dt$  for the first 3 and last 3 values of crack length versus time. In this analysis,  $da/dt$  data were recorded for crack advance increments which exceeded 5  $\mu\text{m}$  and for time intervals which were up to 50,000 s. Depending on levels of  $da/dt$  for a given applied potential, these intervals were adjusted to provide an optimal balance between data density and growth rate variability.

High resolution measurement of  $da/dt$  was challenged by three issues unique to this alloy strength level and environment. These included large scale ligament plasticity, which could compromise the elastic-K analysis and contribute to dcPD increase due to plasticity-based resistivity increase. Additionally, crack surface electrical contact which changes during crack opening may provide a false growth rate. These issues and data analysis enhancements are considered in the Results section.

#### Fracture Mechanics Analysis

Crack growth rate data were analyzed using elastic stress intensity ( $K$ ) and total stress intensity ( $K_J$ ), which includes the effect of specimen plasticity using the J-integral analysis. The clevis-based gripping configuration allowed free rotation of the SENT specimen about the loading pins to comply with the boundary condition for the elastic-K-solution [59].  $K_J$  was determined using analytical solutions for a stationary crack in a material which deforms according to the Ramberg-Osgood flow rule: [53]

$$K_J = \sqrt{(J_{Elastic} + J_{Plastic})E'} = \sqrt{\left(\frac{K^2}{E'} + J_{Plastic}\right)E'} \quad (4)$$

where  $E' = E$  for plane stress and  $E/(1-\nu^2)$  for plane strain, with  $\nu$  as Poisson's ratio. In this formulation of  $K_J$ ,  $K$  is based on effective crack length defined as the physical crack length plus plastic zone radius,  $r_p$ , given by the standard plane strain estimate: [53]

$$r_p = \frac{1}{3\pi} \left(\frac{K}{\sigma_{YS}}\right)^2 \quad (5)$$

Considering the plastic contribution to the J-integral: [60]

$$J_{Plastic} = \frac{\alpha \sigma_o^2}{E} a \frac{(W-a)}{W} h_1(n, a/W) \left(\frac{P}{P_o}\right)^{n+1} \quad (6)$$

where  $\alpha$ ,  $\sigma_o$ ,  $E$ , and  $n$  are constants from the Ramberg-Osgood equation,  $E$  is  $\sigma_o/\epsilon_o$ ,  $a$  is crack length,  $W$  is SENT width,  $P$  is applied load, and  $P_o$  is the plastic limit load given by: [53]

$$P_o = \beta \left( \sqrt{1 + \left(\frac{a}{W-a}\right)^2} - \left(\frac{a}{W-a}\right) \right) (W-a)B\sigma_o \quad (7)$$

where  $B$  is thickness and  $\beta$  is a constant which equals 1.0 for plane stress and 1.455 for plane strain. The  $h_1$  is specific to the cracked geometry and given by a tabulated function of  $a/W$ ,  $n$ , and stress state. For the rotating SENT specimen and  $n$  of 11.8 for Monel K-500, this function was specified by fitting a fourth-order polynomial [53,60]. The stress state dependent terms in Eqns. 4 to 6 were assumed to be plane strain values, justified by three-dimensional finite element analyses [61,62] and the appearance of all EAC surfaces for the Monel K-500 examined.

#### Electrochemical Control and Loading Conditions

The precracked specimen was loaded in a 340 ml cylindrical Plexiglas cell containing non-deaerated 0.6 M (3.5 wt pct) NaCl circulated from a 4 liter reservoir at 20 ml/min and room temperature. Solution was not buffered and periodic measurements

confirmed a constant bulk pH of 6.5 to 7.5 for the experiment duration. Only the cracked section of the specimen was exposed to solution, precluding galvanic coupling with the grips. The specimen was the working electrode grounded through the testing machine, while the potentiostat was operated in floating mode to avoid a ground loop. Experiments were run in potentiostatic control with applied potentials ranging from -1.1 to -0.7 V<sub>SCE</sub>, compared to an open circuit potential of -200 to -250 mV<sub>SCE</sub> [28]. The counter electrode was platinum coated Nb mesh surrounding the specimen in the cell and the reference electrode was located in the fatigue cell. After immersion in NaCl solution, the specimen was cyclically loaded at 1 Hz and the final air-precrack stress intensity condition for 500 to 1000 cycles to assure that the environment penetrated the fatigue crack tip.

The precracked SENT specimen was loaded in a servo-hydraulic feedback controlled tensile machine under slow actuator displacement rate. This displacement rate was computer controlled and varied in real time to provide a constant rate of K increase, dK/dt, during crack growth. This loading protocol was programmed to optimize test time: dK/dt = 6 MPa√m/h for elastic K up to 5.5 MPa√m where SCC is improbable, dK/dt = 0.3 MPa√m/h for K from 5.5 to 44 MPa√m, and dK/dt = ~1 MPa√m/h for K above 45 MPa√m. These rates were selected based on experience with HEAC in steel [40] and a nickel superalloy (IN718 [14]) of widely varying D<sub>H</sub>, but the effect of dK/dt was not measured for Monel K-500 in chloride. Load, actuator displacement, time, crack length, and K were automatically recorded.

#### Occluded Crevice Electrochemistry

Modeling of HEAC, using Eqns. 1-3, requires determination of C<sub>H-Diff</sub> as a function of crack tip H overpotential ( $\eta_H$ ), which directly follows from knowledge of crack tip pH and potential as well as a microstructure-specific H uptake relationship; all versus applied potential. Crack tip pH and potential were measured for Monel K-500 using the artificial crevice geometry shown in Fig. 1, coupled with the scaling-law approach to relate crevice and crack geometry difference [63]. The cell consisted of three parts: an acrylic bottom plate in which 6 disk-shaped specimens were embedded and shorted to form a continuous working electrode, a plastic shim to create the crevice gap (G) of 1 mm, and an acrylic top plate which forms the crevice and holds the micro reference



electrodes (REs) for local potential measurement. Vacuum grease was used to maintain a tight seal on the crevice components. The Monel K-500 specimens (surface area  $\sim 3 \text{ cm}^2$ ) were polished to a 600-grit finish, degreased with ethanol and mounted in the bottom acrylic plate. The specimens are at a distances (x) of 1, 3, 5, 7, and 9 cm from the crevice opening to create values of  $x^2/G = 10, 90, 250, 490$  and  $810 \text{ cm}$ . Local potential was measured using a Ag/AgCl micro-reference electrode prepared by the procedure reported elsewhere [64] and calibrated versus the saturated calomel electrode (SCE). Local pH was measured using pH indicator paper as shown in Fig. 1. The electrolyte in all experiments was 0.6 M NaCl (bulk pH = 6 to 7) and the cell was open to air.

The H uptake relationship,  $C_{\text{H-Diff}}$  versus  $E_{\text{applied}}$ , was determined using either thermal desorption spectroscopy (TDS) or barnacle cell (BC) methods applied to planar electrodes of Monel K-500 which were H precharged for 10 days in 0.6M NaOH maintained at pH 8 with NaOH addition. It is assumed that H uptake in the Monel K-500 crack is relatively insensitive to local pH, at constant  $\eta_{\text{H}}$  for the expected pH levels above 6. This experimental approach is detailed elsewhere [17].

## RESULTS

### Crack Tip Chemistry and Hydrogen Uptake

Crack tip conditions which govern uptake of H were measured for Monel K-500. It is assumed that crack potential and pH are not affected by heat-to-heat differences in ST-A Monel K-500. As such, a lot of Monel K-500 was investigated which was used in a prior-extensive study of H uptake.<sup>1</sup> Figure 2 shows local potential measured at different distances into the crevice from the mouth (x, for  $G = 1 \text{ mm}$ ) at different applied potentials of -0.6, -0.7, -0.8, -0.9 and -1.0  $V_{\text{SCE}}$ . Potential is plotted versus  $x^2/G$  since this parameter correlates artificial crevice and crack chemistry conditions [63]. In all experiments a potential gradient inside the crevice was established after the external potential was applied. This local potential increased as the distance from the crevice

<sup>1</sup> Special Metals; Ni-30.2Cu-1.66Fe-0.17C-0.58Mn-2.69Al-0.61Ti-0.007P-<10 ppm S (by weight pct);  $\sigma_{\text{YS}} = 783 \text{ MPa}$ ,  $\sigma_{\text{UTS}} = 1146 \text{ MPa}$ , RA = 48%, aged at 593°C (16 h), 538°C (6 h), 482°C (8 h), air cooled.



opening increased and the potential gradient decreased with time. No significant pH difference was observed as a function of  $x^2/G$  inside the crevice. However, pH increased with decreasing-applied potential at 300 s exposure,<sup>2</sup> and with increasing exposure time.

The distribution of hydrogen overpotential inside the crevice was calculated from local pH and potential (Fig. 2), and results are shown in Fig. 3 as a function of applied potential after 300 s and 10 h exposures. At  $E_{\text{applied}}$  of -0.6 and -0.7  $V_{\text{SCE}}$ ,  $\eta_{\text{H}}$  was positive which suggests that H was not generated. At more negative potentials such as -0.8 and -0.9  $V_{\text{SCE}}$ ,  $\eta_{\text{H}}$  was negative at 300 s but increased to positive for longer time (10 h). At -1.0  $V_{\text{SCE}}$ ,  $\eta_{\text{H}}$  was always negative, indicating H was generated at all times. However, the overpotential became less negative with increasing distance from the crevice opening and with time.

The subsurface diffusible H concentration,  $C_{\text{H-Diff}}$ , at each position within the artificial crevice was calculated from position-dependent  $\eta_{\text{H}}$  in Fig. 3. Planar electrodes of the ATI-Allvac lot of Monel K-500 (Table 1) were immersed for 10 days in 0.6 M NaCl (pH 8) solution at various  $E_{\text{applied}}$  to introduce H to this microstructure. Total H content from both melt extraction (LECO) and LECO calibrated TDS was measured along with  $C_{\text{H-diff}}$  from TDS and the BC methods, each versus applied potential. The results are shown in Fig. 4, with the most reasonable H diffusivity for the BC data analysis being  $1.3 \times 10^{-10} \text{ cm}^2/\text{s}$  for ST-A Monel K-500 at 23°C [17]. The TDS and BC methods yielded different H-uptake relationships, as also observed for a different lot of Monel K-500 [17]. Regression through the TDS-based bold surface  $C_{\text{H-Diff}}$  versus  $E_{\text{applied}}$  data in Fig. 4 ( $\square$ ), converted to  $\eta_{\text{H}}$  for bulk solution pH 8, yielded:

$$C_{\text{H-Diff}} (\text{wppm}) = -3.37 - 0.085 \eta_{\text{H}} (\text{mV})^3 \quad (8)$$

<sup>2</sup> Crevice measurements (Fig. 1) showed this association: crevice pH 10 at -1000  $\text{mV}_{\text{SCE}}$ , pH 8 at -900  $\text{mV}_{\text{SCE}}$ , pH 8 at -800  $\text{mV}_{\text{SCE}}$ , pH 7.5 at -700  $\text{mV}_{\text{SCE}}$ , and pH 7 at -600  $\text{mV}_{\text{SCE}}$ . Each crevice pH was independent of  $x^2/G$  and measured after 300 s exposure.

<sup>3</sup> A similar trend was measured for the lot of Monel K-500 represented in Footnote 1 and Figs. 2-4, and exposed in the 0.6M (pH 8) NaCl solution:

$$C_{\text{H-Diff}} (\text{wppm}) = -6.97 - 0.196 \eta_{\text{H}} (\text{mV})$$

Notably, the concentration of diffusible H was substantially higher in this lot of Monel K-500 compared to the ATI-Allvac lot represented by Eq. 8 and used in the current study of HEAC.

Eqn. 8 was used with measured  $\eta_H$  (300 s immersion, Fig. 3) to predict  $C_{H-Diff}$  at various  $x^2/G$  within the crevice and as a function of bold-surface applied potential, Fig. 5. Eqn. 8 was assumed to describe crack surface H uptake for all locations and  $E_{applied}$  levels. Hydrogen uptake on the free surface ( $x^2/G = 0$  cm) was computed using pH 6 in the calculation of  $\eta_H$ .

A typical crack in Monel K-500 (Tables 1 and 2) grows from a depth (x) of about 1.3 mm at a K of 20 MPa $\sqrt{m}$  to a depth of 3 mm at 40 MPa $\sqrt{m}$ . The opening displacement (gap, G) is approximated by the average of the elastic crack tip and crack mouth opening displacements, which varies from 6 to 33  $\mu m$  for this crack extension interval and typical K increase. The associated value of  $x^2/G$  is between 20 and 29 cm. This is an approximation of a more complex crack shape and variation between cracking experiments. The dotted line in Fig. 5 reasonably describes crack tip  $C_{H-Diff}$  versus applied potential for Monel K-500 (ST-A, ATI-Allvac) with  $x^2/G$  of 20 to 30 cm; the equation is:

$$C_{H-Diff} \text{ (wppm)} = -52.5 - 68.7 E_{applied} (V_{SCE}) \quad (9)$$

At this constant  $x^2/G$ ,  $C_{H,diff}$  decreased with increasing  $E_{applied}$  and reached 0 at -764 mV $_{SCE}$  (Fig. 5). This behavior results from the dependence of  $\eta_H$  on potential and pH inside the crack. Clearly, H is introduced at the Monel K-500 crack tip, for a range of cathodic polarizations; the effect of H uptake on cracking is reported in the next section.

#### HEAC under Severe Cathodic Polarization

Solution treated and aged Monel K-500 is susceptible to severe intergranular HEAC when stressed under slow-rising K during immersion in NaCl solution at a constant-cathodic potential of -1000 mV $_{SCE}$ . Figure 6 shows the results of replicate experiments, plotted as da/dt versus elastic K at constant dK/dt  $\sim 0.3$  MPa $\sqrt{m}/h$  for K from 6 to 44 MPa $\sqrt{m}$  and dK/dt =  $\sim 1$  MPa $\sqrt{m}/h$  for K above 44 MPa $\sqrt{m}$ . Figure 6a shows da/dt values computed for a very small increment of crack advance ( $\Delta a = 5 \mu m$ ), which produces a high data density, but local variation in da/dt. Figure 6b shows one of these

experiments where the dcPD data were analyzed using a larger  $\Delta a$  (25  $\mu\text{m}$ ) to reduce the variability of  $da/dt$ . Reproducibility is excellent and the  $da/dt$  vs  $K$  relationship conforms to the typical kinetics of environmental cracking by the HEAC mechanism [13]. Each replicate specimen exhibits a threshold stress intensity for the onset of resolvable subcritical crack growth under slow-rising  $K$  ( $K_{TH}$ ), followed by steeply rising  $da/dt$  with increasing  $K$ , and transitioning to the beginning of a  $K$ -independent (Stage II) crack growth rate regime above about  $4 \times 10^{-5}$  mm/s. The programmed increase of the controlled  $dK/dt$  at  $K = 44 \text{ MPa}\sqrt{\text{m}}$  did not resolvably affect  $da/dt$  (e.g., Figure 6b), as expected for Stage II subcritical crack growth at this relatively high rate. The  $K_{TH}$  is resolved at  $da/dt$  above  $3 \times 10^{-7}$  mm/sec, equaling  $K$  levels of  $14.9 \text{ MPa}\sqrt{\text{m}}$  and  $20.1 \text{ MPa}\sqrt{\text{m}}$  for these two experiments, based on the low-data density plots and after correction to eliminate the impact of the initial-artifact decline in  $da/dt$  with rising  $K$  as described in an ensuing section. These low values of  $K_{TH}$  are compared to a plane strain fracture toughness for this alloy which is in the range of 198 to  $340 \text{ MPa}\sqrt{\text{m}}$  [38,55].

The HEAC path was fully intergranular for the test conditions represented in Fig. 6, as established by the scanning electron microscopy (SEM) fractographs in Fig. 7. The low magnification image (Fig. 7a) shows the outlined moist air fatigue precrack front transition to intergranular cracking. (Fatigue in this alloy likely involves a combination of highly faceted  $\{111\}$  slip band cracking, plus intergranular cracking, for the low  $K$  levels employed in precracking [65]. The resulting features are somewhat similar, but none-the-less distinct from the intergranular crack path typical of HEAC.) The transition from fatigue precrack to H crack is outlined in Fig. 7a and was consistently observed during SEM analyses of all specimens. The low magnification fractograph is compared to an SEM image of the Monel K-500 microstructure, at the same magnification in Fig. 7b, showing the good correspondence between grain size and intergranular crack surface facet size. A higher magnification image of the transition from IG/TG fatigue to TG HEAC is shown in Figure 7c. The high magnification images in Figs. 7d and 7e suggest that grain surfaces are populated by slip trace steps, as reported for IHAC of Ni [21]. Also, note the occasional intersecting twins and small-infrequent particles which are relatively large TiC and sulfide inclusions (rich in Mg, Mn, Al, Ti and Fe based on energy dispersive analysis) [17].

### Effect of Applied Potential on HEAC

The severity of HEAC in Monel K-500 increased with increasing cathodic polarization, between  $-700 \text{ mV}_{\text{SCE}}$  and  $-1100 \text{ mV}_{\text{SCE}}$ , as shown by  $da/dt$  vs  $K$  in Fig. 8. Polarization current was sensibly constant during slow-rate loading at fixed potential and was always cathodic. Initial declines in  $da/dt$  with rising  $K$  at levels below about  $10 \text{ MPa}\sqrt{\text{m}}$  (see Fig. 6) were observed for each potential and deleted for clarity. Two important trends are apparent in Fig. 8. First, the  $K_{\text{TH}}$  increases as potential increases from  $-1100 \text{ mV}_{\text{SCE}}$  to  $-700 \text{ mV}_{\text{SCE}}$ . Second, crack growth rates in the vicinity of a possible  $K$ -independent Stage II plateau decrease with increasing potential over this same range. The vertical line drawn at  $K = 43.9 \text{ MPa}\sqrt{\text{m}}$  notes the point in the loading protocol where the constant-applied  $dK/dt$  was increased from  $0.3$  to  $1.1 \text{ MPa}\sqrt{\text{m/h}}$ . When stable crack growth is driven by rising  $K$ , as in a crack growth resistance fracture experiment,  $da/dt$  is often directly proportional to applied  $dK/dt$ . The shaded-vertical band in Fig. 8 shows a near-instantaneous 3.3-times increase in  $da/dt$  which is directly proportional to the 3.3-times increase in applied  $dK/dt$  and establishes that this loading rate rise produced a proportionate increase in  $da/dt$ . This increase in  $dK/dt$  had a similar effect on  $da/dt$  at higher potentials of  $-800$ ,  $-750$  and  $-700 \text{ mV}_{\text{SCE}}$ , less so for loading at  $-900$  and  $-1000 \text{ mV}_{\text{SCE}}$ , the increase was not resolved for  $-1100 \text{ mV}_{\text{SCE}}$ . The shaded horizontal band represents the resolution limit of the dcPD-based determination of  $da/dt$ , limited by crack tip plasticity as outlined in an ensuing section.  $K_{\text{TH}}$  is operationally defined as the stress intensity level necessary to produce a crack growth rate equal to this resolution limit for the loading rate of interest ( $dK/dt = 0.3 \text{ MPa}\sqrt{\text{m/h}}$  for Monel K-500 in the present study). The results in Fig. 8 are summarized in Table 3. This tabulation includes data obtained by the present test method applied to a second lot of ST-A Monel K-500 with similar chemical composition and mechanical properties [14].<sup>1</sup> The J-integral based values of  $K_{\text{TH}}$  are presented in an ensuing section.

For potentials between  $-1100 \text{ mV}_{\text{SCE}}$  and  $-800 \text{ mV}_{\text{SCE}}$ , HEAC was regular in macroscopic shape and substantially intergranular. However, the crack shape was localized to the specimen center for loading at  $-750 \text{ mV}_{\text{SCE}}$  and HEAC was not

macroscopically apparent for the -700 mV<sub>SCE</sub> case. Intergranular crack growth was not resolved by SEM analysis of the specimens loaded at -750 and -700 mV<sub>SCE</sub>.

**Table 3. HEAC Growth Rate Properties for Monel K-500 (ST-A)**

	K <sub>TH</sub> (elastic) at 4 x 10 <sup>-7</sup> mm/s MPa√m	K <sub>TH</sub> (J-integral) MPa√m	da/dt from dcPD at elastic K = 50 MPa√m mm/s
-1100 mV <sub>SCE</sub>	18	18	1.7 x 10 <sup>-4</sup>
-1000	23	23	2.3 x 10 <sup>-5</sup>
-1000	18	18	1.9 x 10 <sup>-5</sup>
-934 (2010)	~30	~32	1.6 x 10 <sup>-5</sup>
-900	22	22	1.1 x 10 <sup>-5</sup>
-800	42	44	3 x 10 <sup>-6</sup>
-750	> 68	> 90	IG not resolved by SEM
-700	> 63	> 77	IG not resolved by SEM
-700 (2010)	> 63	> 77	IG not resolved by SEM

These results are supported by the images in Figs. 9 through 11. The optical micrographs in Fig. 9 depict, from left to right in each image: (a) the EDM notch, (b) the fatigue precrack, which is irregular for the specimen stressed at -1100 mV<sub>SCE</sub>, varying from 0.54 on the top edge to 1.60 mm on the lower edge, with a 5- point average depth of 1.09 mm, with similar irregularity seen for the -900 and -750 mV<sub>SCE</sub> cases, (c) HEAC, with the extent indicated by the horizontal arrow, and (d) post-HEAC fatigue in moist air after removal from the cell and cleaning in distilled water. While da/dt from dcPD is suggested to be finite for the experiment conducted at -700 mV<sub>SCE</sub> (Fig. 8), low magnification optical microscopy did not show a resolvable region of HEAC (Fig. 9). While da/dt from dcPD is similar for the two experiments conducted at -750 and -800 mV<sub>SCE</sub> (Fig. 8), the low magnification images in Fig. 9 suggest a different shape and perhaps microscopic morphology of HEAC.

High magnification SEM analysis confirmed that intergranular HEAC did not occur in the Monel K-500 specimens stressed in pure NaCl at either -700 or -750 mV<sub>SCE</sub>. For the -700 mV<sub>SCE</sub> case, the fractograph in Fig. 10a shows the fatigue precrack in the top-third of the image, a 75 μm wide zone (middle), and post-HEAC fatigue in the bottom



third of the image. Intergranular crack extension is not resolved, even for slow rate loading (Fig. 10b), strongly suggesting with lack of HEAC. A stretch zone could form due to crack tip blunting plasticity and the size is estimated to equal  $20\text{ }\mu\text{m}$  for Monel K-500 and the K level applied at the end of the HEAC experiment.<sup>4</sup> The physically larger zone in Fig. 10a suggests crack tip blunting-extension by slip augmented by microvoid damage which is not expected, at least for rapid rate loading, at the K levels investigated in this study. The experiment conducted at  $-750\text{ mV}_{\text{SCE}}$  shows a larger zone of apparent subcritical crack growth localized to the central portion of the specimen and about  $450\text{ }\mu\text{m}$  deep, as seen in Fig. 9 (left column, lowest image) and amplified in Fig. 11a. Figure 11b shows that this cracking is wholly by microvoid-based processes and is not IG.

The results in Figs. 10 and 11 establish that polarization to  $-700$  and  $-750\text{ mV}_{\text{SCE}}$  eliminated HEAC in Monel K-500 for the slow loading rate investigated. Crack growth ahead of the fatigue precrack was by microvoid nucleation, growth and coalescence which is not likely due to a contribution from H. Since the plane strain fracture toughness for Monel K-500 (ST-A) was reported to equal  $198\text{ MPa}\sqrt{\text{m}}$  and  $223\text{ MPa}\sqrt{\text{m}}$  for air melted and electroslag-remelted heats of Monel K-500, respectively [38], and perhaps as high as  $340\text{ MPa}\sqrt{\text{m}}$  [28,55], the appearance of microvoids in Figures 10b and 11b is unexpected since the stress intensity levels applied to these specimens were about  $90\text{ MPa}\sqrt{\text{m}}$  based on the J-integral analysis put forth in an ensuing section. Speculatively, the stable crack growth shown in Figs. 10 and 11 could be ascribed to the interaction of very load-rising K loading interacting with carbide particles; essentially, a form of ambient temperature creep crack growth. Critically, for the present study, the  $da/dt$  vs K values shown in Fig. 8 for  $-700$  and  $-750\text{ mV}_{\text{SCE}}$  are not due to IG HEAC and thus should not be considered in modeling of this failure mechanism.

#### Effect of Loading Protocol on HEAC

Loading protocol impacts HEAC growth in Monel K-500 (ST-A), predominantly at higher potentials where resistance to IGSCC is high and  $da/dt$  levels are low. An

<sup>4</sup> Crack tip opening displacement, CTOD, is estimated to equal  $d_n K^2(1-\nu^2)/(\sigma_{YS} E)$  [53], where the stress state and hardening dependent coefficient,  $d_n$ , = 0.69 for the average of plane stress and plane strain and Ramberg-Osgood flow properties for ST-A Monel K-500. Elastic K at the end of the HEAC loading,  $55\text{ MPa}\sqrt{\text{m}}$ , was increased to  $K_I = 95\text{ MPa}\sqrt{\text{m}}$  using the J-integral approach.

example is shown in Fig. 12 where the continuously-slow-rising K experiment at  $-800 \text{ mV}_{\text{SCE}}$  is compared to a rising-step-K format ( $2.6 \text{ MPa}\sqrt{\text{m}}$  K step at  $dK/dt = 7.2 \text{ MPa}\sqrt{\text{m/h}}$  followed by a 6 h hold period at each fixed K). Intergranular HEAC was produced during rising K for this applied potential of  $-800 \text{ mV}_{\text{SCE}}$ , but during step-hold loading. This conclusion is supported by optical microscopy (Fig. 12a), where slow crack growth is  $0.25 \text{ mm}$  for the step case and  $0.58 \text{ mm}$  for the continuous-K case, and where the step-loading cracking is centrally localized akin to the HEAC-immune result for continuous loading at  $-750 \text{ mV}_{\text{SCE}}$  (Fig. 11). The effect of loading format is also shown by the dcPD measured a vs time data (Fig. 12b), where crack growth from measured voltage is  $0.32 \text{ mm}$  for the step case and  $0.51 \text{ mm}$  for the continuous-K case, with each occurring after initial rise to  $a = 0.70 \text{ mm}$ , which is false crack extension, as amplified in an ensuing section. Finally, the effect of loading format is shown by the crack growth rate data in Fig. 12c, where  $da/dt$  was computed for the hold period for the step case. From Fig. 12b, the majority of resolvable HEAC growth occurred during the rising part of the step-hold sequence and the dcPD measured change during the hold was nil to very small up to the highest K levels examined (Fig. 12c).

The strong effect of loading format was confirmed by the SEM fractographic findings contained in Fig. 13. In Fig. 13a, crack growth during continuous-slow-rising K was by IG HEAC along the arrow, with the fatigue precrack front at the right of the image. Such IG HEAC was uniform throughout the thickness (vertical direction in Fig. 13a) of the SENT specimen, as suggested by the optical micrograph for the continuous-rising K loading (Fig. 12). This surface contained a fraction of transgranular cracking features which are amplified at higher magnifications in Figs. 13b and 13c. These features were not seen for continuous-slow-rising K loading at lower potentials and are suggestive of H interaction with slip to produce faceted surfaces possibly parallel to intersecting slip planes. Perhaps this occurrence of transgranular cracking is related to the lower H content produced at the crack tip for this higher potential, as developed in an ensuing section.

In contrast crack growth during the step-hold sequence was localized ahead of the fatigue precrack at the SENT specimen mid-plane (Fig. 12) and in the direction of the arrow in Fig. 13d. This growth appearance at low magnification is similar to that



observed for the slow-continuous-K loading at -750 and -700 mV<sub>SCE</sub> where these potentials did not support IG HEAC. Critically, the step-hold crack morphology (Fig. 13e) suggests that IG HEAC did not occur during this loading sequence, while such IG HEAC was produced by continuous-slow-rising K (Fig. 13b). The microscopic morphology shown at higher magnification in Fig. 13e has some characteristics of microvoid damage which is interspersed with sheared regions that were not typically observed in other specimens. This point is clearly illustrated by comparison between Figs. 13e and 13f, with the latter SEM image showing classic microvoid damage produced by final separation of this SENT specimen after post-HEAC fatigue cracking to final separation in air. This microvoid-like fracture zone was likely only formed during the relatively rapid rising K section of the step-hold, from the dcPD data. The occurrence of microvoids at such low K levels is unexpected, as previously discussed. Moreover, the detailed appearance of this surface is not that of classic microvoids when viewed at higher magnification. The details of this crack surface, as well as the occurrence of microvoid based damage at stress intensity levels less than 100 MPa√m in a high toughness alloy, are under investigation. The key point is that IG HEAC was produced during slow-rising K loading, but not during the step-hold format, when Monel K-500 was exposed in NaCl at a fixed cathodic polarization of -800 mV<sub>SCE</sub>.

Both slow rising and step-hold stress intensity programs yielded the same rates of HEAC in SH-T Monel K-500 when the specimens were stressed at -934 mV<sub>SCE</sub>, which favored intrinsically higher rates of subcritical cracking. The data supporting this conclusion are presented in Fig. 14 for the lot of ST-A Monel K-500 described in Footnote 2, where da/dt was computed during the hold period of the step protocol.

#### Experimental Method Issues

Two aspects of the dcPD-based crack length data obtained for Monel K-500 in NaCl reveal complicating factors which differ from the HEAC response of ultra-high strength martensitic steel, which was characterized by the same experimental approach [40]. First, for Monel K-500 da/dt declines with increasing K in the low K regime for each applied-cathodic potential which was examined. A typical example is shown in Figs. 6 and 14 for the replicate -1000 mV<sub>SCE</sub> experiments, and in Fig. 15a for ST-A Monel K-500

at  $-700 \text{ mV}_{\text{SCE}}$ . This behavior is not real-decelerating IGSCC at low  $K$ , but rather represents increasing dcPD signal as the crack opens with increasing  $K$  to reduce crack-wake electrical contact [56]. This increase in voltage, at declining rate with crack opening, is reasonable for Monel K-500 in NaCl because: (a) cathodic polarization likely reduced the fatigue crack surface oxide that would otherwise provide electrical insulation, and (b) the fatigue crack was microscopically rough due to slip band and intergranular cracking to promote asperity contact during crack opening (see Figs. 7a and 7c). This electrical shorting effect was directly observed; the dcPD value continuously declined as solution was first added to the environmental cell prior to rising- $K$  loading. Considering Fig. 15b, the physically real fatigue crack length of 1.15 mm (horizontal line at 0.045 inches) decreased to 0.66 mm (0.026 inches) upon solution introduction at very low load and near 0 time. Obviously, such crack length shrinkage is not physically possible. Moreover, during rising  $K$ , the apparent crack length increased to recover to the 1.15 mm length (horizontal line) after loading for about 230,000 s. IGSCC is unlikely during such low  $K$  loading, in general, and IGSCC was in fact never produced for loading at  $-700 \text{ mV}_{\text{SCE}}$ .

There are several approaches to eliminate this spurious effect of crack surface electrical contact on  $da/dt$ . In this study falling log  $da/dt$  was fit as a linear function of log  $K$  and subtracted from the measured  $da/dt$  to produce growth rates only due to HEAC. This correction is illustrated in Figs. 6b and 15a. The alternate approach is to assume a point on the crack length vs time plot (e.g., ♦ in Fig. 15b) where electrical contact along the crack surfaces is effectively eliminated by opening and the dcPD crack length is equated to that established by fatigue precracking. This voltage is used with the fatigue precrack length in the Johnson equation calibration of dcPD. Each approach is judged to yield the same-correct set of  $da/dt$  versus  $K$  data.

Figure 15b illustrates a second complicating issue associated with dcPD characterization of HEAC beyond shorting contact. For this specimen stressed in NaCl at  $-700 \text{ mV}_{\text{SCE}}$ , crack length first rises linearly for an apparent length increase of  $75 \text{ } \mu\text{m}$  between 230,000 s and 430,000 s (effective  $da/dt \sim 4 \times 10^{-7} \text{ mm/s}$ ), then at an elastic  $K$  of  $45 \text{ MPa}\sqrt{\text{m}}$  (430,000 s)  $da/dt$  accelerates proportionate to the enforced increase in applied  $dK/dt$  to produce an additional  $190 \text{ } \mu\text{m}$  of apparent growth as  $K$  continues to

increase (effective  $da/dt \sim 4 \times 10^{-6}$  mm/s at  $dK/dt$  of  $1.1 \text{ MPa}\sqrt{\text{m/h}}$ ). This total crack extension of  $260 \mu\text{m}$  is not real. The SEM result in Fig. 10a shows a  $75 \mu\text{m}$  zone of plasticity-stretch and microvoid damage, but no intergranular crack extension, ahead of the fatigue crack tip. The dcPD measurement over-predicts this SEM-measured zone by  $190 \mu\text{m}$ . The reference probe was used in the present experiments in order to eliminate the effect of increased current density on dcPD, traced to reduced SENT specimen cross-sectional area due to Poisson contraction, as well as due to increased Monel resistivity due to strain. The false-extra amount of crack growth,  $190 \mu\text{m}$  from dcPD, shows that this linear-reference correction was not fully sufficient. The  $da/dt$  shown in Fig. 15b, involves crack extension due to blunting and microvoiding, but the values are elevated due to elastic and plastic deformation effects on the resistivity of the material surrounding the crack tip. This resistance change is sensed by the local voltage probes only and not eliminated by reference probe correction. This local increase in resistance will produce a limit on the capability of the dcPD method to resolve very slow rates of HEAC, as quantified in the Discussion.

A slow-rising  $K$  experiment with Monel K-500 in moist air confirmed this interpretation of each dcPD artifact. Electrical shorting was not observed at lower  $K$  and rising  $K$  deformation caused a slow increase in apparent crack length.

#### Elastic-Plastic Analysis

The images in Fig. 9 establish that HEAC in Monel K-500 (ST-A) was mode I, without crack branching. Neither macroscopic through-thickness plasticity, nor shear walls along specimen edges are associated with these HEAC cracks. None-the-less, the high-elastic  $K$  achieved near the end of IGSCC (Fig. 8) and relatively low strength of Monel K-500 necessitate assessment of the effect of plasticity on stress intensity. Results are presented in Fig. 16, a plot of  $da/dt$  from dcPD versus elastic  $K$  (open symbols, replotted from Fig. 8) and elastic-plastic  $K_J$  (filled symbols, with the elastic  $K$  increased with a plastic zone addition to physical crack length) from the J-integral analysis of SENT load and crack length values with the Ramberg-Osgood description of plastic flow in Monel K-500. This analysis demonstrates essentially no impact of plasticity for applied elastic  $K$  levels below about  $40 \text{ MPa}\sqrt{\text{m}}$ , and up to about a 40%

increase in  $K$  to  $K_J$  for the highest elastic  $K$  levels and load investigated, typical of the experiments conducted with relatively low cathodic polarization above  $-800 \text{ mV}_{\text{SCE}}$ .  $K_{\text{TH}}$  values are only mildly increased (Table 3) and the estimated level of  $da/dt_{\text{II}}$  is unaffected by plasticity correction.

## DISCUSSION

### Accelerated-Quantitative Laboratory Characterization of HEAC in Monel K-500

The rising- $K$  small crack test method successfully characterized intergranular HEAC in ST-A Monel K-500 in terms of quantitative  $K_{\text{TH}}$  and  $da/dt$  versus  $K$  (Figs. 8 and 16). The combination of continuously recorded high resolution crack length detection by dcPD and the damaging role of active crack tip straining, provide the basis for this accelerated test method compared to longer term quasi-static approaches. A similar finding was reported for HEAC in ultra-high strength steel ( $\sigma_{\text{YS}} \sim 1750 \text{ MPa}$ ) [40]; however, there are important differences to note which are unique to the lower strength Monel K-500/NaCl system. If the alloy is highly susceptible to HEAC, such as an ultra-high strength steel [40], or Monel K-500 under severe cathodic polarization in chloride solution, then cracking is similar for both rising  $K$  and quasi-static  $K$ , and dcPD monitoring of the small crack to yield both  $K_{\text{TH}}$  and  $da/dt$  vs  $K$  is the primary attribute of this test method. Simply stated, measurement of rates, over short intervals of crack extension and in a relatively short time, provide the basis to predict cracking over longer times in alternate geometries, as developed in an ensuing section. However, for alloys which resist environmental cracking, or if crack tip passivity interacts with HEAC, the rising  $K$  characteristic will likely lower  $K_{\text{TH}}$  and increase  $da/dt$ . This behavior was observed for Monel K-500 with moderate cathodic polarization, as suggested in Figs. 12 and 13. In such cases crack tip strain rate is an important variable, as detailed elsewhere [66]; this issue is outside the scope of the present study, but may be important in a given application of this test method. Generally, rising  $K$  at a sufficiently slow  $dK/dt$  provides an accurate (susceptible alloy) to conservative (resistant alloy) measure of HEAC threshold and kinetics.

Three factors are unique to the Monel-chloride situation and must be considered in test method use. First, crack surface electrical shorting may obscure low  $K$  subcritical

crack growth. However, results shown in Figs. 6, 12 and 14, which are typical of each potential examined, show that background  $da/dt$  subtraction provides reasonable  $da/dt$  versus  $K$  values to characterize HEAC.

Second, an apparent  $da/dt$  is produced by crack tip plasticity enhancement of alloy resistivity, which was not eliminated by reference probe normalization. It is critical to separate this effect of plasticity and crack tip blunting on apparent crack growth from dcPD, with actual microvoid based damage. Parallel work in an ultra-high strength stainless steel ( $\sigma_{YS} = 1,650$  MPa) showed that slowing rising  $K$  loading at  $1 \text{ MPa}\sqrt{\text{m/h}}$  up to  $80 \text{ MPa}\sqrt{\text{m}}$  produced apparent crack growth rates which increased monotonically to a  $da/dt$  of  $1.0 \text{ nm/s}$  [67]. Real crack growth was not observed by high resolution SEM analysis of this HEAC and microvoid fracture resistant steel; it was concluded that crack tip plasticity created resolution limit of  $1 \text{ nm/s}$  for this steel. For a loading rate of  $0.3 \text{ MPa}\sqrt{\text{m/h}}$ , relevant to the present experiments, this resolution limit should fall by a factor of 3.3 to  $0.3 \text{ nm/s}$ . For lower strength Monel K-500, the experiment conducted at  $-700 \text{ mV}_{\text{SCE}}$  (see Fig. 15b) provides crack length vs time and  $da/dt$  vs  $K$  data with crack growth due to plasticity plus microvoid crack extension (Fig. 10). The  $da/dt$  was  $0.4 \text{ nm/s}$  and accelerated to  $1.3 \text{ nm/s}$  when  $dK/dt$  was increased from  $0.3$  to  $1.0 \text{ MPa}\sqrt{\text{m/h}}$  at  $43.9 \text{ MPa}\sqrt{\text{m}}$ . This level of apparent plasticity-driven false crack growth is similar to that typical of the ultra-high strength steel and establishes a resolution limit of  $0.4 \text{ nm/s}$  for the present experiments, which is represented by the shaded bar in Figs. 8 and 16. This is the justification for defining  $K_{\text{TH}}$  in Table 3 as the stress intensity level which produced a crack growth rate just above  $4 \times 10^{-7} \text{ mm/s}$ . This resolution limit is well below the values of  $da/dt$  at each potential represented in Figs. 8 and 16 and which are attributed to either IG HEAC at potentials below about  $-850 \text{ mV}_{\text{SCE}}$ , mixed IG plus TG HEAC at  $-800 \text{ mV}_{\text{SCE}}$ , and microvoid based crack growth at potentials above  $-750 \text{ mV}_{\text{SCE}}$ .

Monel K-500, stressed at potentials of  $-700$  and  $-750 \text{ mV}_{\text{SCE}}$  show dcPD-measurable rates of stable crack growth in the range of  $0.4$  to  $7\text{-}10 \text{ nm/s}$  (Fig. 16); however, such cracking involved microvoid processes (Figs. 10 and 11) and did not appear to include a H damage mechanism. The SEM images in Figs. 10a and 11 show  $80 \text{ }\mu\text{m}$  of real-stable crack growth for  $-700 \text{ mV}_{\text{SCE}}$  and  $450 \text{ }\mu\text{m}$  of real-stable crack growth for  $-750 \text{ mV}_{\text{SCE}}$ . Assuming that such crack growth began at a  $K$  level of  $45 \text{ MPa}\sqrt{\text{m}}$  and



ended at a final-elastic  $K$  of  $68 \text{ MPa}\sqrt{\text{m}}$ ; the loading time to produce this amount of optically measured crack growth is 83,000 s for average-real crack growth rates of 1.0 nm/s at  $-700 \text{ mV}_{\text{SCE}}$  and 5.5 nm/s at  $-750 \text{ mV}_{\text{SCE}}$ . Considering the  $-800 \text{ mV}_{\text{SCE}}$  case where IG HEAC occurred, the optical microscopy (Fig. 9) and SEM (Fig. 13) analyses 13 for the continuous-slow-rising  $K$  loading revealed  $580 \mu\text{m}$  of stable crack extension ahead of the fatigue precrack. This crack growth occurred between about 410,000 and 475,000 s of loading at  $1 \text{ MPa}\sqrt{\text{m/h}}$  (Fig. 12 b), yielding an average-real  $da/dt$  of 9 nm/s. These rates are above the plasticity-based resolution limit shown in Fig. 16 and agree reasonably with the dcPD-based  $da/dt$  data, suggesting that the accelerated test method is capable of resolving real crack growth rates above about 0.4 nm/s, independent of whether such growth is due to microvoid damage or IG HEAC.

This analysis suggests several practical actions for successful test method application. First, deformation based  $da/dt$  must be considered when resistant alloy-environment systems are characterized with the dcPD method. It will not be possible to measure real-stable  $da/dt$  at rates below 0.4 nm/s for the present experiments with Monel K-500 at a loading rate of  $0.3 \text{ MPa}\sqrt{\text{m/h}}$ , and below 1 nm/s for Monel K-500 (and ultra-high strength steel [67]) at a loading rate of  $1 \text{ MPa}\sqrt{\text{m/h}}$ . Second, when SEM analysis shows that stable crack growth by any mechanism has not occurred, then the false crack growth can be eliminated by using the measured-final potential to calibrate  $V_0$  in Johnson's dcPD calibration equation. For the Monel K-500 specimen tested at  $-750 \text{ mV}_{\text{SCE}}$ , real crack growth occurred, but not by a hydrogen embrittlement method. To confirm this speculation, and provide a basis for characterizing HEAC, a slow-rising  $K$  fracture toughness experiment should be conducted in a benign environment to provide the occurrence of H-free stable crack growth at measurable rates. Such rates should then be compared to the values obtained for the same  $K$  protocol applied to specimens tested in aggressive environments which are capable of producing crack tip H. Third, for precise  $da/dt$  measurement of slow rate cracking, SEM analysis can establish the total amount of HEAC to permit either a qualitative or perhaps quantitative correction of dcPD-based  $da/dt$ . Finally, the increase in  $dK/dt$  in the loading protocol was not ideal since it proportionately increased the level of false  $da/dt$ . The slowest possible  $dK/dt$  should be employed to minimize the magnitude of the plasticity-based false  $da/dt$ . In the limit this

deformation artifact does not occur during a quasi-static K hold period; however, use of this loading mode to avoid plasticity-rise in dcPD may not be possible if  $dK/dt$  is an important variable.

As a third complicating factor, the accuracy of an elastic K analysis must be assessed for lower strength alloys and relatively small size of the SENT specimen. The  $da/dt$  vs K relationships in Fig. 8 were limited because loading was terminated at a preselected-high K level in the range of 80 MPa $\sqrt{m}$  to conserve laboratory test time. (loading to K of 150 MPa $\sqrt{m}$  requires 21 days at 0.3 MPa $\sqrt{m}/h$ .) The results of the elastic-plastic J-integral analysis (Fig. 16) demonstrate that the method can be applied to quantitatively characterize environmental cracking under large scale plasticity. This result, plus the fact that the experiments with Monel K-500 were terminated with a final  $a/W$  below 0.40 and at 70% of the limit load (Eqn. 6), suggest that the small SENT specimen can be successfully loaded to higher levels and with longer crack lengths to achieve a broader description of  $da/dt$  versus K.

J-integral analyses have not been typically utilized to characterize environmental cracking [38,48-51]. The present results demonstrate that an analytical J-integral analysis enhances the test method without displacement measurement typically used to quantify  $J_{Plastic}$ . These results establish the effectiveness of this approach for the Monel class of alloys, and suggest relevance to other materials such as moderate strength alloy and pressure vessel steels ( $600 < \sigma_{YS} < 1000$  MPa). Other estimation methods exist to determine the J-integral [68], including reference stress [69] and remote-strain [70] based approaches. These were not investigated as there is no basis for concluding that either is superior to the above method for the SENT specimen. The load-displacement area method, with unloading compliance calculated from dcPD crack length, offers an alternative to the Eqn. 5 estimation of  $J_{plastic}$  [62,68,71]. The analysis used for  $K_J$  in Fig. 15 must be enhanced to include the effect of stable crack propagation and crack tip unloading [53]. The area based method to determine  $J_{Plastic}$  provides a means to characterize this well known effect [68]. The results of this work provide small specimen HEAC properties, from elastic-plastic analysis of  $K_J$ , which are believed to be quantitatively pertinent to a larger structure under nominally elastic loading, following the J-integral approach to predict fracture toughness [53,62,68,70].



### HEAC susceptibility of Monel K-500

Consistent with literature results, the findings in Figs. 7, 8 and 16 establish that ST-A Monel K-500 is susceptible to significant intergranular HEAC when stressed in aqueous chloride solution at potentials substantially cathodic to the OCP. The magnitude of this deleterious environmental effect is reduced to zero by decreasing level of such applied polarization. The HEAC is severe at  $-1100 \text{ mV}_{\text{SCE}}$  and eliminated at  $-750$  and  $-700 \text{ mV}_{\text{SCE}}$ , but not eliminated at  $-800 \text{ mV}_{\text{SCE}}$ , for the loading conditions explored and compared to a typical open circuit potential of  $-200$  to  $-250 \text{ mV}_{\text{SCE}}$  [28]. This beneficial effect of reduced cathodic polarization is consistent with limited literature results [2,28,29]. Slow strain rate tensile experiments in artificial seawater showed severe HEAC at  $-1000 \text{ mV}_{\text{SCE}}$  [35] and  $-945 \text{ mV}_{\text{SCE}}$  [2], high resistance at  $-850 \text{ mV}_{\text{SCE}}$  [35], and possible immunity at  $-645 \text{ mV}_{\text{SCE}}$  [2]; consistent with the fracture mechanics measurements summarized in Table 3. Raymond reported apparent threshold stress intensity for the onset of HEAC in aged Monel K-500 ( $R_C$  30 and  $\sigma_{\text{YS}} = 813 \text{ MPa}$ ) in 3.5% NaCl solution based on the rising step load test (RSL, with fatigue precrack and governed by ASTM Standard F1634) [28].  $K_{\text{TH}}$  ranged from  $18.4 \text{ MPa}\sqrt{\text{m}}$  at  $-1200 \text{ mV}_{\text{SCE}}$  and  $19.3 \text{ MPa}\sqrt{\text{m}}$  at  $-1000 \text{ mV}_{\text{SCE}}$ , to above  $75 \text{ MPa}\sqrt{\text{m}}$  at both  $-850 \text{ mV}_{\text{SCE}}$  and  $-700 \text{ mV}_{\text{SCE}}$ . This study did not report crack growth rates, the resolution of crack length monitoring based on load decrease, the effect of plasticity on  $K_{\text{TH}}$ , and SEM analysis of the extent of HEAC.

The RSL results are consistent with the data summarized in Table 3, but differences in the two experimental approaches are apparent. In the RSL experiment,  $K_{\text{TH}}$  for HEAC is defined by a resolvable load decrease due to crack extension (not creep) during the static displacement period after each step. Crack growth during the rising K step is not considered. The present results (Fig. 13) show similar HEAC kinetics for slow-rising K and constant K when potential is low and HEAC is severe. This behavior is consistent with the similarly low values of  $K_{\text{TH}}$ , in the range of 16 to  $20 \text{ MPa}\sqrt{\text{m}}$  below  $-1000 \text{ mV}_{\text{SCE}}$ , for the RSL and present rising displacement formats. The  $K_{\text{TH}}$  levels are similarly high for potentials in the range of  $-850 \text{ mV}_{\text{SCE}}$  to  $-700 \text{ mV}_{\text{SCE}}$ , but the present experiments demonstrate HEAC at  $-800 \text{ mV}_{\text{SCE}}$  compared to the suggestion of RSL

immunity for  $K$  up to  $75 \text{ MPa}\sqrt{\text{m}}$  [28]. There are two explanations for this difference. First, some HEAC may have occurred during the RSL test, but was not detected by the load decrease criterion over the selected hold period. Second, HEAC for a mild environmental exposure ( $-800 \text{ mV}_{\text{SCE}}$ , Fig. 12) occurs at vanishingly small  $da/dt$  at constant  $K$ , but progresses at a measurably faster rate during rising  $K$ . The rising  $K$  portion of the RSL test is typically conducted at a high  $dK/dt$  so the difference in amount of HEAC during the rising portion of each experiment could be ascribed to this loading rate difference and in any event would not be detected by load decrease during the step. For Monel K-500 at this potential, HEAC does not appear to occur during the constant displacement (or  $K$ ) hold so this part of the step load protocol is not damaging. These results demonstrate the importance of loading format, particularly  $dK/dt$ , to the extent of HEAC under less aggressive environmental conditions. The relevance of a given experiment depends on the component and stress state of interest. The slow-rising  $K$  approach with precision and continuous detection of crack growth provides a conservative-quantitative measure of  $K_{\text{TH}}$  and  $da/dt$ . These results also demonstrate the importance of high-resolution crack growth rate measurements, with care taken to eliminate or understand the effect of testing artifacts.

Vassiliaros and et al. characterized HEAC in Monel K-500 using a displacement based J-integral approach [38]. For slow loading in moist air (grip displacement rate =  $60 \mu\text{m/h}$ , but  $dK/dt$  was not reported), measured crack growth initiation toughness ( $K_{\text{JIC}}$ ) was  $198 \text{ MPa}\sqrt{\text{m}}$  and  $223 \text{ MPa}\sqrt{\text{m}}$  for air melted and electroslog-remelted heats of Monel K-500, respectively. These values decreased to  $105 \text{ MPa}\sqrt{\text{m}}$  and  $115 \text{ MPa}\sqrt{\text{m}}$  for these two heats, respectively, stressed in 3.5% NaCl solution at  $-1000 \text{ mV}_{\text{SCE}}$ . The tearing modulus was reduced by stressing in the environment, consistent with subcritical HEAC growth, and the fracture mode changed from microvoid-based in air to intergranular in chloride. The cause of the 5-fold higher HEAC “threshold” stress intensity for this work, compared to that reported by Raymond and in the present study at the same cathodic potential ( $105$  to  $115 \text{ MPa}\sqrt{\text{m}}$  vs  $16$  to  $20 \text{ MPa}\sqrt{\text{m}}$ ) is not known, but could be due to crack growth detection resolution and differing loading rate ( $dK/dt$ ).

### Mechanism Informed Modeling of HEAC Kinetics

It is important to model the  $K_{TH}$  and  $da/dt$  versus  $K$  properties characteristic of HEAC in order to strengthen fundamental understanding and reduce the amount of experimentation required to support management of EAC [13,41]. Of particular importance is quantitative prediction of the applied-cathodic potential dependencies of  $K_{TH}$  and Stage II crack growth rate. The models summarized in the Introduction are specific to the hydrogen embrittlement mechanism, which was justified for intergranular HEAC, and thus provide a firm basis for predictions of cracking in Monel K-500. These models are based on hydrogen embrittlement in the crack tip FPZ, where the damaging H is produced on the crack tip surface in equilibrium with the local crack tip over-potential for H production governed by local pH and electrode potential [13]. This source for subsequent H diffusion into the crack tip FPZ is likely dominant for HEAC of ultra-high strength steel since the electrochemical conditions, stress state, and short H diffusion distance ( $\sim 1 \mu\text{m}$  [13]) all favor this scenario.

For Ni-based alloys, H production under cathodic polarization is greater on boldly exposed specimen surfaces due to crack tip pH rise above bulk (Footnote 3) and modest IR difference (Fig. 2) [17,72]. The net decrease in crack tip versus bold surface production of  $C_{H-Diff}$  is quantified in Fig. 5. However, the intensified 3-dimensional stress state at the crack tip and mid-plane of the SENT specimen appears to dominate HEAC over the boldly exposed surface locations. Bulk H charging during a 500,000 s experiment is not likely; the diffusion distance proportional to  $2(D_H t)^{1/2}$  is 0.16 mm for the measured effective diffusivity of H in Monel K-500,  $1.3 \times 10^{-10} \text{ cm}^2/\text{s}$  [17]). This distance for full-H penetration is 13% of the half-thickness of the SENT specimen. The dominance of crack tip H uptake is supported by the shape of HEAC shown in Fig. 9 where the specimen thickness is 2.5 mm. HEAC advanced regularly with no preference for enhanced crack growth near the boldly exposed surface. This behavior is clearly apparent for the -1000 to -800  $\text{mV}_{SCE}$  cases in Fig. 9. For the experiment at -750  $\text{mV}_{SCE}$ , stable cracking is localized to the center of the specimen; however, this crack growth was most likely not by HEAC since the crack surface (Fig. 11) is entirely microvoid-based.

This discussion is qualitative; however, both  $K_{TH}$  and  $da/dt_{II}$  are predicted in the following section, using the quantitative dependence of  $C_{H-Diff}$  on  $E_{Applied}$  from Fig. 5 and Eqn. 9. This modeling is in progress; the results reported for  $K_{TH}$  and Stage II  $da/dt$  may be refined by additional modeling necessitated by subtle complexities associated with crack tip H production, uptake and diffusion in Monel K-500.

### Threshold for HEAC

Prediction of the applied potential dependence of  $K_{TH}$  for the onset of HEAC utilizes the model put forth by Gerberich and coworkers (Eqns. 1 and 3) [39], and validated by Gangloff for a wide range of steels [40,41]. The first step in modeling is to determine crack tip diffusible H concentration as a function of applied potential for Monel K-500 in near-neutral NaCl solution. This concentration dependence is established by the results given in Fig. 5 and Eqn. 9, which followed from the H uptake law for a planar surface electrode of Monel K-500 (ATI Allvac lot, Fig. 4). The next step is to determine: (a) the value of crack tip hydrostatic stress, typically a multiple of alloy yield strength [43], for use in Eqn. 3 to translate  $C_{H-Diff}$  at the crack tip to a stress field-enhanced concentration, and (b) the values of the constants ( $\beta'$ ,  $\alpha$ ,  $\alpha''$ , and  $k_{IG}$ ) in the  $K_{TH}$  model (Eqn. 1). The ratio  $\sigma_H/\sigma_{YS}$  was assumed to equal 6.0 which is reasonable for either a high work hardening alloy such as Monel K-500 [53] or if strain gradient plasticity impacts the crack tip stress distribution [43]. The values of  $\alpha''$  (0.00018 MPa m) and  $\beta'$  (0.26 (MPa $\sqrt{m}$ )<sup>-1</sup>) were those established by Gerberich's original dislocation model of the crack tip stress field, and verified by extensive correlations for steels and a nickel based superalloy, IN718 [41]. The value of  $k_{IG}$  depends on material and was selected to equal 0.70 MPa $\sqrt{m}$  so as to predict  $K_{TH} \sim K_{IC}$  of 130 MPa $\sqrt{m}$  when  $C_{H-Diff}$  equals 0. The parameter,  $\alpha$ , was adjusted to equate the measured and predicted values of  $K_{TH}$  for a single potential;  $\alpha' = 9.3$  MPa $\sqrt{m}$  per atom fraction of H in order to achieve this forced fit.

Model predictions using these inputs are presented in Figs. 17 and 18. Detailed discussion of these  $K_{TH}$  predictions is premature pending model refinement. However, several points are clear. First, the model reasonably captures the dependence of  $K_{TH}$  on crack tip diffusible H concentration (Fig. 17); specifically,  $K_{TH}$  decreases strongly with initial increase in  $C_{H-Diff}$  and then reaches a lower-limit at high values of crack tip H

concentration. Second, the model reasonably captures the strong dependence of  $K_{TH}$  on applied potential, Fig. 18. Crack chemistry modeling (Fig. 5 and Eqn. 9) shows that the crack tip diffusible H concentration tends to 0 at an applied potential of -764 mV<sub>SCE</sub>. The HEAC experiments clearly established that HEAC occurred at -800 mV<sub>SCE</sub>, but not at either -750 mV<sub>SCE</sub> or -700 mV<sub>SCE</sub>. This strong agreement validates this modeling approach. Finally, the model predictions in Figs. 17 and 18 are very sensitive to the absolute values of the various parameters used in the  $K_{TH}$  model, particularly the intrinsic Griffith toughness ( $k_{IG}$ ) and the H-concentration damage-weighting factor ( $\alpha$ ). The values of the parameters used for the quality of fits shown in Figs. 17 and 18 are reasonable based on previous applications of this modeling approach [40,41]. However, these parameters are not defined by independent measurements or experiments; at present, they must be viewed as curve-fitting constants. Finally, the modeling of  $K_{TH}$  versus applied potential depends on the input dependence of crack tip diffusible H concentration on applied potential (Fig. 5 and Eqn. 9). This dependence varies for H concentration measured by either hot extraction (LECO) or thermal desorption spectroscopy, as reported in Fig. 4 and observed for an alternate heat of Monel K-500 [17]. It is likely that differences in these H uptake laws will result in different values of  $\alpha$  necessary to fit the  $K_{TH}$  model to a single-applied potential. However, differences in  $C_{H-Diff}$  versus applied E could also alter the shape of the overall fit between  $K_{TH}$  and  $E_{Applied}$ . Work is in progress to investigate this issue.

### Stage II Crack Growth Rate

Knowing the relationship between crack tip diffusible H concentration and applied potential, it is possible to predict the potential dependence of Stage II crack growth rate, which is limited by H diffusion in the fracture process zone. Eqn. 2 provides the specific prediction in this regard, with a single adjustable parameter,  $C_{Crit}$ , and all other terms in this model known. The  $D_H$  for H in aged Monel K-500 at 25°C was reported to be  $5 \times 10^{-11}$  cm<sup>2</sup>/s [32],  $1.5$  to  $1.9 \times 10^{-10}$  cm<sup>2</sup>/s [31], and  $9 \times 10^{-11}$  to  $4 \times 10^{-10}$  cm<sup>2</sup>/s [17]; an average H diffusivity of  $1 \times 10^{-10}$  cm<sup>2</sup>/s is used for  $da/dt$  modeling. The  $x_{Crit}$  in Eqn. 2 is 1  $\mu$ m for HEAC in a wide range of high strength alloys [42]. The maximum crack tip hydrostatic stress in Eqn. 3 is assumed to be  $6\sigma_{YS}$ , consistent with the assumption used



for the  $K_{TH}$  model. The relationship between  $C_{H-Diff}$  in Eqn. 3 and applied potential is given for the ATI Allvac lot of Monel K-500 by the results in Fig. 5 and Eqn. 9.

The model predictions of Stage II crack growth rate are presented in Figs. 19 and 20, using a best fit value for  $C_{Crit} = 40$  wppm. Agreement between predicted and measured (Table 3) Stage II crack growth rate is excellent when considered as a function of either crack tip diffusible H concentration (Fig. 19) or applied cathodic potential (Fig. 20). The absolute value of the fastest Stage II crack growth rate measured at  $-1100$  mV<sub>SCE</sub> applied potential is in excellent agreement with the reduced form of Eqn. 2 where the inverse error function approaches 1.0 when  $C_{H\sigma} \gg C_{Crit}$ . In this case the predicted Stage II crack growth rate equals  $4D_H/x_{Crit}$ , and is between  $0.02$  and  $0.16$   $\mu\text{m/s}$  for the range of literature-reported diffusivities noted above. A reasonable-average value of  $D_H$  is  $1-2 \times 10^{-10}$   $\text{cm}^2/\text{s}$ , corresponding to a predicted Stage II  $da/dt$  of  $0.04-0.08$   $\mu\text{m/s}$ . From Figs. 16 and 19 as well as Table 3, the fastest measured Stage II  $da/dt$  (at  $K$  of  $50$  MPa $\sqrt{\text{m}}$ ) is  $0.17$   $\mu\text{m/s}$ .

This good agreement between measured and modeled crack growth rate affirms the validity of HEAC in Monel K-500 at cathodic potentials and rate limited by H diffusion in the crack tip process zone. Note that this model prediction model prediction does not rely on any adjustable parameters. Moreover, the inverse error function operating on the concentration term of  $(1-C_{Crit}/C_{H\sigma})$  dictates the novel and technologically important shape of the potential dependence of  $da/dt$  (Fig. 20) where the crack growth rate mildly decreases with increasing  $E_{Applied}$  (decreasing crack tip diffusible H concentration, Fig. 5 and Eqn. 9), until a point where the growth rate plummets with further rise in applied potential. For the parameters employed in the present model, this severe drop-off in HEAC  $da/dt$  is predicted to occur at  $-785$  mV<sub>SCE</sub>, in excellent agreement with the measurements in Table II. Recall that IG HEAC was produced at  $-800$  mV<sub>SCE</sub>, with the rate plotted in Fig. 20, but SEM analysis did not resolve any HEAC for the experiments conducted at either  $-750$  mV<sub>SCE</sub> or  $-700$  mV<sub>SCE</sub>. This sharp change in HEAC rate is a direct result of the crack tip electrochemical boundary conditions for H diffusion in the FPZ.

The good agreement between the measured and model predicted dependencies of  $K_{TH}$  and Stage II crack growth rate on applied-cathodic potential supports the conclusion that a critical level of cathodic polarization must be exceeded before HEAC can progress at a significant rate in Monel K-500 stressed in NaCl. The precise level of this potential could depend on subtle differences in Monel metallurgy through microstructure and composition effects on the H uptake law (Fig. 5 and Eqn. 9), as well as on key parameters in the micromechanical models, particularly  $k_{IG}$ ,  $\alpha$ , and  $C_{Crit}$ .

### Fracture Mechanics Simulation of Component HEAC

The slow crack growth rates measured for Monel K-500, and strong dependence on the level of applied cathodic polarization, provide an ideal system for application of a fracture mechanics based crack growth approach to predict component life. A fracture mechanics software code, *SCCrack*, has been written to predict HEAC propagation life in Monel K-500 components as a function of applied stress, residual stress, initial defect size, and applied potential [47].<sup>5</sup> The basis for this program is the similitude concept, which is widely used in fatigue crack growth modeling and which was proposed for HEAC and SCC [44-46]. The graphical user interface for *SCCrack* is shown in Figure 21. The program uses a fast Monte Carlo routine to conduct multiple simulations of HEAC growth to component failure given input distributions of defect size, applied potential, and  $da/dt$  versus  $K$  property laws. The input  $da/dt$  versus applied-elastic  $K$  relationships are shown in Fig. 22, based on the laboratory data presented in Fig. 8. These inputs are used to predict IGSCC from an existing crack in ten different geometries.

The results of a typical *SCCrack* model simulation are shown in Fig. 23, which is a hypothetical example not intended to represent a specific failure or application of Monel K-500. The initial flaw is a semi-elliptically-shaped crack at the root of a thread in a uniaxially-tensile-loaded bolt. As the crack grows in the radial direction of the bolt, in a simple Mode I orientation, this semi-elliptical shape transitions to a straight-chord crack front. The applied stress was fixed at 40% of the material yield strength, the applied

---

<sup>5</sup> *SCCrack* resulted from collaboration between Professor Gangloff and staff of VEXTEC Corporation including Michael Oja, Vladimir Ogarevic and Robert Tryon.



potential was fixed at  $-900 \text{ mV}_{\text{SCE}}$ , and the mean crack depth was  $150 \text{ }\mu\text{m}$  with a coefficient of variation (standard deviation to mean ratio) assumed to be 0.20. The distribution of initial crack depths is represented by the range between  $110 \text{ }\mu\text{m}$  and  $205 \text{ }\mu\text{m}$  shown by the top image in Fig. 23. The initial K level for this set of simulations varied with starting crack depth, but was  $20\text{-}22 \text{ MPa}\sqrt{\text{m}}$ . 100 simulations were performed with the Monte Carlo selection scheme used to select the starting crack depth from this assumed distribution. The lower image shows simulated crack extension, with failure occurring at about 2,000 h as the crack exceeded 10 mm. The distribution of either failure time, or time required to achieve a specific crack depth, is determined from the simulation results shown in the lower plot of Fig. 23.

The strong effect of applied cathodic polarization on IGSCC life is shown by the *SCCrack* model simulation results presented in Fig. 24. The initial flaw is a semi-elliptically-shaped crack at the root of a thread in a uniaxially-tensile-loaded bolt. As the crack grows, this semi-elliptical shape transitions to a straight-chord crack front. The initial crack depth was fixed at  $100 \text{ }\mu\text{m}$ . The applied stress was maintained constant at one of four values between 40% and 70% of the Monel K-500 yield strength. For a crack depth of  $100 \text{ }\mu\text{m}$  ahead of the thread root, this set of deterministic conditions yielded initial stress intensity levels of between  $20.7 \text{ MPa}\sqrt{\text{m}}$  and  $36.3 \text{ MPa}\sqrt{\text{m}}$ . The level of applied-cathodic polarization was varied about a mean of  $-850 \text{ mV}_{\text{SCE}}$ , with a coefficient of variation of 0.06. Assuming that the potentials in this simulation are normally distributed, values will be between  $-952 \text{ mV}_{\text{SCE}}$  and  $-748 \text{ mV}_{\text{SCE}}$  at the 95% confidence level. 100 simulations were performed with the Monte Carlo selection of potential, at each of the four-constant stress levels. Growth rates, for a potential between the two proximate values of the input  $da/dt$  versus K data (Fig. 22) were linearly interpolated. Bolt failure was typically defined by achievement of a maximum crack size of 10 mm for the size of bolt which was modeled. For each stress examined, the distribution of time-to-failure is extreme, between 100 h and  $10^6$  h or longer. This range of lives is a direct reflection of the very strong potential dependence of IG HEAC, as demonstrated by the experimental measurements in Fig. 8 and 16, as well as by the micromechanical model predictions shown in Figs. 17 through 20. Monel K-500 resisted IGSCC when stressed at  $-700$  and  $-750 \text{ mV}_{\text{SCE}}$ , but was prone to rapid cracking at  $-900 \text{ mV}_{\text{SCE}}$ .

The theoretical predictions of very slow rates of IGSCC in the potential range above about  $-775 \text{ mV}_{\text{SCE}}$  strengthen the impact of the relatively short term measurements of such crack growth. The *SCCrack* provides the means to quantitatively relate such science-based laboratory work to predict the distribution of component performance. Additional research is required to: (a) validate the predictions of this modeling approach and (b) raise the confidence associated with predictions of long-term component performance based on short term accelerated laboratory experimentation.

## CONCLUSIONS

- The rising displacement test method, with continuous-precision dcPD monitoring of a small crack provides an effective-accelerated characterization of environmental cracking in Monel K-500, particularly when augmented to account for artifacts due to crack surface electrical contact, highly localized crack tip plasticity under small-scale yielding, and small-specimen ligament plasticity.
- For Monel K-500, the rising displacement test method is capable of resolving real crack growth rates of  $0.4 \text{ nm/s}$  and faster for a constant-applied  $dK/dt$  of  $0.3 \text{ MPa}\sqrt{\text{m/h}}$ . This growth rate resolution is directly proportional to  $dK/dt$ , and may depend on alloy strength.
- An analytical J-integral analysis characterizes HEAC in Monel K-500, without the need to measure displacement or unloading compliance, thus providing material-property data for simulation of cracking in a larger and elastically loaded structure.
- Solution treated and aged Monel K-500 is susceptible to severe intergranular hydrogen environment assisted cracking in NaCl solution when under cathodic polarization in the range of  $-800 \text{ mV}_{\text{SCE}}$  and higher. Such cracking is eliminated by reduced cathodic polarization in the range of  $-750 \text{ mV}_{\text{SCE}}$  and lower.

- HEAC in Monel K-500 is exacerbated by rising  $K$  and active crack tip strain rate, compared to quasi-static loading, but only for environmental conditions where cracking is mild to moderate.
- A rescaled crevice model, coupled with measured-local crevice potential and pH, was combined with a H uptake law measured by thermal desorption spectroscopy for Monel K-500, to establish the strong effect of applied potential on crack tip H concentration.
- Diffusible H concentration produced at the crack tip in Monel K-500 decreased with increasing applied potential and was essentially below the experimental resolution limit for applied potentials above  $-764 \text{ mV}_{\text{SCE}}$ .
- Good agreement between the measured and micromechanical model predicted dependencies of  $K_{\text{TH}}$  and Stage II crack growth rate on applied-cathodic potential supports the conclusion that a critical level of cathodic polarization must be exceeded before HEAC can progress at a significant rate in Monel K-500 stressed in NaCl. The precise level of this potential could depend on subtle differences in Monel metallurgy through microstructure and composition effects on H uptake, as well as on key parameters in the micromechanical models.
- A fracture mechanics-based program, *SCCrack*, predicts distributions of cracked-component life as limited by HEAC using the input from accelerated laboratory experiments strengthened by electrochemical measurements of crack tip H and micromechanical mechanism-based modeling. The effect of a distribution of applied-cathodic polarization on component life is strikingly strong, reflecting the dominant influence of cathodic polarization on rates of IG HEAC.

## ACKNOWLEDGEMENTS

This research was sponsored by ONR Grant N00014-10-1-0552 under the direction of Dr. Airan Perez. Fracture mechanics experiments were conducted by Fracture

Technology Associates and Mr. J. Keith Donald, enabled by a technology transfer from the University of Virginia under STTR Topic No. N08-T010 (Phase II Contract #N68335-09-C-0378) managed by Dr. Jeffrey Waldman (NAVMAR) and Dr. William E. Frazier (NAVAIR).

## REFERENCES

1. K.D. Eifird, Materials Performance, 1985, vol. 24, pp. 37-40.
2. L.H. Wolfe and M.W. Joosten, SPE Production Engineering, vol. 3, 1988, pp. 382-386.
3. L.H. Wolfe and C.C. Burnette, "Hydrogen Embrittlement of Cathodically Protected Subsea Bolting Alloys", Document 20294-MS, Society of Petroleum Engineers, 1990, 32 pages. (<http://www.onepetro.org/mslib/servlet/onepetropreview?id=00020294>)
4. M.W. Joosten and L.H. Wolfe, "Failures of Nickel-Copper Bolts in Subsea Applications", Offshore Technology Conference Paper No. 5553-MS, April, 1987.
5. L.H. Wolfe, C.C. Burnette and M.W. Joosten, "Hydrogen Embrittlement of Cathodically Protected Subsea Bolting Alloys", Corrosion 93, Paper No. 288, NACE International, Houston, TX (1993).
6. G.A. Scott, "Studbolting Experience in the Underwater Environment of the North Sea", 17<sup>th</sup> Offshore Technology Conference, Paper No. OTC 5050, Houston, TX (1985).
7. R.E. Butler, in Engineering with Copper-Nickel Alloys, Metals Society, London, UK, pp. 79-84 (1988).
8. L.H. Wolfe, C.C. Burnette and M.W. Joosten, Materials Performance, pp. 14-21, July (1993).
9. C.A. Clark, S. Driscoll and P. Guha, British Corrosion Journal, vol. 27, pp. 157-160 (1997).
10. J.R. Scully and M.G. Vassilaros, "The Hydrogen Embrittlement Susceptibility of Monel Alloy K-500", Report DTNSRDC/SME-84-69, David Taylor Naval Ship Research and Development Center, Bethesda, MD, 1984.
11. R.D. Bayles et al., "Monel K-500 Hydrogen Embrittlement", Naval Surface Treatment Center MR2010 proceedings presentation, 2010. (<http://www.nstcenter.com/docs/PDFs/MR2010/Thurs-1-Presentations/10-Bayles.PDF>)
12. H.R. Copson and C.F. Cheng, Corrosion, vol. 12, 1956, pp. 647-633.
13. R.P. Gangloff, in Comprehensive Structural Integrity, I. Milne, R.O. Ritchie and B. Karihaloo, Editors-in-Chief, J. Petit and P. Scott, Volume Editors, Vol. 6, Elsevier Science, New York, NY, 2003, pp. 31-101.
14. J.A. Lillard, "Environment Assisted Cracking of a Nickel-Based Superalloy in Hydrogen-Producing Solutions", PhD Dissertation, University of Virginia, Charlottesville, VA, 1998.
15. R.B. Rebak, in Environment Induced Cracking of Materials (EICM-2), Sergei Shipilov, R.H. Jones, J.-M. Olive, and R.B. Rebak, Eds., Elsevier Science, Oxford, UK, 2007, pp. 435-446.

16. R.H. Jones and S.M. Bruemmer, in Environment Induced Cracking of Metals, R.P. Gangloff and M.B. Ives, Eds., NACE, Houston, TX, 1990, pp. 287-310.
17. J. Ai, H. Ha, R.P. Gangloff, and J.R. Scully, "Hydrogen Diffusion and Trapping in a Precipitation Hardened Ni-Cu-Al Alloy: UNS N05500 (Monel Alloy K-500)", Acta Materialia, in review, 2012.
18. S. Lynch, in Gaseous Hydrogen Embrittlement of Materials in Energy Technologies: The Problem, Its Characterization, and Effects on Particularly Alloy Classes, Volume 1, R.P. Gangloff and B.P. Somerday, Eds., Woodhead Publishing Limited, Cambridge, UK, 2012, pp. 274-346.
19. Y.D. Park, D.L. Olsson, A. Landau and M. Pinkas, Corrosion, 2006, vol. 62, pp. 395-402.
20. R. Otsuka, T. Maruno and H. Tsuji, in International Congress on Metallic Corrosion, Volume 2, National Research Council, Canada, 1984, pp. 270-277.
21. M.L. Martin, B.P. Somerday, R.O. Ritchie, P. Sofronis and I.M. Robertson, Acta Materialia, vol. 60, 2012, pp. 2739-2745.
22. Y. Fukai, Journal of Alloys and Compounds, vol. 356-357, 2003, pp. 263-269.
23. M.H. Kamdar, in Second International Congress on Hydrogen in Metals, P. Azou, Ed., Paper No. 3D10, Pergamon Press, Oxford, UK, 1977, pp. 1-11.
24. D.H. Lassila and H.K. Birnbaum, Acta Metallurgica, vol. 35, 1987, pp. 1815-1822.
25. D.H. Lassila and H.K. Birnbaum, Acta Metallurgica, vol. 36, 1988, pp. 2821-2825.
26. N.R. Moody, S.L. Robinson and W.M. Garrison, Jr., Res Mechanica, vol 30, 1990, pp. 143-206.
27. D.M. Symons, Engineering Fracture Mechanics, vol. 68, 2001, pp. 751 to 771.
28. L. Raymond, "Fracture and Stress Corrosion Cracking Resistance of C465, BioDur 108, SpT 13-8, K-Monel 500, and Zeron 100", LRA Report #CTC'071024, L. Raymond and Associates, Newport Beach, CA, 2008.
29. D.M. Aylor, "A Hydrogen Embrittlement Evaluation of High Strength Non-Ferrous Materials for Fastener Applications", Proceedings of the 1992 Tri-Service Corrosion Conference, M. Levy, Ed., AMPTIAC Document No. AMO26091, 1992.
30. J.L. Mihelich and A.R. Troiano and Nature, vol. 197, 1963, pp. 996-997.
31. J.A. Harris, R.C. Scarberry and C.D. Stephens, Corrosion, vol. 28, 1972, pp. 57-62.
32. C.D.S. Tuck, Z. Xianghua and D.E.J. Talbot, British Corrosion Journal, vol. 29, 1994, pp. 70-74.
33. C.E. Price and R.S. Fredell, Metallurgical Transactions A, vol. 17A, 1986, pp. 889-898.
34. A.W. Funkenbush, L.A. Heldt and D.F. Stein, Metallurgical Transactions A, vol. 13A, 1982, pp. 611-618.
35. M.G. Koul and P. S. LeGrand, "Environmentally Assisted Cracking Evaluation of UNS N06686 Using Constant Extension Rate Testing", Corrosion 2011, Paper 11296, NACE International, Houston, TX, 2011, 15 pages.
36. M.A. Natishan and W.C. Porr, Jr., in Structural Integrity of Fasteners, ASTM STP 1236, P.M. Toor, Ed., American Society for Testing International, Conshohocken, PA, 1995, pp. 81-92.



37. S. Bechtle, M. Kumar, B.P. Somerday, M.E. Launey and R.O. Ritchie, Acta Materialia, vol. 57, 2009, pp. 4148-4157.
38. M.G. Vassilaros, R.L. Juers, M.E. Natishan and A.K. Vasudevan, in *Slow Strain Rate Testing for Evaluation of Environmentally Induced Cracking Research and Engineering Applications*, ASTM STP 1210, R.D. Kane, Ed., American Society for Testing and Materials International, West Conshohocken, PA, 1993, pp. 123-133.
39. Gerberich Y. Katz, N. Tymiak and W.W. Gerberich, Engr. Frac. Mech., vol. 68, 2001, pp. 619-646.
40. Yongwon Lee and R.P. Gangloff, Metallurgical and Materials Transactions, A, 2007, vol. 38, pp. 2174-2190.
41. R.P. Gangloff, in Hydrogen Effects on Materials, B.P. Somerday, P. Sofronis, and R.H. Jones, Eds., ASM International, Materials Park, OH, pp. 1-21 (2009).
42. R.P. Gangloff, in *Hydrogen Effects on Material Behavior and Corrosion Deformation Interactions*, N.R. Moody, A.W. Thompson, R.E. Ricker, G.S. Was and R.H. Jones, Eds., The Minerals, Metals & Materials Society, Warrendale, PA, pp. 477-497 (2003).
43. U. Komaragiri, S.R. Agnew, R.P. Gangloff and M.R. Begley, Journal of Mechanics and Physics of Solids, vol. 56, 2008, pp. 3527-3540.
44. D.P. Williams, International Journal of Fracture, vol. 9, 1973, pp. 63-74.
45. R.P. Wei, S.R. Novak and D.P. Williams, Mats. Res. Stds., vol. 12, 1972, pp. 25-30.
46. R.P. Wei, *Fracture Mechanics: Integration of Mechanics, Materials Science and Chemistry*, Cambridge University Press, New York, NY, 2010.
47. J. Waldman, R.P. Gangloff and W.E. Garrison, *Development of Corrosion-Hydrogen Crack Resistant Aircraft Alloys from Mechanistic Understanding*, Final Report, STTR Topic No. N08-T010 (Phase II), Navmar Applied Sciences Corporation, Warminster, PA, 2011.
48. R.A. Mayville, R.J. Warren and P.D. Hilton, Transactions of the ASME, vol. 109, 1987, pp. 188-193,
49. J. Alvarez and F. Gutierrez-Solana, Nuclear Engineering and Design, vol. 188, 1999, pp. 185-202.
50. W. Dietzel, A. Atrens, and A. Barnoush in Gaseous Hydrogen Embrittlement of Materials in Energy Technologies: The Problem, Its Characterization, and Effects on Particularly Alloy Classes, Volume 1, R.P. Gangloff and B.P. Somerday, Eds., Woodhead Publishing Limited, Cambridge, UK, 2012, pp. 237-273.
51. G. Abramson, J.T. Evans and R.N. Parkins, Metallurgical Transactions A, vol. 16A, 1985, pp. 101-108.
52. G.K. Dey and P. Mukhopadhyay, Materials Science and Engineering, vol. 84, 1986, pp. 177-189.
53. T.L. Anderson, *Fracture Mechanics*, 3<sup>rd</sup> Edition, Taylor & Francis, Boca Raton, LA, 2005, pp. 121-123, 398-400, 445-446.
54. [www.specialmetals.com](http://www.specialmetals.com).
55. R. Bayles, Private communication, Naval Research Laboratory, Washington, DC, 2012.

56. R.P. Gangloff, D.C. Slavik, R.S. Piascik and R.H. Van Stone, in *Small Crack Test Methods*, ASTM STP 1149, J.M. Larsen and J.E. Allison, Eds., ASTM, Philadelphia, PA, 1992, pp. 116-168.
57. J.K. Donald and J. Ruschau, in *Fatigue Crack Measurement: Techniques and Applications*, EMAS, West Midlands, UK, 1991, pp. 11-38.
58. H.H. Johnson, Mater. Res. Stand., 1965, vol. 5, pp. 442-45.
59. H. Tada, P. C. Paris and G. R. Irwin, in *The Stress Analysis of Cracks Handbook*, Paris Productions Incorporated, St. Louis, Missouri, 1985, pp. 2.10-2.12.
60. V. Kumar, M.D. German and C.F. Shih, *An Engineering Approach for Elastic-Plastic Fracture Analysis*, EPRI final report NP-1931, Electric Power Research Institute, Palo Alto, CA, 1981.
61. S.A. English and N.K. Arakere, International Journal of Plasticity, 2011, vol. 27, pp. 920-939.
62. S. Cravero and C. Ruggieri, Engineering Fracture Mechanics, 2007, vol 74, pp. 2735-2757.
63. J.S. Lee, M.L. Reed, R.G. Kelly, Journal of the Electrochemical Society, 2004, vol. 151, pp. B423-B433.
64. A.W. Hassel, K. Fushimi and M. Seo, Electrochemistry Communications, 1999, vol. 1, pp. 180-183.
65. C.E. Price and G.W. Henderson, Fatigue and Fracture of Engineering Materials and Structures, 1988, vol. 11, pp. 493-500.
66. B.P. Somerday, L.M. Young and R.P. Gangloff, Fatigue and Fracture of Engineering Materials and Structures, 2000, vol. 23, pp. 39-58.
67. G. Pioszak and R.P. Gangloff, unpublished research, University of Virginia, Charlottesville, VA (2012).
68. Xian-Kui Zhu and J.A. Joyce, Engineering Fracture Mechanics, 2012, vol. 85, pp. 1-46.
69. R.A. Ainsworth, Engineering Fracture Mechanics, 1984, vol. 19, pp. 633-642.
70. K.I. Azzabi, A.R. Luxmoore and M.M.K. Lee, International Journal of Fracture, 1991, vol. 63, pp. 75-87.
71. M.J. Haynes and R.P. Gangloff, Journal of Testing and Evaluation, 1997, vol. 25, pp. 82-98.
72. B.A. Kehler and J.R. Scully, Corrosion, 2008, vol. 64, pp. 465-477.



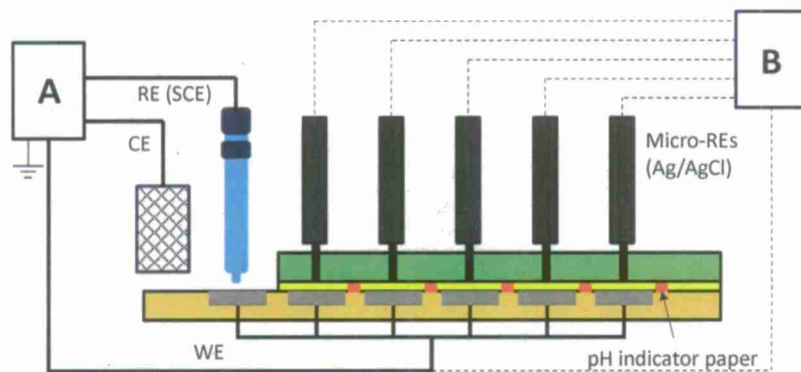


**Figure 1** The artificial crevice electrochemical cell, where A is a potentiostat, B is a multimeter used to measure local potential of 6-shortcd disk electrodes sandwiched between an acrylic bottom plate, plastic shim, and acrylic top plate. Standard and micro-reference electrodes (RE) measured potential and indicator paper measured local pH.

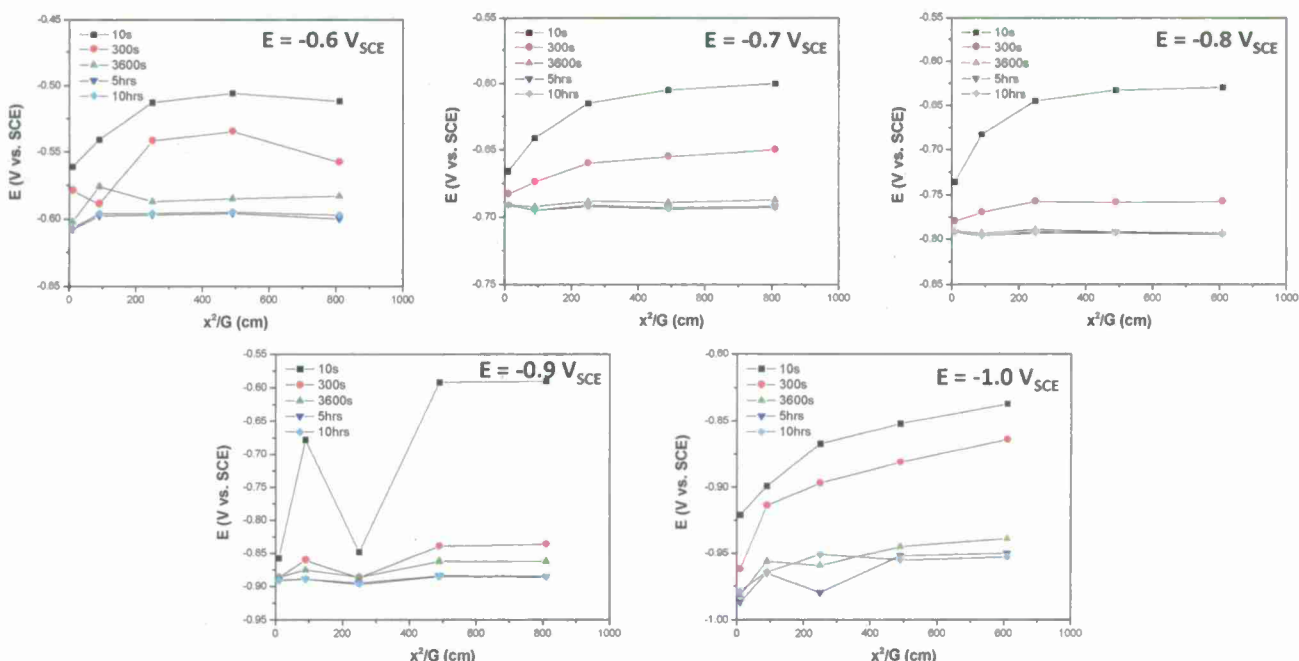


**Figure 2** Local potential with respect to SCE, measured at different locations along the artificial crevice (Fig. 1) between Monel K-500<sup>1</sup> and the acrylic top plate as a function of external-applied potentials and exposure time. The crevice gap was fixed at  $G = 1$  mm.

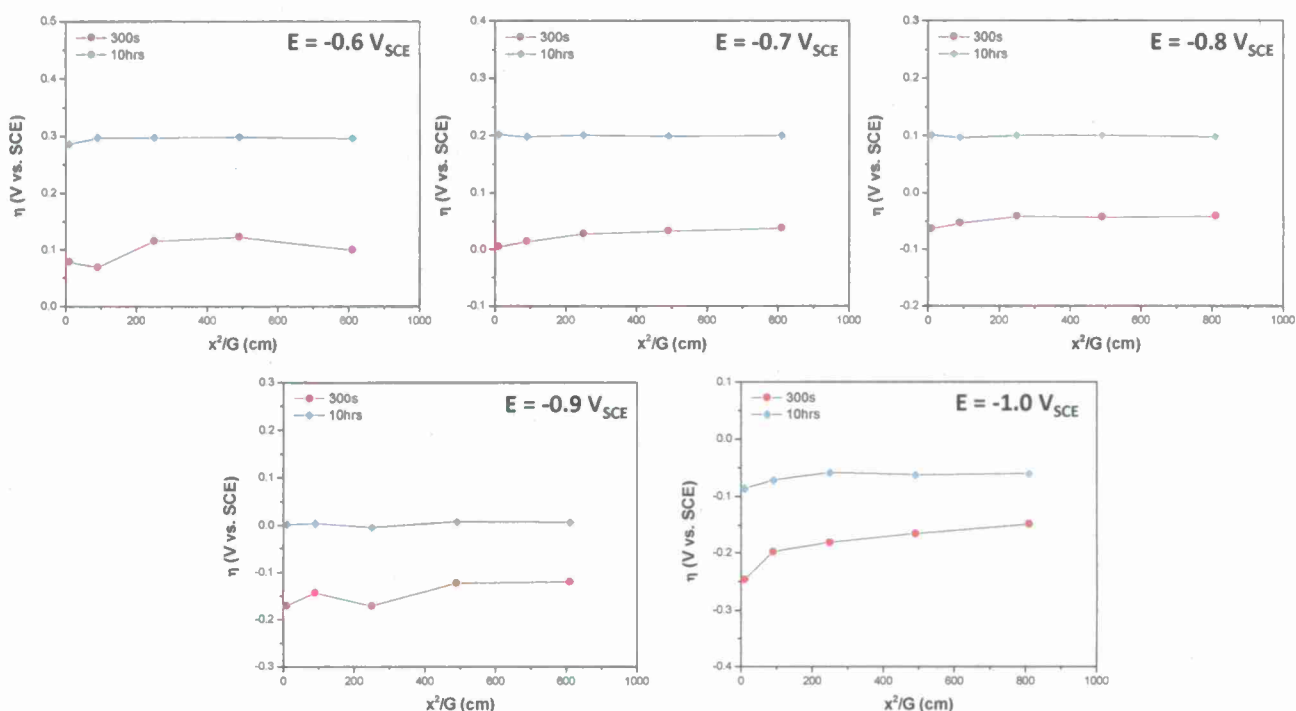


**Figure 3** Local H overpotential versus normalized distance into the artificial crevice as a function of external applied potential for exposure times of 300 s and 10 h. The crevice gap was fixed at  $G = 1$  mm.

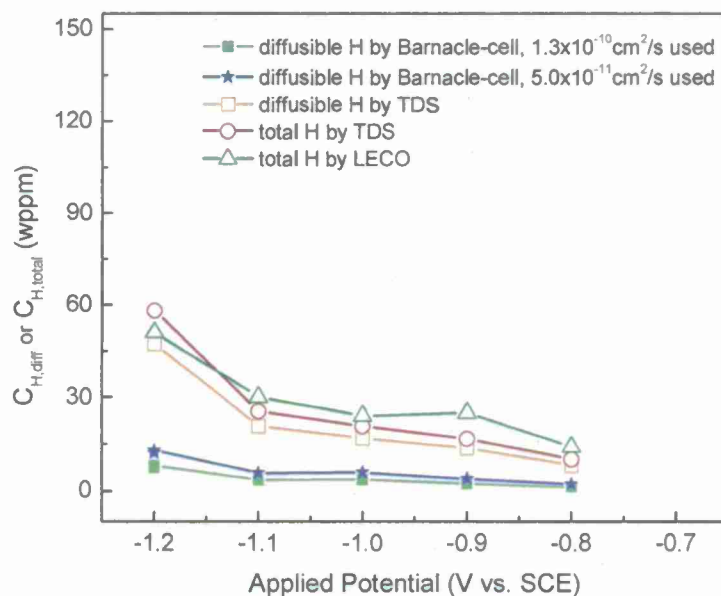


**Figure 4** Dissolved total and diffusible H concentration measured versus applied potential for Monel K-500 (ST-A, ATI Allvac 2011) planar electrodes immersed in 0.6M NaCl (pH 8). Both Barnacle Cell and LECO-calibrated TDS methods were used, with the details reported elsewhere [17].

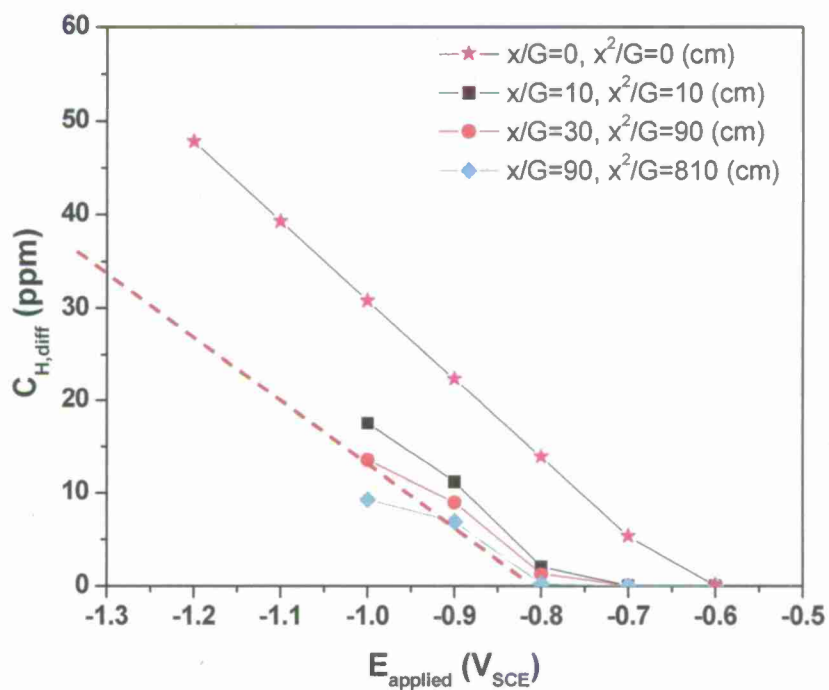


**Figure 5** Relationship between applied bold-surface potential and diffusible H concentration produced at various locations within an artificial crevice for ST-A Monel K-500 (ATI Allvac lot), immersed in 0.6M NaCl solution (bulk pH 8) for 300 s.  $C_{\text{H-Diff}}$  is based on the TDS-established H uptake relationship in Fig. 4 and the dashed line is given by Eq. 9.

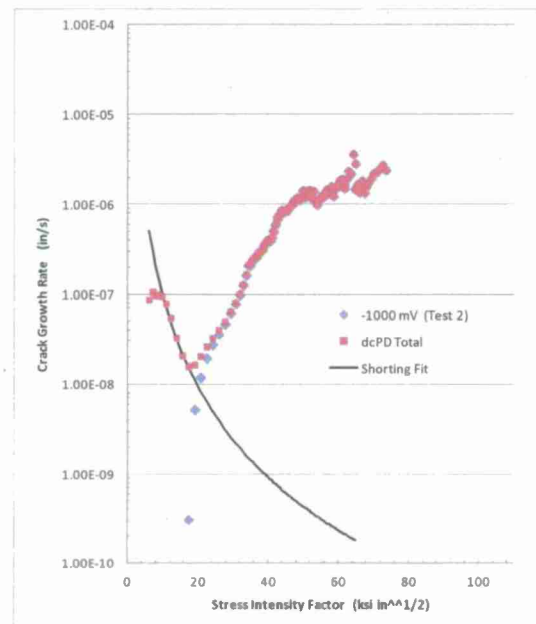
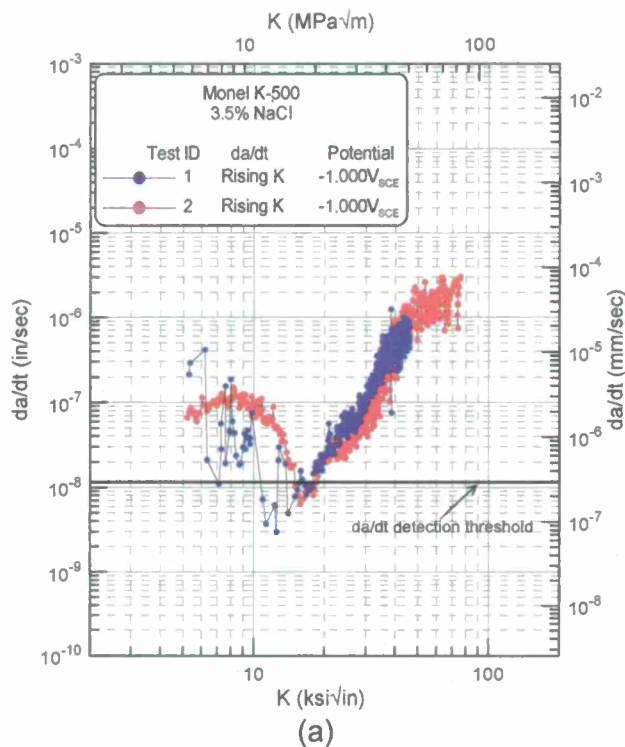
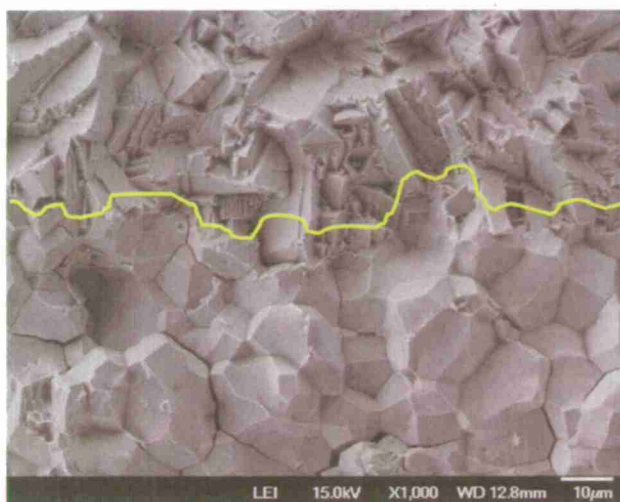


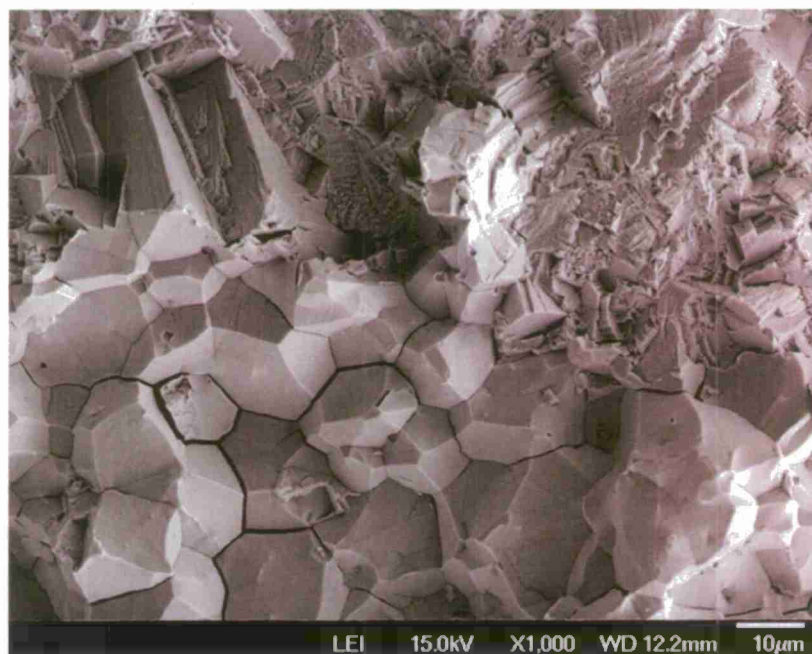
**Figure 6** (a) Replicate experimental characterizations of  $da/dt$  vs  $K$  for Monel K-500 (ST-A, ATI Allvac 2011) stressed under slow-rising  $dK/dt$  of  $0.3 \text{ MPa}\sqrt{\text{m}}/\text{h}$  in NaCl solution at constant-applied potential of  $-1,000 \text{ mV}_{\text{SCE}}$ . (b)  $da/dt$  computed with increased crack length interval, with and without correction for crack surface electrical contact.



(a)

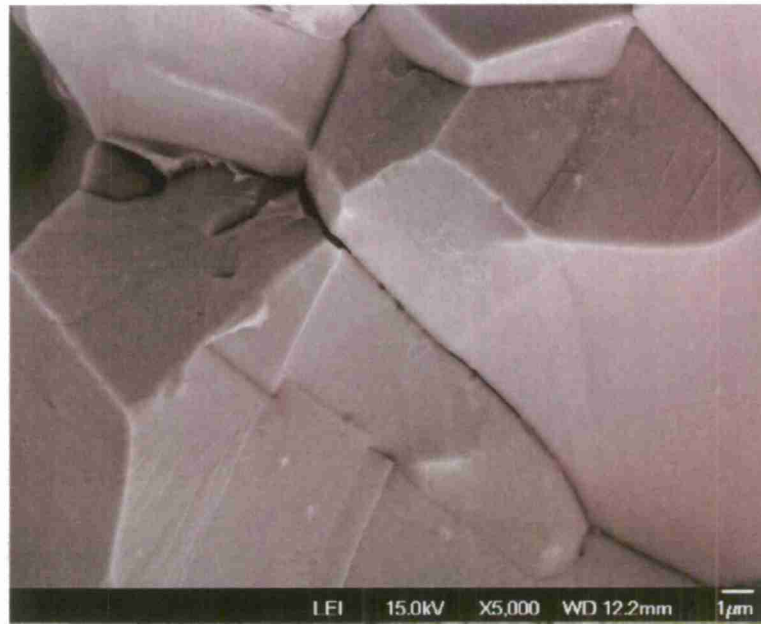


(b)

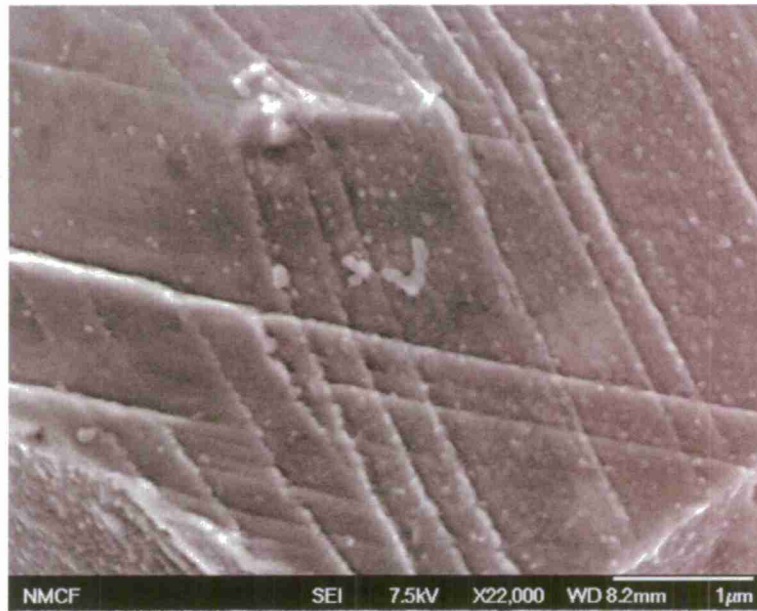


(c)





(d)



(e)

**Figure 7** (a), (c), (d), (e): Scanning electron fractographs for Monel K-500 (ST-A; ATI Allvac 2011), stressed under slow-rising initial  $dK/dt$  of  $0.3 \text{ MPa}\sqrt{\text{m/h}}$  in NaCl solution at constant-applied potential of  $-1,000 \text{ mV}_{\text{SCE}}$ , showing intergranular HEAC transitioning from the mixed transgranular-intergranular fatigue crack front in (a) and (c). Crack growth is from top to bottom in each image. (b): Scanning electron micrograph of anodically etched Monel K-500 (ST-A). (d) and (e): Slip traces are evident on grain facets and the small particles are largely Ti-rich carbides, with occasional inclusions.

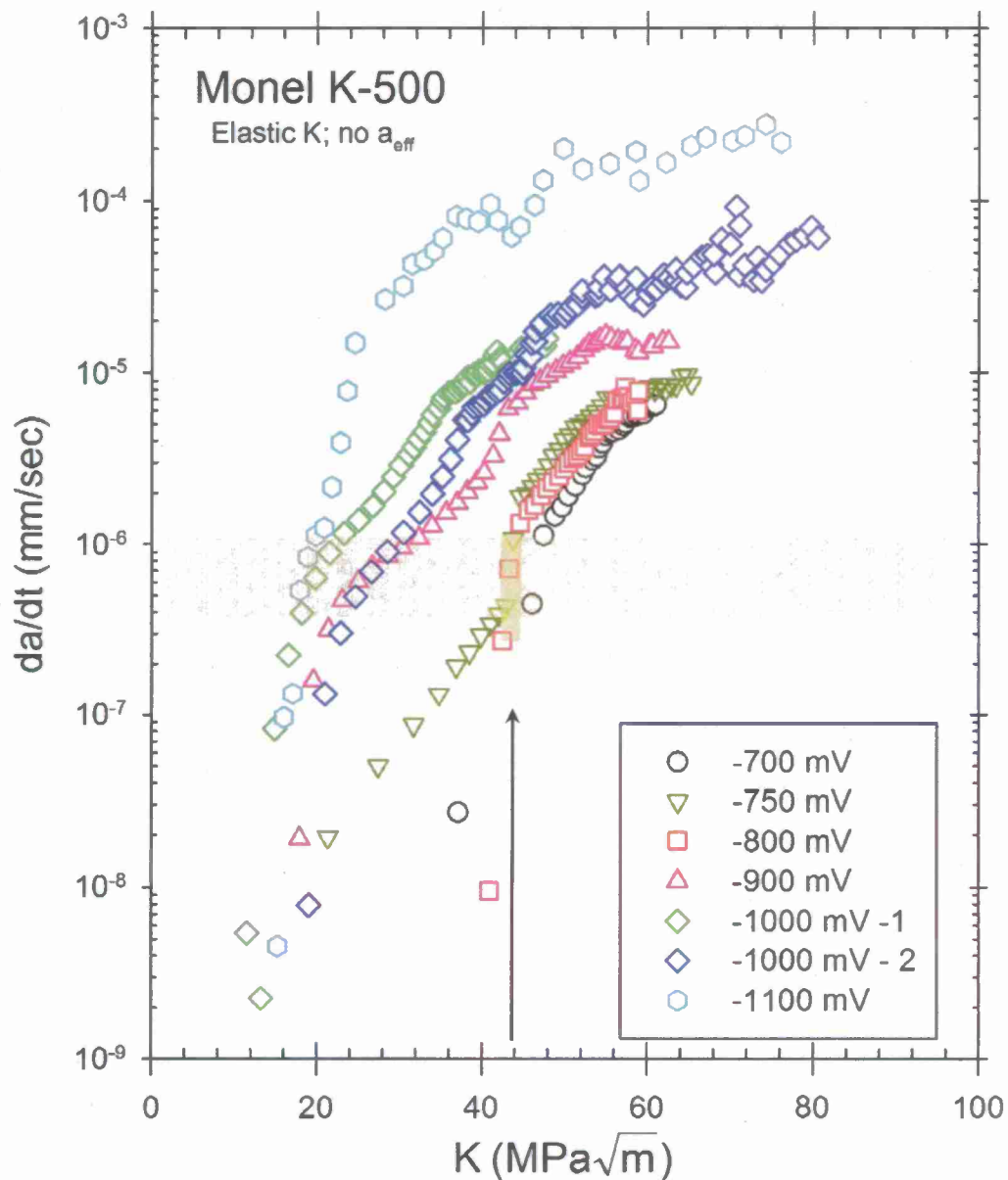


**Figure 8**  $Da/dt$  versus  $K$  for Monel K-500 (ST-A, ATI Allvac 2011) stressed under slow-rising  $dK/dt$  of 0.3 MPa $\sqrt{m}/h$  in NaCl solution at various constant-applied potentials of between -700 and -1,100 mV<sub>SCE</sub>. The vertical line at  $K = 43.9$  MPa $\sqrt{m}$  represents the point in the loading protocol where constant  $dK/dt$  was increased from 0.3 to 1.1 MPa $\sqrt{m}/h$  to reduce test duration. The shaded band shows the range of false  $da/dt$  which is produced by the effect of crack tip plastic deformation on  $dcPD$  for  $dK/dt$  of 0.3 MPa $\sqrt{m}/h$  (lower level of rectangle) and 1.0 MPa $\sqrt{m}/h$  (upper level of rectangle).



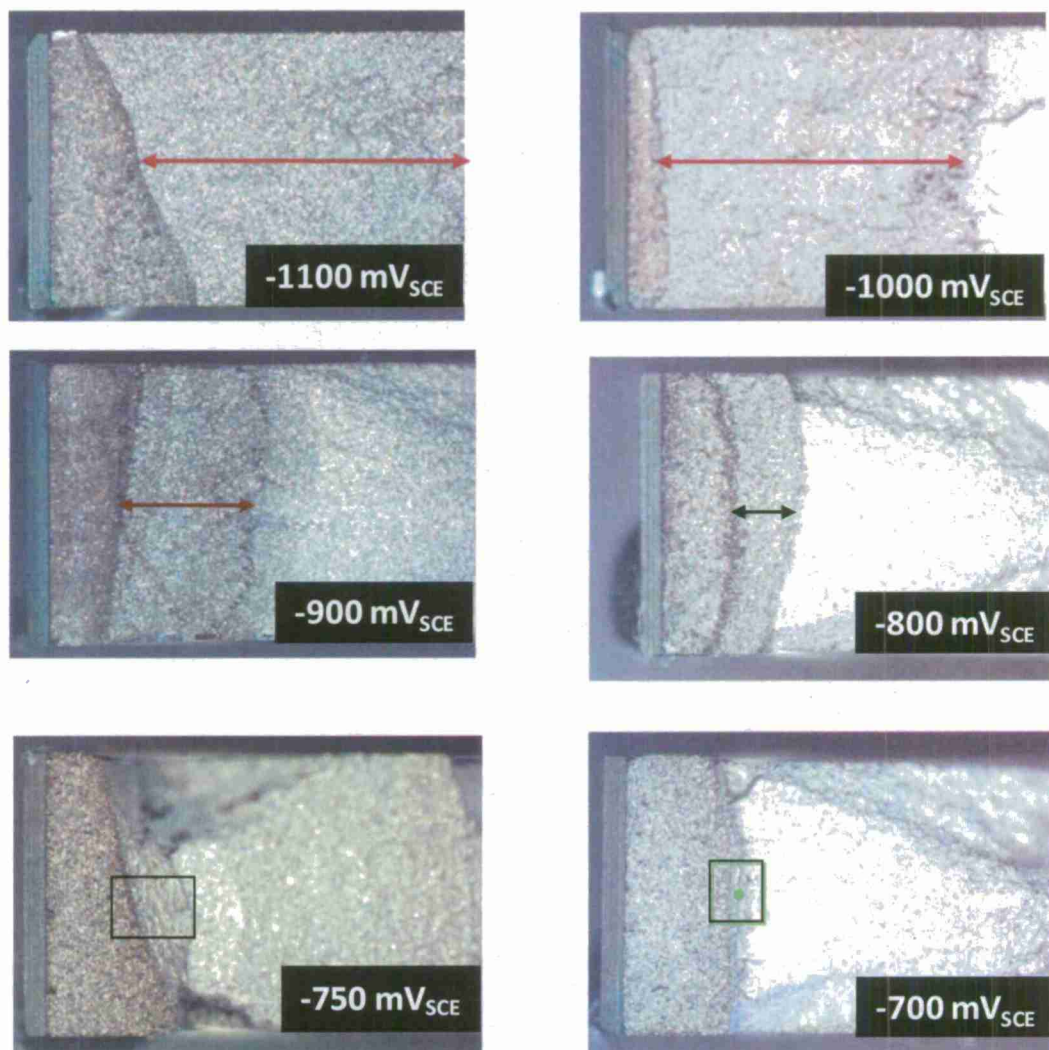
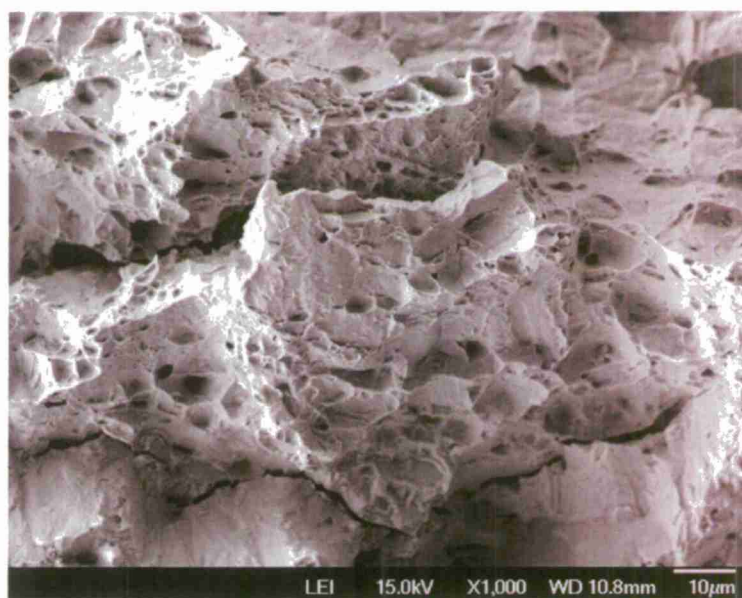


**Figure 9** Low magnification scanning electron fractographs showing the morphology of cracking in Monel K-500 (ST-A, ATI Allvac 2011) stressed under slow-rising initial  $dK/dt$  of  $0.3 \text{ MPa}\sqrt{\text{m/h}}$  in NaCl solution at various constant-applied potentials of between -700 and -1,100  $\text{mV}_{\text{SCE}}$ . Crack growth is from left to right in each image, with the machined notch, then fatigue precrack, SCC (horizontal arrow), fatigue-to-fracture regions shown. Specimen thickness is nominally 2.54 mm to calibrate image magnifications.



(a)



(b)

**Figure 10** Scanning electron fractographs for Monel K-500 (ST-A, ATI Allvac 2011), stressed under slow-rising initial  $dK/dt$  of  $0.3 \text{ MPa}\sqrt{\text{m/h}}$  in NaCl solution at constant-applied potential of  $-700 \text{ mV}_{\text{SCE}}$ , showing a lack of resolvable intergranular HEAC transitioning from the transgranular fatigue crack front in (a). The stretch zone of plastic deformation along the fatigue crack front is shown in (b). Crack growth is from top to bottom in each image.



(a)

(b)

**Figure 11** Scanning electron fractographs for Monel K-500 (ST-A, ATI Allvac 2011), stressed under slow-rising initial  $dK/dt$  of  $0.3 \text{ MPa}\sqrt{\text{m/h}}$  in NaCl solution at constant-applied potential of  $-750 \text{ mV}_{\text{SCE}}$ , showing a lack of resolvable intergranular HEAC transitioning, but rather microvoid-based cracking, transitioning from the transgranular fatigue crack front. Crack growth is from left to right in each image, with the fatigue precrack front located about 1/3 of the distance from the left edge of each image.



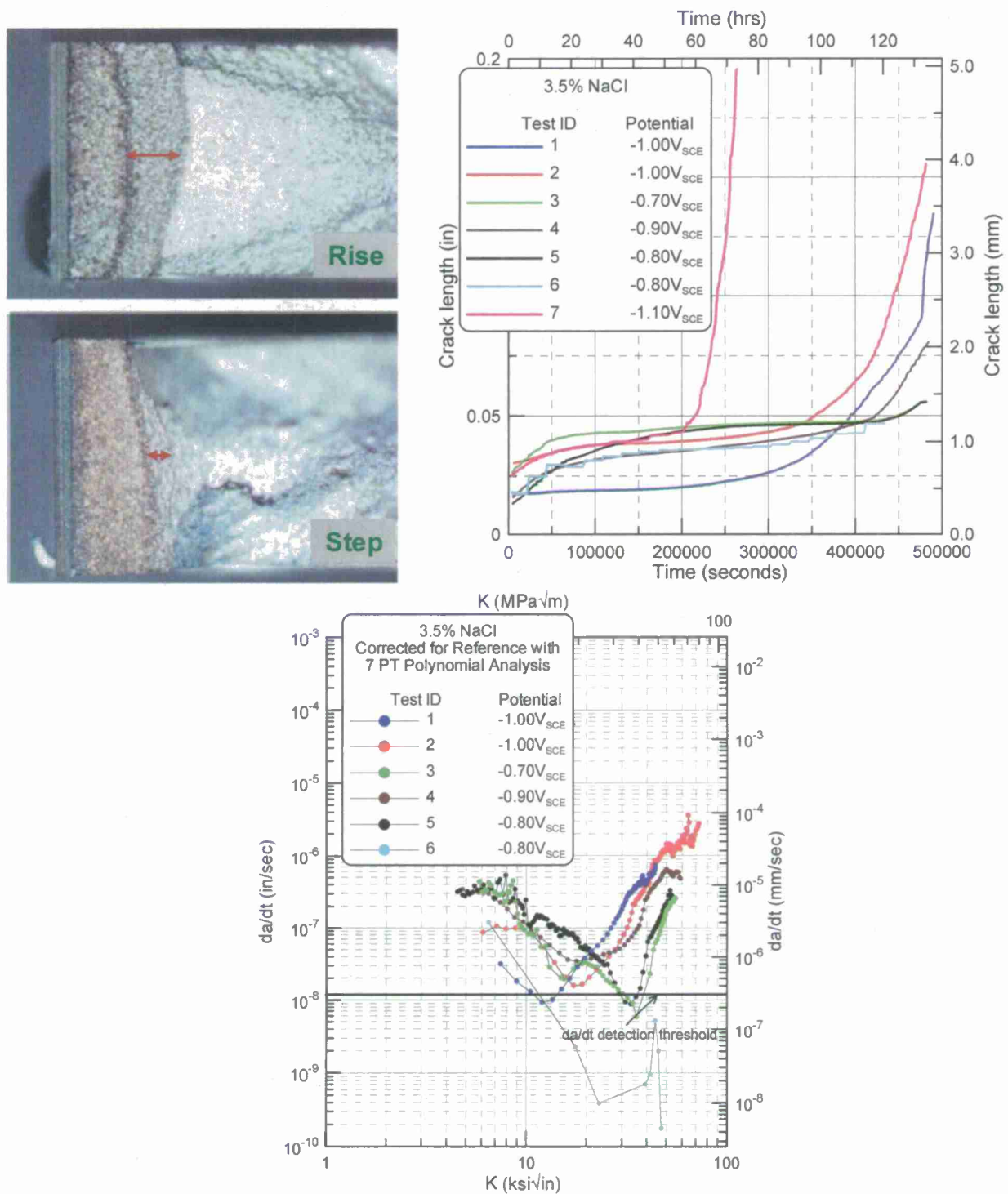
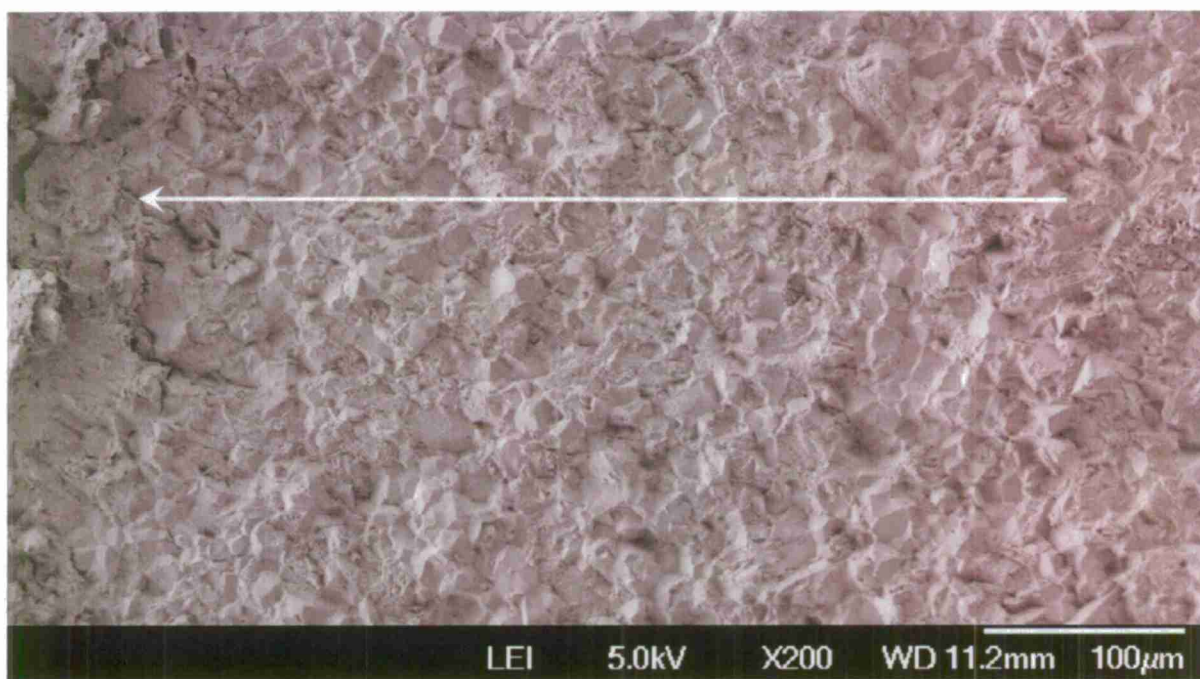
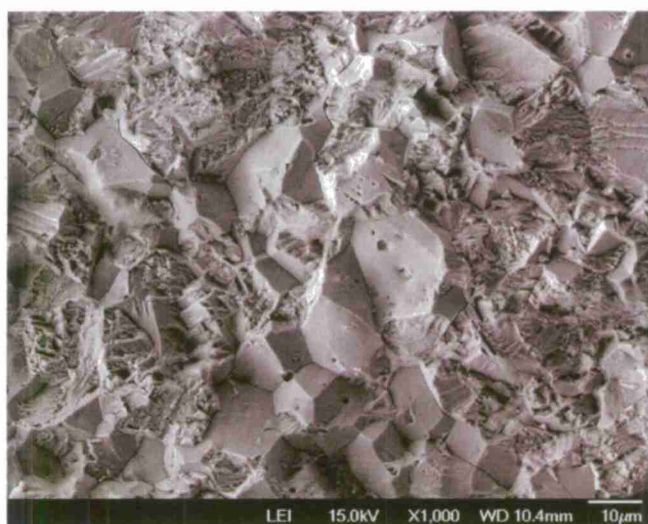


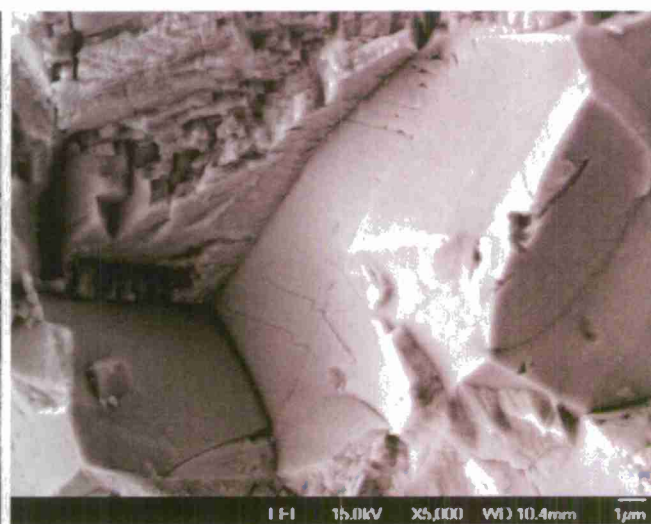
**Figure 12** Effect of continuous-rising K ( $dK/dt = 0.3 \text{ MPa}\sqrt{m}/h$ ) versus step-hold K (7  $\text{MPa}\sqrt{m}/h$  rise and 6 h hold) on: (a) optically imaged extent of HEAC, (b) crack length versus time where "5" is the continuous loading case and "6" is the step-hold loading, and (c)  $da/dt$  versus K where  $da/dt$  was computed based on crack dcPD crack growth during the hold period for the step test and with shorting correction during the rising K experiment. Monel K-500 (ST-A, ATI Allvac 2011) was stressed in NaCl solution at constant-applied potential of  $-800 \text{ mV}_{\text{SCE}}$ .



(a)

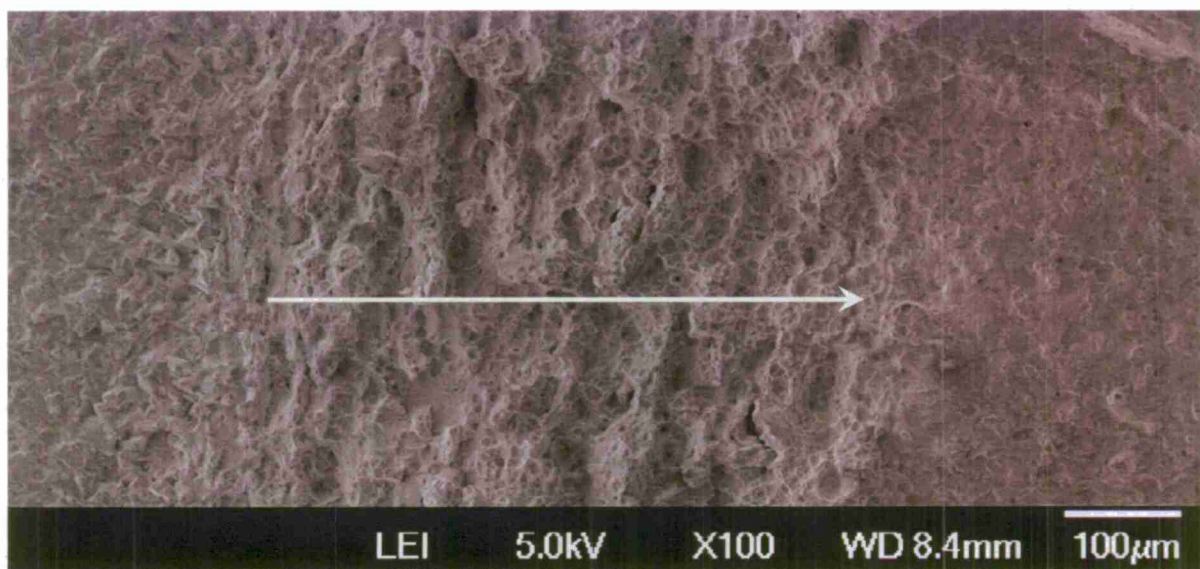


(b)



(c)

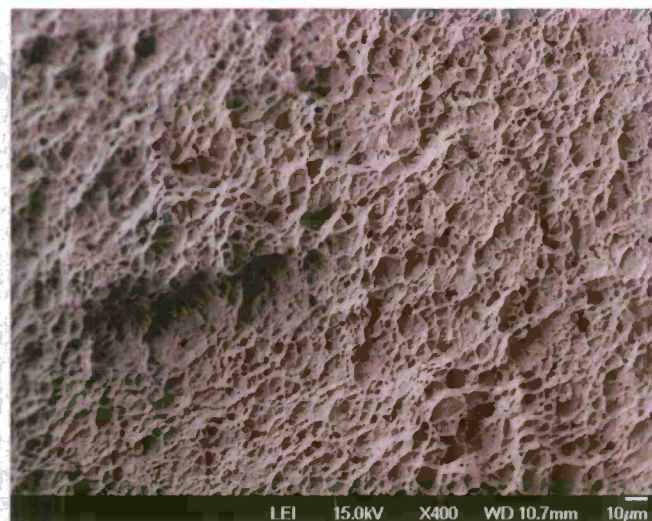




(d)



(e)



(f)

**Figure 13** Fracture surface morphology for Monel K-500 (ST-A, ATI Allvac, 2011) stressed in NaCl solution at constant-applied potential of  $-800 \text{ mV}_{\text{SCE}}$  for: (a), (b) and (c) continuous-rising K ( $dK/dt = 0.3 \text{ MPa}\sqrt{\text{m/h}}$ ), with crack growth from right to left in (a); and IG HEAC indicated by the horizontal arrow, and (d), (e) and (f) step-hold K ( $7 \text{ MPa}\sqrt{\text{m/h}}$  rise and 6 h hold), with crack growth from left to right.



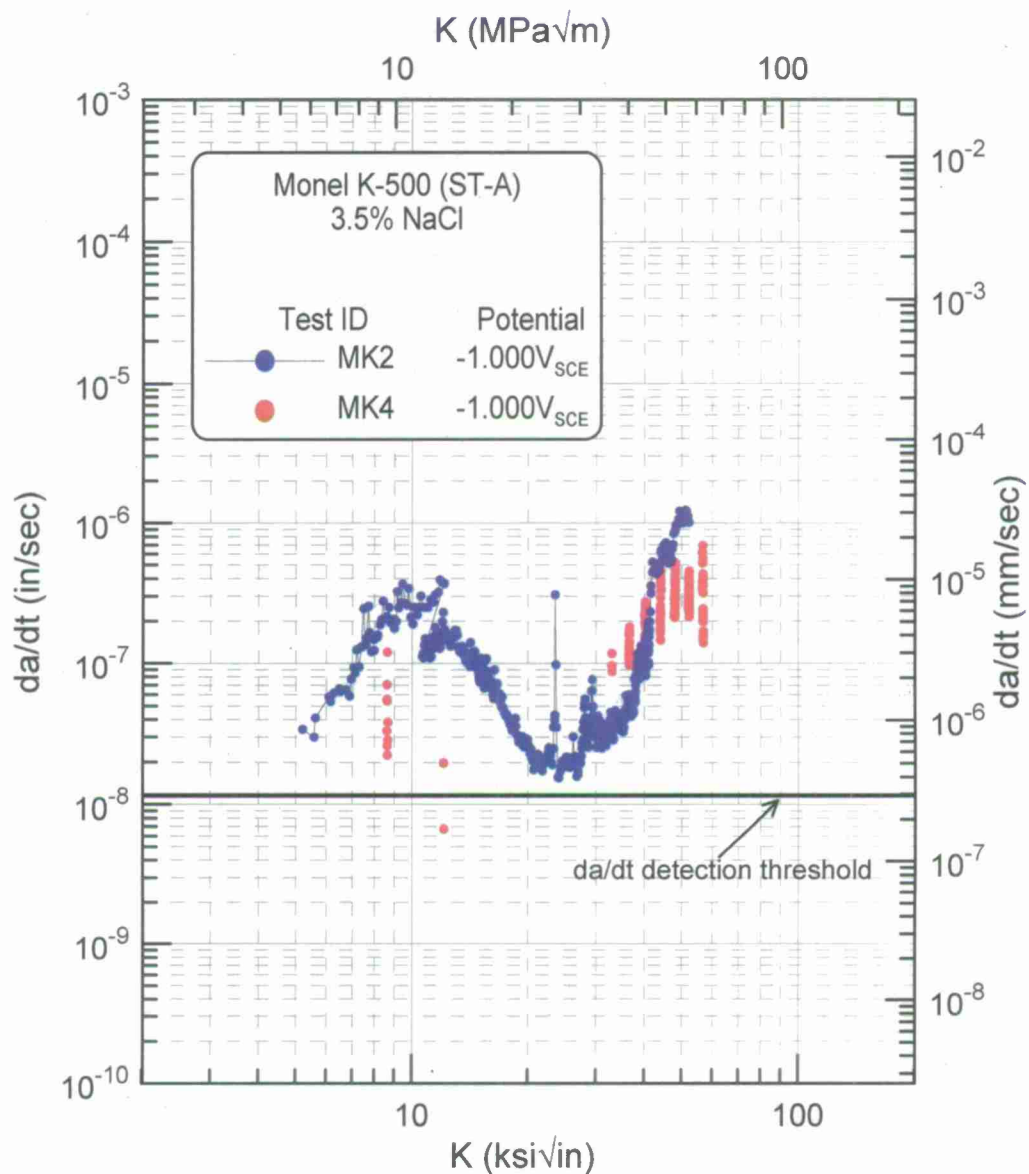


**Figure 14** Effect of continuous-rising  $K$  ( $dK/dt = 0.3 MPa\sqrt{m/h}$ ) versus step-hold  $K$  ( $7 MPa\sqrt{m/h}$  rise and 6 h hold) on  $da/dt$  versus  $K$ , where  $da/dt$  was computed based on dcPD crack growth during the hold period for the step test and crack length computed with shorting correction during the rising  $K$  experiment. Monel K-500 (ST-A; Special Metals, 2008) was stressed in NaCl solution at constant-applied potential of  $-934 mV_{SCE}$ .

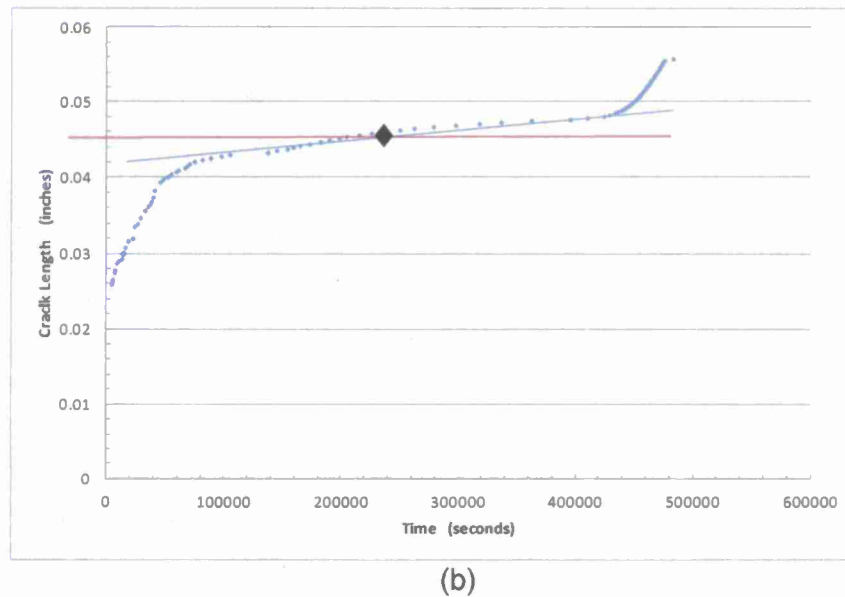
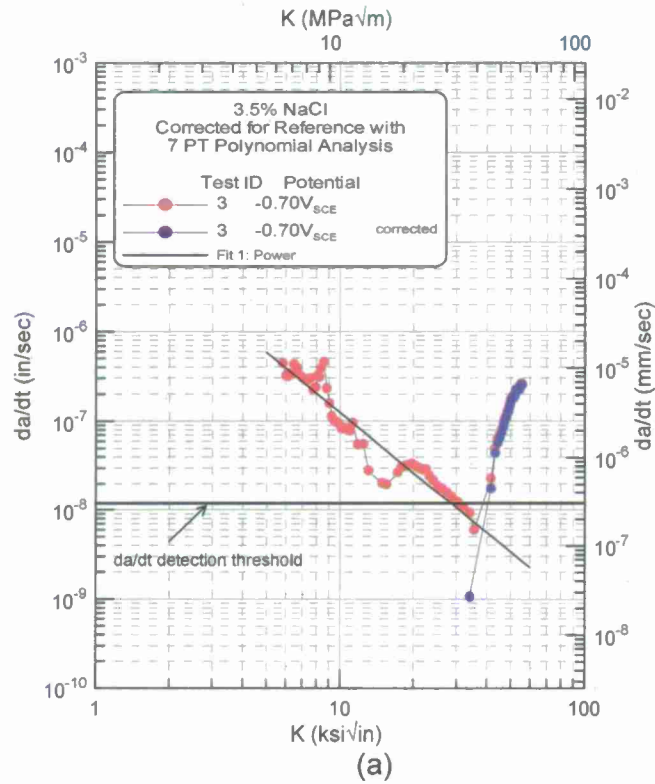


**Figure 15** Apparent crack growth rate versus  $K$  for Monel K-500 (ST-A, ATI Allvac 2011), stressed under slow-rising initial  $dK/dt$  of  $0.3 \text{ MPa}\sqrt{\text{m}}/\text{h}$  in NaCl solution at constant-applied potential of  $-700 \text{ mV}_{\text{SCE}}$ : (a) crack growth rate versus applied elastic  $K$  and (b) crack length from dcPD versus time during slow-rising load.

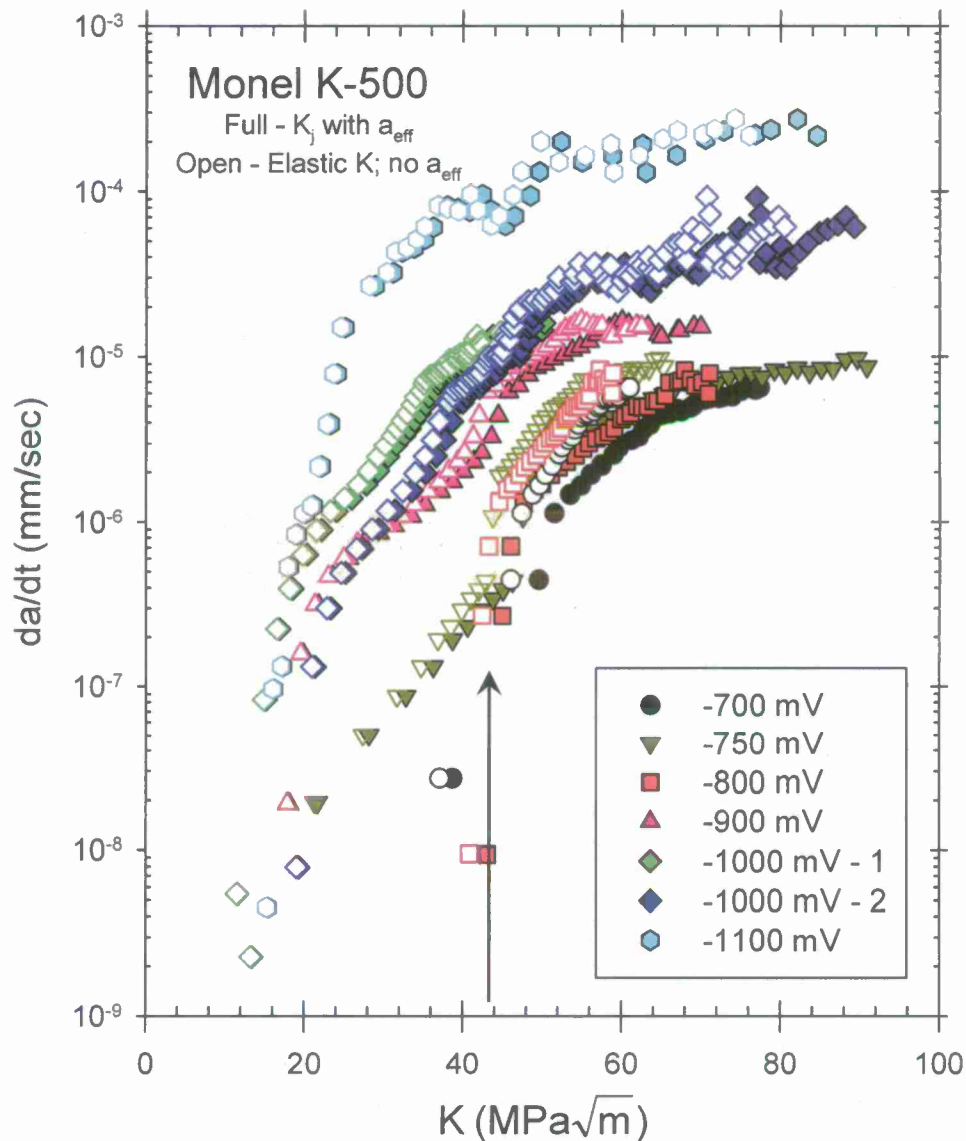


**Figure 16**  $Da/dt$  versus  $K$  for Monel K-500 (ST-A, ATI Allvac 2011) stressed under slow-rising initial  $dK/dt$  of 0.3 MPa $\sqrt{m}/h$  in NaCl solution at various constant-applied potentials of between -700 and -1,100 mV<sub>SCE</sub>.  $Da/dt$  is plotted versus elastic  $K$  (open) from Figure 8 and elastic-plastic  $K_j$ . The shaded band shows the range of false  $da/dt$  which is produced by the effect of crack tip plastic deformation on dcPD for  $dK/dt$  of 0.3 MPa $\sqrt{m}/h$  (lower level of rectangle) and 1.0 MPa $\sqrt{m}/h$  (upper level of rectangle), which is not eliminated by the global reference probe normalization. The constant  $dK/dt$  was 0.3 MPa $\sqrt{m}/h$  for  $K < 43.9$  MPa $\sqrt{m}$  and was increased by 3.3 times at this  $K$  level to a constant value of 1.0 MPa $\sqrt{m}/h$  in order to conserve test time. For lower levels of crack growth rate, this loading rate increase produced a proportionate rise in  $da/dt$ .

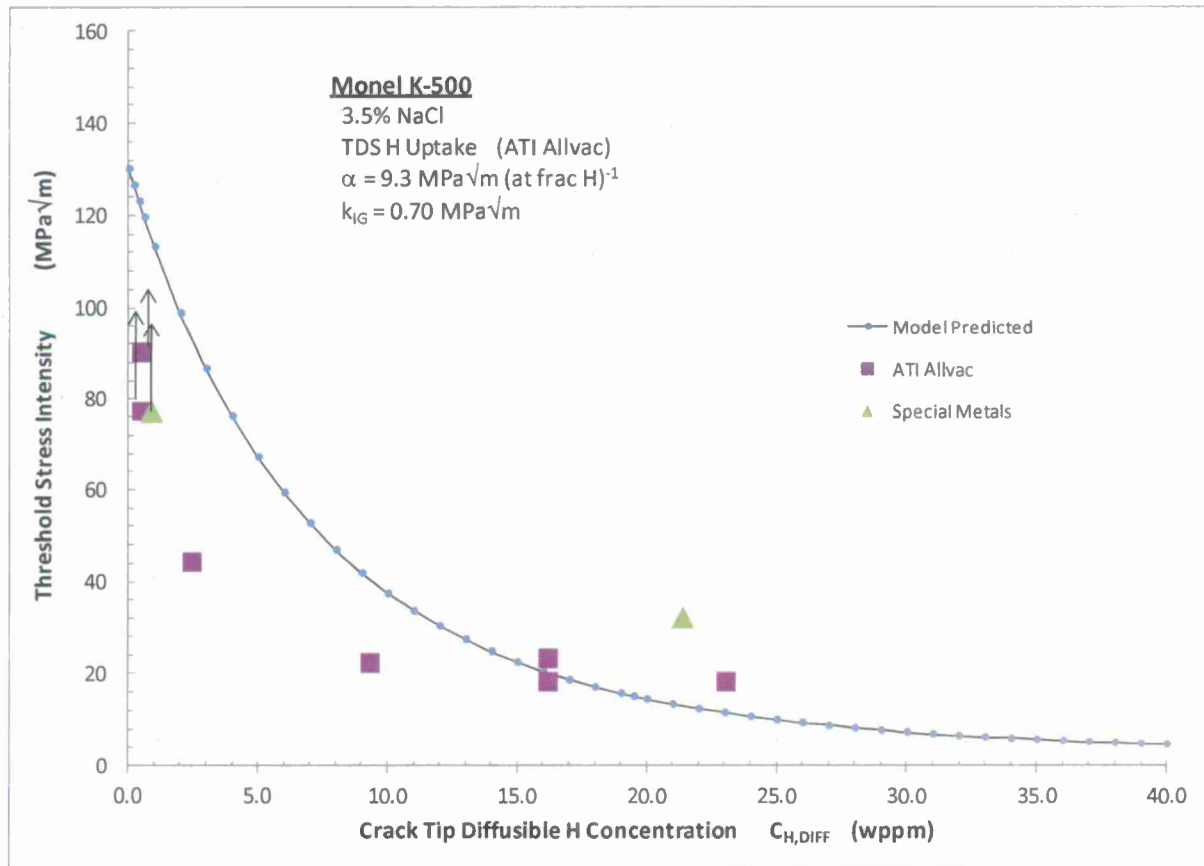


**Figure 17** Model predicted (Equations 1 and 3) and measured values (Table 3) of  $K_{TH}$  for HEAC plotted versus crack tip diffusible H concentration determined for Monel K-500 (ST-A, ATI Allvac, 2011) stressed in 3.5% NaCl at various-applied cathodic potentials between -1100 and -700 mV<sub>SCE</sub>. The relationship between  $C_{H-Diff}$  and applied potential is given in Figure 5 and Equation 9 for this heat of Monel K-500. Measured values for  $K_{TH}$  are included for the Special Metals lot of Monel K-500 (Footnote 1), using an estimate of the correct H uptake law which was reported for this heat [17].

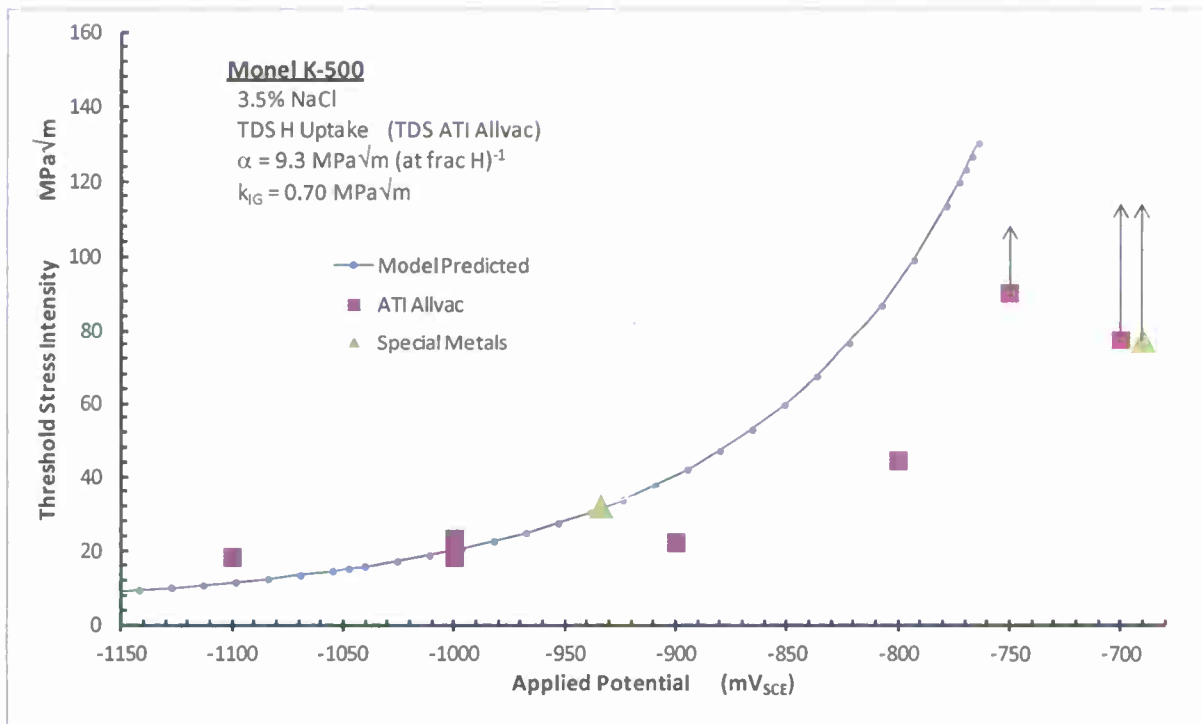


**Figure 18** Model predicted (Equations 1 and 3) and measured values (Table 3) of  $K_{TH}$  for HEAC plotted versus applied cathodic potential for Monel K-500 (ST-A, ATI Allvac, 2011) stressed in 3.5% NaCl. The relationship between  $C_{H-Diff}$  and applied potential is given in Figure 5 and Equation 9 for this heat of Monel K-500. Measured values for  $K_{TH}$  are included for the Special Metals lot of Monel K-500 (Footnote 1). The good agreement with the model prediction may be fortuitous since, the H uptake law reported for this heat [17] was higher by about 1.8 times compared to that for the ATI Allvac lot (Fig. 4) used to establish the model prediction in this plot.

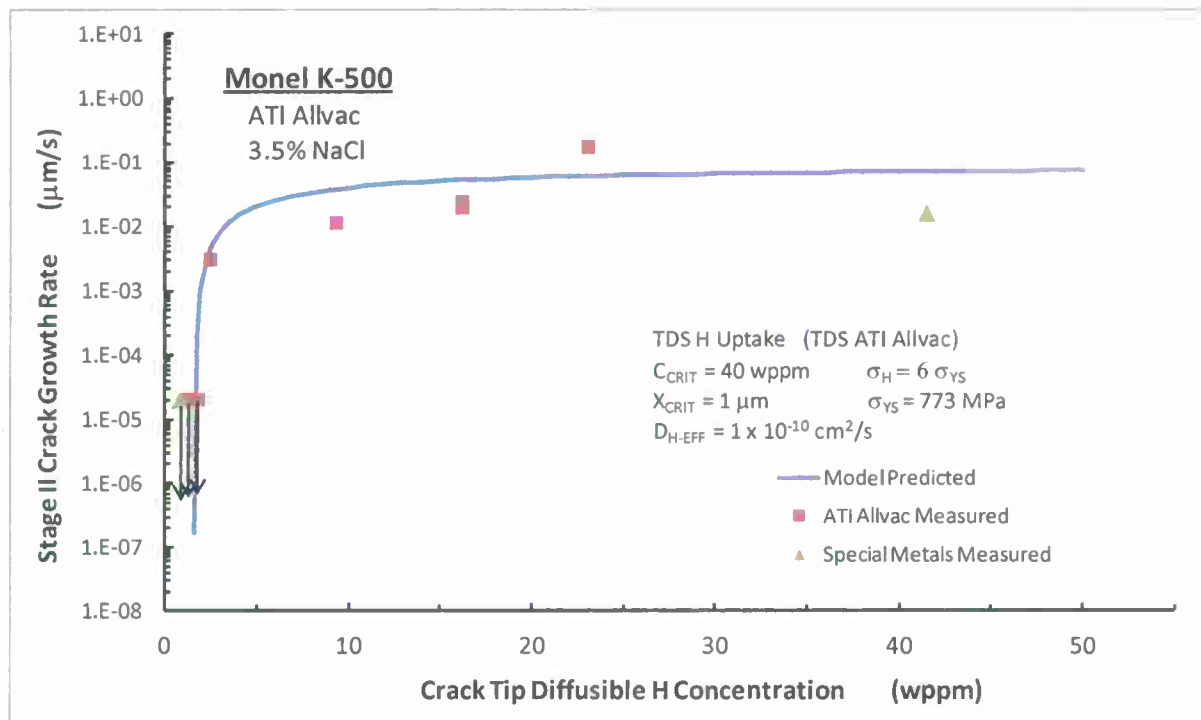


**Figure 19** Model predicted (Equation 2 and 3) and measured values (Table 3) of Stage II crack growth rate for HEAC plotted versus crack tip diffusible H concentration determined for Monel K-500 (ST-A, ATI Allvac, 2011) stressed in 3.5% NaCl at various-applied cathodic potentials between -1100 and -700 mV<sub>SCE</sub>. The relationship between  $C_{H\text{-Diff}}$  and applied potential is given in Figure 5 and Equation 9 for this heat of Monel K-500. Measured values for Stage II  $da/dt$  are included for the Special Metals lot of Monel K-500 (Footnote 1), using the correct H uptake law which was reported for this heat [17].



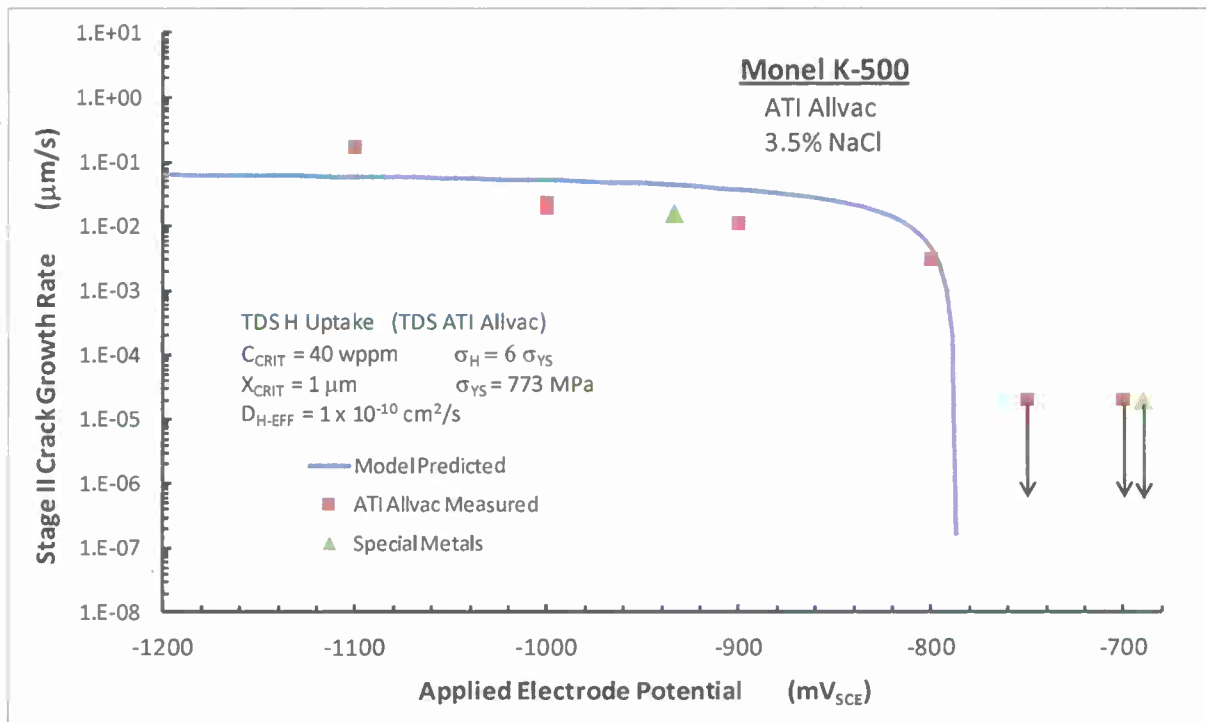


**Figure 20** Model predicted (Equations 2 and 3) and measured values (Table 3) of the Stage II crack growth rate for HEAC plotted versus applied cathodic potential for Monel K-500 (ST-A, ATI Allvac, 2011) stressed in 3.5% NaCl. The relationship between  $C_{H-Diff}$  and applied potential is given in Figure 5 and Equation 9 for this heat of Monel K-500. Measured values for Stage II  $da/dt$  (Table 3) are included for the Special Metals lot of Monel K-500 (Footnote 1). The good agreement with the model prediction may be fortuitous since, the H uptake law reported for this heat [17] was higher by about 1.8 times compared to that for the ATI Allvac lot (Fig. 4) used to establish the model prediction in this plot.

SCCrack

Alloy Input | Plot Plots | da/dN Plots | K-R Plots

Material: Monel K500

Max a [mm]: 9.9411

Polarization (mV-SCE): Normal Distribution Mean: -0.825 COV: 0.05  
 (-700 to -550) 95% bounds: -907.50 -742.50

☐ Randomize Material  
☒ Randomize Polarization  
☒ Randomize Crack Size

Num of Simulations: 100

K solution: Thread Root Circumferential Crack With Nut

☒ Stress [% YS]: 30  
☐ Axial force [N]: 15000  
☐ Torque [N mm]: 30000

Initial a [mm]: Normal Distribution Mean: 0.350 COV: 0.05

Aspect Ratio: Constant

Residual Stress: None

Outer diameter [mm]: 12.5235 Standard Thread: 1/2-13  
 Inner diameter [mm]: 9.9411  
 Root radius [mm]: 0.1524

Options Cancel Run...

Figure 21 Graphical User Interface for SCCrack.

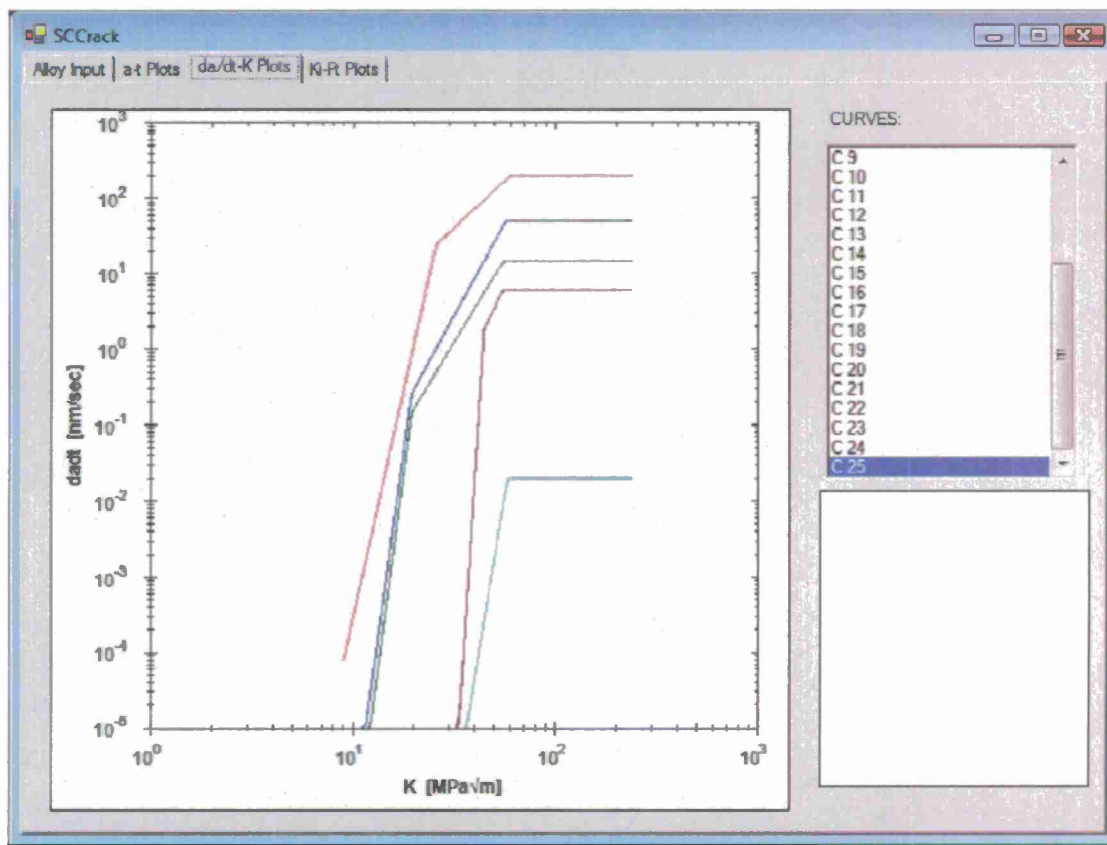


**Figure 22** Input estimates of  $da/dt$  versus applied-elastic  $K$  relationships for Monel K-500 (ST-A, ATI Allvac lot) stressed in NaCl at various potentials, based on the data presented in Fig. 8.

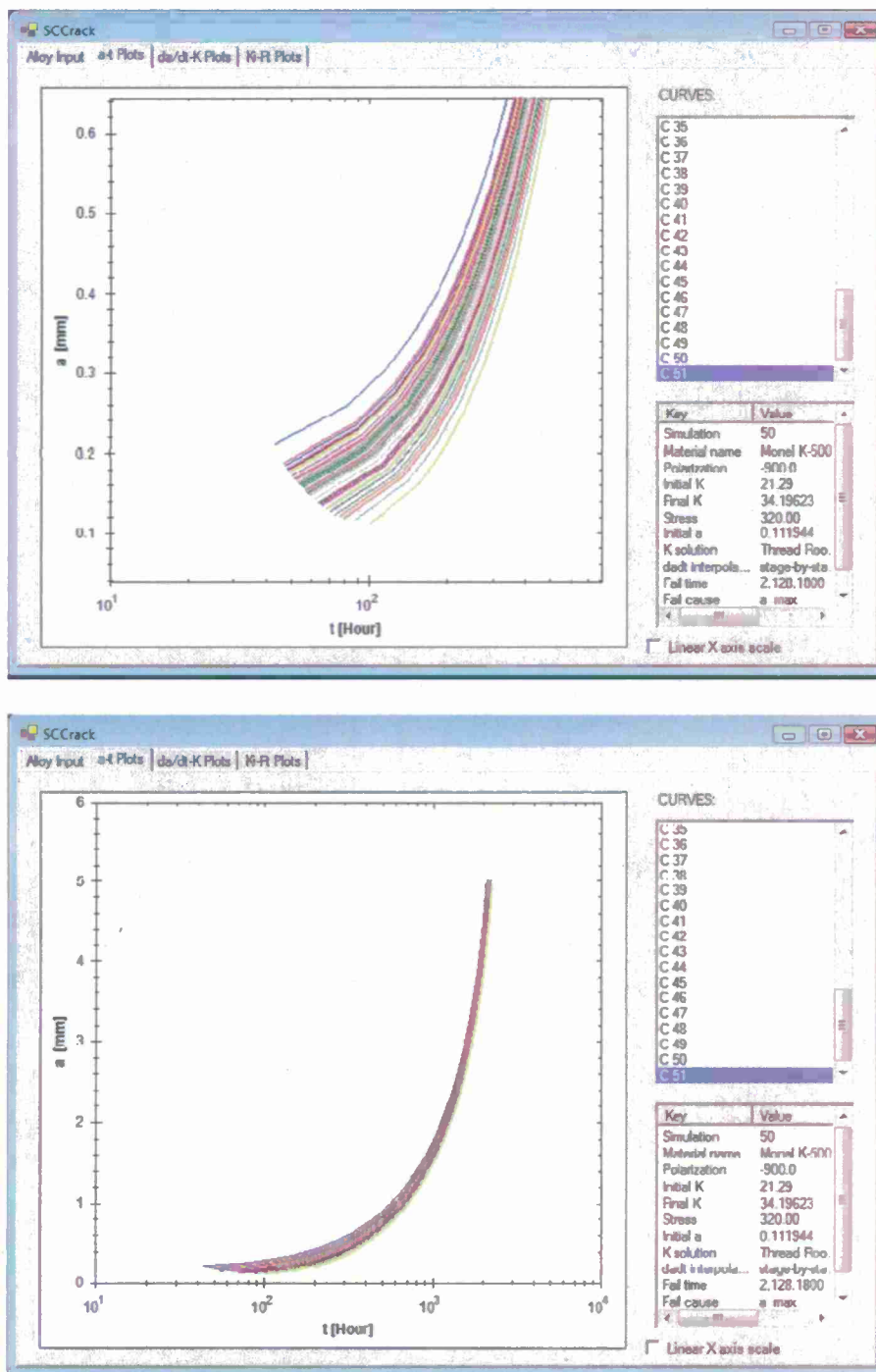


**Figure 23** SCCrack simulation of the IGSCC life of a cracked thread root of Monel K-500 (ST-A) stressed quasi-statically in NaCl solution, showing the effect of Monte Carlo selected variation in starting elliptically-shaped crack depth about a mean level of  $150\ \mu\text{m}$  with a coefficient of variation of 0.20. Applied-tensile stress is constant at 40% of tensile yield strength and the level of cathodic polarization is fixed at  $-900\ \text{mV}_{\text{SCE}}$ .

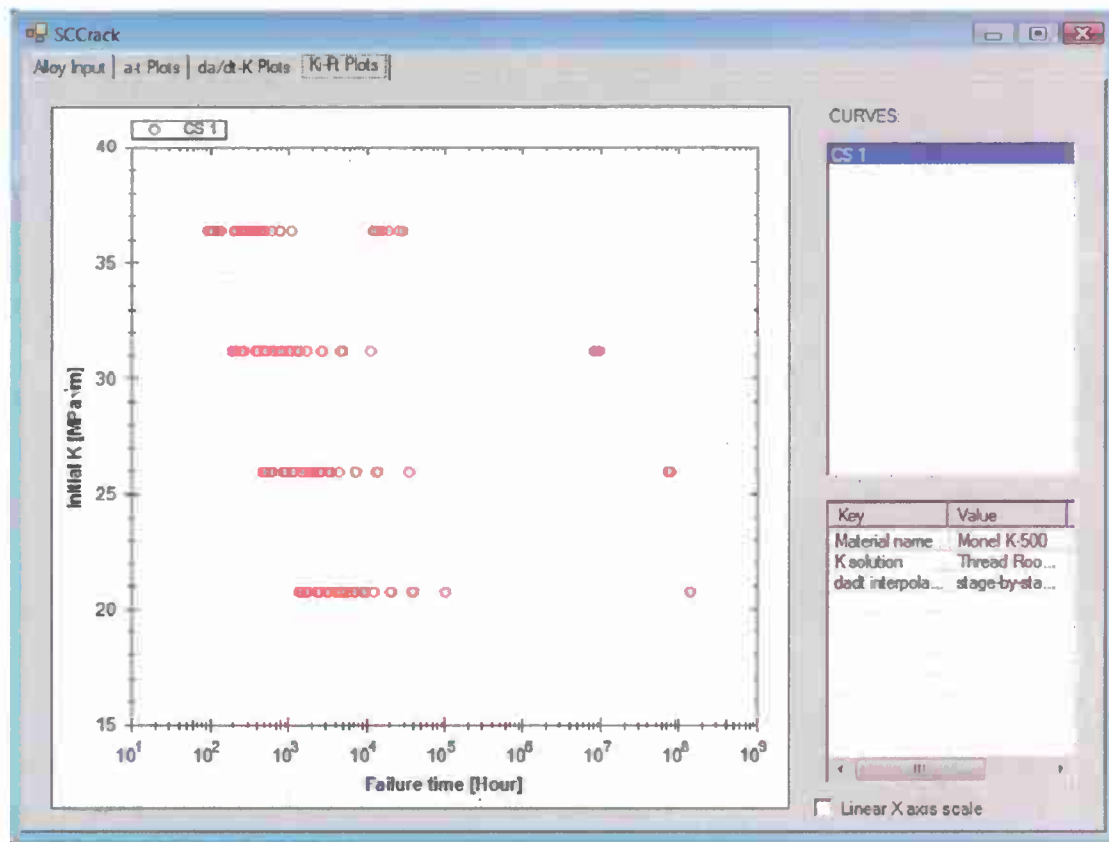


**Figure 24** SCCrack simulation of the IGSCC life of a cracked thread root of Monel K-500 (ST-A) stressed quasi-statically in NaCl solution showing the effect of Monte Carlo selected variation in applied potential about a mean level of -850 mV<sub>SCE</sub> with a coefficient of variation of 0.06 for a normal distribution (-952 mV<sub>SCE</sub> < E < -748 mV<sub>SCE</sub> at +/- 95% confidence level). Applied stress is constant at either 40%, 50%, 60% or 70% of tensile yield strength. The thread-root semi-elliptical crack is initially 100 μm deep.

**REPORT DOCUMENTATION PAGE**Form Approved  
OMB No. 0704-0188

Public reporting burden for this collection of information is estimated to average 1 hour per response, including the time for reviewing instructions, searching existing data sources, gathering and maintaining the data needed, and completing and reviewing this collection of information. Send comments regarding this burden estimate or any other aspect of this collection of information, including suggestions for reducing this burden to Department of Defense, Washington Headquarters Services, Directorate for Information Operations and Reports (0704-0188), 1215 Jefferson Davis Highway, Suite 1204, Arlington, VA 22202-4302. Respondents should be aware that notwithstanding any other provision of law, no person shall be subject to any penalty for failing to comply with a collection of information if it does not display a currently valid OMB control number. PLEASE DO NOT RETURN YOUR FORM TO THE ABOVE ADDRESS.

<b>1. REPORT DATE (DD-MM-YYYY)</b> 11/09/2012		<b>2. REPORT TYPE</b> Final		<b>3. DATES COVERED (From - To)</b> 02/15/10 – 08/14/12	
Mechanism-Based Modeling of Hydrogen Environment Assisted  Cracking (HEAC) in High Strength Alloys for Marine Applications:  Prediction of Monel K-500 HEAC for Select Environmental & Mechanical Conditions				<b>5a. CONTRACT NUMBER</b> N/A	
				<b>5b. GRANT NUMBER</b> N00014-10-1-0552	
				<b>5c. PROGRAM ELEMENT NUMBER</b> N/A	
<b>6. AUTHOR(S)</b> Dr. J. R. Scully & Dr. R. P. Gangloff				<b>5d. PROJECT NUMBER</b> N/A	
				<b>5e. TASK NUMBER</b> N/A	
				<b>5f. WORK UNIT NUMBER</b> N/A	
<b>7. PERFORMING ORGANIZATION NAME(S) AND ADDRESS(ES)</b>  University of Virginia Office of Sponsored Programs P. O. Box 400195 Charlottesville, Virginia 22904-4195				<b>8. PERFORMING ORGANIZATION REPORT NUMBER</b>  135228-101-GG11294-31340	
<b>9. SPONSORING / MONITORING AGENCY NAME(S) AND ADDRESS(ES)</b> Office of Naval Research 875 North Randolph Street Arlington, Virginia 22203-1995				<b>10. SPONSOR/MONITOR'S ACRONYM(S)</b> N/A	
				<b>11. SPONSOR/MONITOR'S REPORT NUMBER(S)</b> N/A	
<b>12. DISTRIBUTION / AVAILABILITY STATEMENT</b>  Approved for public release, distribution unlimited.					
<b>13. SUPPLEMENTARY NOTES</b> N/A					
<b>14</b> The crack propagation perspective provides a framework to quantify subcritical cracking phenomena for component life assessment in a marine application. Over the past 25 years, extensive data have been generated to describe cracking in a range of high strength alloys of naval significance. A variety of mechanism-based models have been reported in the literature, derived from this experimentation, but all involve multiple-adjustable parameters associated with uncertainties in the crack tip hydrogen interactions that govern crack initiation and propagation. As such, modeling and simulation have not been used extensively here-to-fore for alloy and protection system development; rather, time consuming experimentation continues to be carried out and results are often explained with questionable-limited speculations. However, improvements to H cracking models are achievable by developing new understanding of crack tip electrochemistry and mechanics, as guided by the existing interdisciplinary experience base. The Monel K-500 alloys system provides an ideal case, of both practical and scientific relevance, to extend understanding of HEAC modeling. By coupling with external definition of the mechanics condition, the lifetime of the component can be estimated as long as the state of stress, material, geometry, electrochemical conditions, and temperature are defined.					
<b>15. SUBJECT TERMS</b> crack propagation, crack propagation, multiple-adjustable parameters associated with uncertainties					
<b>16. SECURITY CLASSIFICATION OF:</b>			<b>17. LIMITATION OF ABSTRACT</b>	<b>18. NUMBER OF PAGES</b>	<b>19a. NAME OF RESPONSIBLE PERSON</b>
<b>a. REPORT</b> Unclassified	<b>b. ABSTRACT</b> Unclassified	<b>c. THIS PAGE</b> Unclassified	UL	119	J. R. Scully
					<b>19b. TELEPHONE NUMBER (include area code)</b> 434-982-5786